Numerical Radiative Transfer and the Hydrogen Reionization of the Universe

Margarita Borisova Petkova

München 2011

Numerical Radiative Transfer and the Hydrogen Reionization of the Universe

Margarita Borisova Petkova

Dissertation
an der Fakultät für Physik
der Ludwig–Maximilians–Universität
München

vorgelegt von
Margarita Borisova Petkova
aus Sofia, Bulgarien

München, den 24. Januar, 2011

...и помни човече,
когато си на брега, движи се лодката,
когато си в лодката, променят се бреговете...
Павел Вежинов

Contents

Zusammenfassung

Eine der interessantesten Fragen der modernen Kosmologie ist, wie sich das Universum aus einem einfachen, nahezu gleichförmigen Zustand kurz nach dem Urknall in das komplexen Gebilde entwickeln konnte, dass wir heute beobachten. Insbesondere möchte man verstehen, wie sich Galaxien bilden und warum sie die Eigenschaften haben, die wir heute im nahen Universum beobachten. Computersimulationen spielen dabei eine wichtigen Rolle, erlauben sie es doch, durch die Gleichungen der Hydrodynamik und Gravitation, den Prozess der Strukturbildung im hoch nichtlinearen Bereich zu modellieren.

In modernen Simulationscodes wird die Gravitatonswechselwirkung der dunklen Materie und des Gases, sowie die Hydrodynamik des Gases berechnet. Strahlungsprozesse werden in der Regel nicht oder nur als externes, räumlich flaches Hintergrundphotonenfeld mit in die Rechnungen einbezogen. Theoretische Modelle legen jedoch nahe, dass das kosmische Strahlungsfeld in gewissen Phasen der Strukturbildung äusserst inhomogen gewesen ist, und so dessen Wechselwirkung mit dem kosmischen Gas und damit der Einfluss auf den Prozess der Galaxienbildung nicht vernächlässigbar ist. Das diffuse Gas nach der Rekombination bei hoher Rotverschiebung neutral war, heute aber hochgradig ionisiert ist. Der Übergang von Neutralität des Gases zum heutigen Plasma nennt man Reionisation. Die dafür verantwortlich ultraviolet Strahlung durchdringt heute den gesamten Kosmos und könnte erklären, warum kleine Zwerggalaxien unverhältnissmässig geringe Leuchtkraft zeigen. Daraus wird sofort klar, dass genaue, in-sich widerspruchsfreie Simulationen der Struktur- und Galaxienbildung und der Entwicklung des kosmischen Strahlungsfeldes und der inhärenten Strahlungsprozesse einen Code erfordern, der direkten Strahlungstransport und die relevanten Strahlungs-quellen und -senken mit in Betracht zieht.

In dieser Doktorarbeit zeigen wir eine neue Implementation von Strahlungstransport in den kosmologischen "smoothed particle hydrodynamics" (SPH) Simulationcode GADGET. Der Algorithmus basiert auf einem schnellen, zuverlässigen und die Photonenzahl erhaltenden Integrationsschema. Wir approximieren das Problem des Strahlungstransports durch Momente der Transportgleichungen und verwenden einen variablen Eddingtontensor um das Gleichungssystem zu schliessen. Dabei folgen wir dem Vorschlag eines OTVET-Schemas von Gnedin & Abel. Wir leiten den entsprechenden anisotropen Diffusionsoperator des lokalen Strahlungstransports im Rahmen der SPH Gleichungen her und lösen das resultierende Gleichungssystem mit der Methode der konjugierten Gradienten. Dieser implizite, iterative Algorithmus erlaubt eine effiziente, parallelisierte Lösung der Matrixgleichung. Schlussendlich verwenden wir ein chemisches Netzwerk für die Rekombinations- und Ionisationsprozess des Stickstoffs um Senken des Strahlungsfeldes zu modellieren. Wir zeigen eine Reihe von numerischen Tests unserer Implementation: zum Beispiel einzelne und mehrere Strahlungsquellen in einem statischen, uniformen Dichtefeld, mit und ohne Temperaturentwicklung; Schattenbildung durch eine Überdichteregion; mehrere Strahlungsquellen in einem statischen kosmologischen Dichtefeld. Alle Tests zeigen gute Übereinstimmung mit analytischen Rechnungen, beziehungsweise anderer

Codes, ausgenommen die Schattenbildung. Im Gegensatz zu den meisten vorhandenen Strahlungstransportcodes kann unsere Implementation zur Laufzeit einer vollen kosmologischen Simulation eingesetzt werden, was es erlaubt Galaxienbildungs- und Reionisationsprozesse gleichzeitig und selbst-konsistent zu simulieren.

Wir zeigen erste Resultate einer Rechnung, in der nur Sterne als Quellen der Strahlung dienen und untersuchen, inwieweit ein solche Szenario zu angemessenen Ergebnissen hinsichtlich Reionisation und Temperatur des intergalaktischen Mediums führen. Dabei zeigt sich, das Sternentstehung allein ausreicht, um das Universum bei einer Rotverschiebung von $z \sim 6$ zu reionisieren. Unter der Annahme angemessener Eingangsparameter reproduzieren unsere Modelle sowohl die Wahrscheinlichkeitsverteilung als auch das Leistungsspektrum des "Lyman α-Forest". Dabei hat das Strahlungsfeld grossen Einfluss auf Sternentstehungsrate in unseren Simulationen und verringert den Anteil von Gas und Sternen in Halos niedriger Masse. Unsere Ergebnisse unterstreichen die Wichtigkeit der Strahlungsrückkopplung in der Entstehung von Galaxien.

Weiterhin zeigen wir eine alternative Behandlung der Physik des Strahlungstransports in kosmologischen Simulationen. Unsere numerische Implementation im Gittercode AREPO basiert auf einem explizit photonenerhaltenden Advektionsschema, indem wir den Strahlungsfluss über die Zellgrenzen des (un-)strukturierten Gitters durch eine Rekonstruktion der Intensität in zweiter Ordnung berechnen. Dazu führen wir eine direkte Diskretisierung der Strahlungstransportgleichung in Boltzmann Form durch. In seiner allgemeinsten Form stellt dieses Schema eine Zerlegung des lokalen Strahlungsfeldes in die lineare Summe von Richtungskonussen auf der Einheitsspähre dar. Das Feld entlang jedes dieses Konusfelds wird unabhängig von den anderen transportiert, mit konstanter Intensität innerhalb des Konus. Die Photonen breiten sich mit (optional: reduzierter[1]) Lichtgeschwindigkeit aus, was eine voll zeitabhängigen Lösung der Strahlungstransportgleichung bedeutet, die sowohl einer beliebige Anzahl von Quellen als auch Streuung behandeln kann. Diese Methode führt auch zu Schattenwurf abhängig von der gewählten Winkelauflösung. Falls die Anzahl der simulierten Punktquellen gering ist und Streuung vernachlässigt werden kann, kann dieser Algorithmus sogar jede einzelne Quelle mit exakter Winkelauflösung behandeln, sodass der Fehler im Schattenwurf dem Fehler durch die Gitteraulösung entspricht. Als Kompromiss zwischen den beiden vorherigen Methoden schlagen wir vor nur die lokal hellsten Punktquellen explizit in die Rechnung einzubeziehen und den restlichen Teil der Strahlungsintensität in der Diffusionsapproximation zu berechnen.

Diese Algorithmen sind in unserem Gittercode AREPO mit der Hydrodynamik über "Operator-Splitting" gekoppelt, der alternierend Hydrodynamik und Strahlung zeitentwickelt. Weiterhin diskutieren wir unsere Behandlung der, für die Reionisation grundlegenden, kosmologischen Strahlungsquellen mit Hilfe eines chemischen Netzwerks, das in der Lage ist die entsprechenden chemischen Ungleichgewichte präzise zu beschreiben. Wir zeigen eine Reihe von Test unserer Implementation, unter anderem Schattenwurf in zwei und drei Dimensionen, die Ausdehnung einer Ionisationskugel in statischem und dynamis-

---

[1]Eine Reduktion der Lichtgeschwindigkeit erlaubt längere Zeitschritte

chen Dichtefeld, sowie die Ionisation eines kosmologischen Dichtefeldes. Alle Test stimmen gut mit analytischen Rechnungen und numerischen Simulationen anderer Codes überein.

Schlussendlich vergleichen wir die Leistungsfähigkeit unserer Algorithmen, mit Hilfe einer Simulation der kosmologischen Reionisation von Wasserstoff. Als erste Näherung werden dabei stellare Winde in unseren Rechnungen vernachlässigt. Die zugrunde liegenden Simulationscodes errechnen stark unterschiedliche Sternformationsraten, die, unabhängig vom Strahlungstransport, zu grossen Abweichungen im Photonenanzahl führen. Dies allein verursacht, dass die Reionisation im GADGET bei höheren Rotverschiebungen geschieht, als im AREPO. Aus der niedrigeren Anzahl ionisierender Photonen im ersten Code resultiert ein höherer Anteil an neutralem Wasserstoff und eine andere Temperatur des kosmischen Gases im Vergleich zum Zweiten. In beiden kosmischen Reionisationsmodelle wird einen geringeren Anteil an Baryonen in leichten dunkle Materie Halos erzeugt, was eine direkte Folge des Strahlungsheizens ist. Der Effekt ist, aufgrund höherer Ionisationsgrade, stärker in den GADGET als in AREPO Simulation. Beide Simulationcodes stimmen knapp mit Beobachtungen der Lyman-α Spektrallinien. Dies war allerdings auch nicht zu erwarten, da mit den stellaren Winden ein unverzichtbarer Rückkopplungmechanismus fehlt.

Wir kommen damit zu dem Schluss, dass sich trotz der nennenswerten Unterschiede zwischen den Codes, beide im Rahmen neuester Beobachtungen zur Simulation der Wasserstoffreionisation eigenen. Es sei an dieser Stelle aber noch einmal darauf hingewiesen, dass der Verlauf der kosmischen Wasserstoffreionisation hochgradig von der Entwicklung der Sternentstehungsratendichte abhängt, die daher den unsichersten Parameter in unseren Modellen darstellt.

Summary

One of the most interesting questions in cosmology is to understand how the Universe evolved from its nearly uniform and simple state briefly after the Big Bang to the complex state we see around us today. In particular, we would like to explain how galaxies have formed, and why they have the properties that we observe in the local Universe. Computer simulations play a highly important role in studying these questions, because they allow one to follow the dynamical equations of gravity and hydrodynamics well into the non-linear regime of the growth of cosmic structures.

The current generation of simulation codes for cosmological structure formation calculates the self-gravity of dark matter and cosmic gas, and the fluid dynamics of the cosmic gas, but radiation processes are typically not taken into account, or only at the level of a spatially uniform, externally imposed background field. However, we know that the radiation field has been highly inhomogeneous during certain phases of the growth of structure, and may have in fact provided important feedback effects for galaxy formation. In particular, it is well established that the diffuse gas in the universe was nearly fully neutral after recombination at very high redshift, but today this gas is highly ionized. Sometime during the evolution, a transition to the ionized state must have occurred, a process we refer to as reionization. The UV radiation responsible for this reionization is now permeating the universe and may in part explain why small dwarf galaxies have so low luminosities. It is therefore clear that accurate and self-consistent studies of galaxy formation and of the dynamics of the reionization process should ideally be done with simulation codes that directly include a treatment of radiative transfer, and that account for all relevant source and sink terms of the radiation.

We present a novel numerical implementation of radiative transfer in the cosmological smoothed particle hydrodynamics (SPH) simulation code GADGET. It is based on a fast, robust and photon-conserving integration scheme where the radiation transport problem is approximated in terms of moments of the transfer equation and by using a variable Eddington tensor as a closure relation, following the 'OTVET'-suggestion of Gnedin & Abel. We derive a suitable anisotropic diffusion operator for use in the SPH discretization of the local photon transport, and we combine this with an implicit solver that guarantees robustness and photon conservation. This entails a matrix inversion problem of a huge, sparsely populated matrix that is distributed in memory in our parallel code. We solve this task iteratively with a conjugate gradient scheme. Finally, to model photon sink processes we consider ionization and recombination processes of hydrogen, which is represented with a chemical network that is evolved with an implicit time integration scheme. We present several tests of our implementation, including single and multiple sources in static uniform density fields with and without temperature evolution, shadowing by a dense clump, and multiple sources in a static cosmological density field. All tests agree quite well with analytical computations or with predictions from other radiative transfer codes, except for shadowing. However, unlike most other radiative transfer codes presently in use for study-

ing reionization, our new method can be used on-the-fly during dynamical cosmological simulations, allowing simultaneous treatments of galaxy formation and the reionization process of the Universe.

We carry out hydrodynamical simulations of galaxy formation that simultaneously follow radiative transfer of hydrogen-ionizing photons, based on the optically-thin variable Eddington tensor approximation as implemented in the GADGET code. We consider only star-forming galaxies as sources and examine to what extent they can yield a reasonable reionization history and thermal state of the intergalactic medium at redshifts around $z \sim 3$. This serves as an important benchmark for our self-consistent methodology to simulate galaxy formation and reionization, and for future improvements through accounting of other sources and other wavelength ranges. We find that star formation alone is sufficient for rinsing the Universe by redshift $z \sim 6$. For a suitable choice of the escape fraction and the heating efficiency, our models are approximately able to account at the same time for the one-point function and the power spectrum of the Lyman-α forest. The radiation field has an important impact on the star formation rate density in our simulations and significantly lowers the gaseous and stellar fractions in low-mass dark matter halos. Our results thus directly demonstrate the importance of radiative feedback for galaxy formation.

In search for even better and more accurate methods we introduce a numerical implementation of radiative transfer based on an explicitly photon-conserving advection scheme, where radiative fluxes over the cell interfaces of a structured or unstructured mesh are calculated with a second-order reconstruction of the intensity field. The approach employs a direct discretization of the radiative transfer equation in Boltzmann form with adjustable angular resolution that in principle works equally well in the optically thin and optically thick regimes. In our most general formulation of the scheme, the local radiation field is decomposed into a linear sum of directional bins of equal solid-angle, tessellating the unit sphere. Each of these "cone-fields" is transported independently, with constant intensity as a function of direction within the cone. Photons propagate at the speed of light (or optionally using a reduced speed of light approximation to allow larger timesteps), yielding a fully time-dependent solution of the radiative transfer equation that can naturally cope with an arbitrary number of sources, as well as with scattering. The method casts sharp shadows, subject to the limitations induced by the adopted angular resolution. If the number of point sources is small and scattering is unimportant, our implementation can alternatively treat each source exactly in angular space, producing shadows whose sharpness is only limited by the grid resolution. A third hybrid alternative is to treat only a small number of the locally most luminous point sources explicitly, with the rest of the radiation intensity followed in a radiative diffusion approximation.

We have implemented the method in the moving-mesh code AREPO, where it is coupled to the hydrodynamics in an operator splitting approach that subcycles the radiative transfer alternatingly with the hydrodynamical evolution steps. We also discuss our treatment of basic photon sink processes relevant for cosmological reionization, with a chemical network that can accurately deal with non-equilibrium effects. We discuss several tests of the new method, including shadowing configurations in two and three dimensions, ionized sphere expansion in static and dynamic density field and the ionization of a cosmological

density field. The tests agree favorably with analytic expectations and results based on other numerical radiative transfer approximations.

We compare how our schemes perform in a simulation of hydrogen reionization, excluding stellar winds due to development issues. The underlying cosmological simulation codes produce different star formation rate histories, which results in a different total photon budget. As a consequence reionization in GADGET happens at a higher redshift, i.e. sooner, than in AREPO. The lower number of ionizing photons in the latter code results in a higher volume-averaged neutral fraction at redshift $z = 3$ and a different temperature state of the baryonic gas. We find that in both reionization scenarios the baryon fraction of low mass dark matter halos is reduced due to photoheating processes and observe that the change is bigger in the GADGET simulation than in the AREPO one, which is due to the higher ionized fractions we find the in former. Both simulations compare marginally well with the Lyman-α forest observations at redshift $z = 3$, but results are not expected to be in very good agreement due the lack of the essential feedback from stellar winds in the simulations.

Finally, we can conclude that despite the differences between the two realizations, both codes perform well at the given problem and are suitable for studying the process of reionization because they produce sensible results in the limits of observations. We emphasize that the reionization history depends strongly on the star formation rate density in the simulations and which should therefore be accurately reproduced.

1 Introduction

1.1. A brief history of time

Time and space were created in the Big Bang approximately 14 Gyr ago (Komatsu et al., 2010). The first few seconds of life of the Universe were very dynamic as all known forces and elementary particles were created. In the very first second inflation took place - space expanded exponentially and increased its size by a factor of $\sim 10^{29}$. This process shaped the cosmos as it is today, stretching quantum fluctuations across the horizon and allowing for density perturbations to form. These perturbations in turn formed galaxies and clusters of galaxies.

After inflation took place, the Universe cooled adiabatically as it expanded, until at temperatures around 10^3 K at time $t \sim 400,000$ yr after the Big Bang, the radiation decoupled from the matter and allowed atoms to form through recombination. We observe this radiation in the form of the cosmic microwave background (CMB). The period directly after this last scattering surface is known as the Dark Ages - there were no luminous sources yet and therefore no observations based on electro-magnetic radiation are possible. The Dark Ages ended with the formation of the first stars and luminous galaxies and the beginning of reionization.

1.1.1. The concordance cosmological model

The most recent observations of the CMB by the Willkinson Microwave Anisotropy Probe (WMAP) were used to derive the following cosmological parameters: $\sigma_8 = 0.8$, $H_0 = 70.4\,, \mathrm{km\,s^{-1}\,Mpc^{-1}}$, $\Omega_\Lambda = 0.73$, $\Omega_\mathrm{m} = 0.27$, and $\Omega_\mathrm{b} = 0.045$ (Komatsu et al., 2010), where σ_8 is the present linear-theory mass dispersion on a scale of $8h^{-1}\,\mathrm{Mpc}$, H_0 is the Hubble expansion rate, Ω_Λ is the dark energy density parameter, Ω_m is the matter density parameter, and Ω_b is the baryon density parameter.

The current cosmological model, outlining the evolution of the Universe, is called ΛCDM - cold dark matter with a cosmological constant. It describes the Universe as flat and homogeneous on large scales, and expanding at an accelerating rate today, evolving originally from a uniform distribution of low velocity dark matter. The initial perturbations in the

density field are described by the primordial power spectrum, whose slope is $n_{\mathrm{s}} = 0.96$ as measured by WMAP (Komatsu et al., 2010). Currently the Universe has a web-like structure, where most of the objects are located along filaments and in galaxy clusters, that lie at the junctions of these filaments. Structures form hierarchically as small objects merge together to form larger ones.

1.2. Reionization of the Universe

1.2.1. The Process of Reionization

In the standard cosmological model, the primordial gas recombines and becomes neutral around redshift $z \simeq 1000$. However, the absence of Gunn-Peterson troughs in the spectra of high redshift quasars up to $z \leq 6$ (White et al., 2003; Fan et al., 2006a) suggests that hydrogen is highly ionized at low redshift. Thus, there must be a period in the history of the Universe when hydrogen became ionized again, but it is still an open question when the process of this *cosmic reionization* started, how it proceeded in detail, and which sources of radiation were primarily responsible for it.

In the literature, predictions based on simulations for the onset of reionization range from redshifts $z \sim 30 - 40$ (Iliev et al., 2007; Wise & Abel, 2008) to $z \sim 15 - 20$ (Norman et al., 1998; Abel et al., 2002), depending on the formation time of the first luminous sources. Reionization then proceeds in an inhomogeneous and patchy fashion (Lidz et al., 2007; Iliev et al., 2007), reflecting the inhomogeneous density distribution of the large-scale structure. At first, many isolated ionized bubbles are formed. They then grow in size from $\sim 1\,\mathrm{Mpc}$ during the early stages of reionization up to $> 10\,\mathrm{Mpc}$ in the late phases (Furlanetto et al., 2006; Iliev et al., 2006). It remains an open question whether reionization proceeds from high to low density region, also know as the *inside-out* model (Iliev et al., 2006) or from low to high density regions - the *outside-in* model (Gnedin, 2000). Around redshift $z \sim 13$ (Iliev et al., 2006), $8 < z < 10$ (Lee et al., 2008), or $z \sim 6$ (Gnedin & Fan, 2006), the ionized regions overlap. The duration of reionization is also highly speculative between different groups. However, recently an all-sky observation of the mean 21cm line emission by Bowman & Rogers (2010) gave a lower limit on the duration of reionization, $\Delta z > 0.06$. The theoretical estimates for the aforementioned quantities, obtained by numerical simulations, are very uncertain and depend strongly on the modeling details of reionization and the parameters of the underlying galaxy formation simulations. However, it is plausible that the future use of more self-consistent simulation techniques should be able to reduce the systematic modeling uncertainties.

An important observational clue about reionization is provided by the total electron-scattering optical depth to the last scattering surface of the CMB, found to be $\tau_{\mathrm{es}} = 0.08785 \pm 0.00072$ by the WMAP seven-year data release (Larson et al., 2010). This points to an early start and possibly extended period of reionization. Further observational information about the history of hydrogen reionization can be inferred through various astrophysical phenomena: the Gunn-Peterson troughs in quasar spectra are sensitive to small

trace amounts of neutral hydrogen during the late stages of reionization ($z \sim 6$); the 21-cm line background and gamma ray bursts (GRBs) probe the early stages of reionization, when the Universe was mostly neutral ($10 < z < 30$); and finally, the CMB polarization provides important data on the free electron column density integrated over a large range of redshifts (Alvarez et al., 2006), see Fan et al. (2006) for a detailed review. In the future, upcoming observations from new radio telescopes such as LOFAR (Low Frequency Array) (Falcke et al., 2007) promise to be able to map out the epoch of cosmic reionization in unprecedented detail.

Numerous theoretical studies have begun to investigate the characteristic scales and the topology of the reionization process through the use of numerical simulations (e.g. Gnedin & Ostriker, 1997; Miralda-Escudé et al., 2000; Gnedin & Abel, 2001; Ciardi et al., 2003; Sokasian et al., 2004; Iliev et al., 2006; Zahn et al., 2007; Croft & Altay, 2008; Shin et al., 2008; Wise & Abel, 2008; Geil & Wyithe, 2008; Alvarez et al., 2009; Thomas et al., 2009; Mesinger, 2010; Petkova & Springel, 2010). However, due to the high computational cost and complexity of the radiative transfer problem, most simulations, with very few exceptions (Gnedin & Ostriker, 1997; Kohler et al., 2007; Shin et al., 2008; Wise & Abel, 2008; Petkova & Springel, 2010), have treated reionization through post-processing, applied to static or separately evolved gas density fields. This neglects the fact that the radiation field may exert important feedback effects on galaxy formation itself (e.g. Iliev et al., 2005; Yoshida et al., 2007; Croft & Altay, 2008). It is therefore an important task to develop more accurate theoretical models based on self-consistent simulations, where the ionization field is evolved simultaneously with the growth of cosmic structures, a topic that we address in this work.

1.2.2. Observing reionization

The epoch of reionization has not been directly observed to date. Together with the Dark Ages after recombination, it is one of the most speculative epochs in the evolution of the Universe. However, some observations, discussed below, are able to give several important constraints of the process.

Gun-Peterson Troughs

The Lyman-α absorption in the spectra of high redshift quasars is a direct probe for the neutral hydrogen density in the inter galactic medium (IGM) at high redshifts (Gunn & Peterson, 1965). Neutral hydrogen clouds along the line of sight of a quasar create absorption patterns in the spectrum at the redshifted Lyman-α wavelength. These features are called the Lyman-α forest.

The Gunn-Peterson optical depth to the Lyman-α photons as a function of redshift z is

$$\tau_{\mathrm{GP}}(z) = 4.9 \times 10^5 \left(\frac{\Omega_0 h^2}{0.13} \right)^{-0.5} \left(\frac{\Omega_{\mathrm{b}} h^2}{0.02} \right) \left(\frac{1+z}{7} \right) x_{\mathrm{HI}}, \tag{1.1}$$
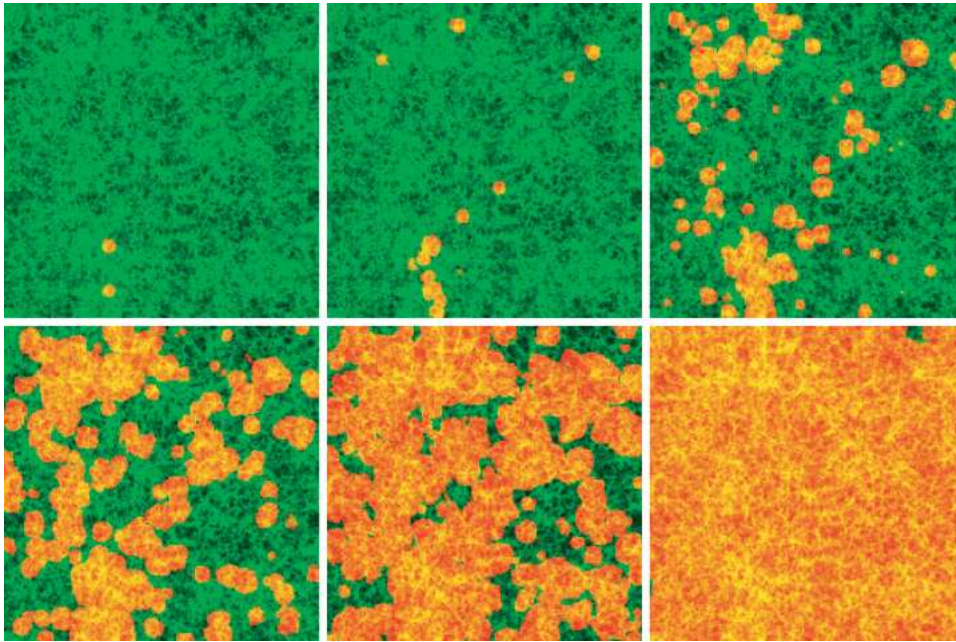
Figure 1.1: Slices through the volume of a simulation of reionization (carried out by Iliev et al., 2006) at redshifts z = 18.5, 16.1, 14.5, 13.6, 12.6 and 11.3. Shown are the density field (green in neutral regions, yellow in ionized regions) and the HII regions (red). The HII regions grow around sources, tracing the high-density regions and then escape into the voids, finally overlapping - the end of reionization.

where Ω_0 is the matter density of the Universe, $\Omega_{\rm b}$ is the baryon density parameter, h is the Hubble factor and $x_{\rm HI}$ is the neutral hydrogen fraction. The optical depth becomes large already for neutral factions as small as 10^{-4}. Therefore this parameter is only relevant for the end stages of reionization, as the absorption saturates at the early stages, when the gas is mostly neutral.

Gunn-Peterson troughs have been detected in many high redshift quasars from the Sloan Digital Sky Survey (York et al., 2000). The first significant detection is made by Becker et al. (2001), who report an optical depth $\tau_{\rm eff} > 5$ at redshift $z > 6$. Further detections of quasars have provided more data for analysis (Fan et al., 2003; Fan, 2004; Fan et al., 2006a; Fan, 2007). Fan et al. (2002) report a neutral hydrogen fraction of $x_{\rm HI} > 10^{-3}$ and effective Gunn-Peterson optical depth $\tau_{\rm GP} > 5$ at redshift $z \sim 6$. White et al. (2003) report an optical depth $\tau_{\rm Lyman-\alpha} > 22$ at redshift $z > 6$, inferred from the spectra of eight quasars. Songaila (2004) show from an analysis of the Lyman-α forest that the transmitted Lyman-α flux drops below 10% at redshift $z > 5.5$. These values indicate that the IGM neutral hydrogen fraction is $10^{-3.5} < x_{\rm HI} < 10^{-0.5}$ at redshift $z \sim 6$. Fan et al. (2006b) detect a steepening in the evolution of the Gunn-Peterson optical depth with redshift. The dependence goes from $\tau_{\rm GP} \sim (1+z)^{4.3}$ to $\tau_{\rm GP} \sim (1+z)^{>11}$ at redshift $z > 5.7$ (see Figure 1.2). They also infer the average size of neutral hydrogen clouds from
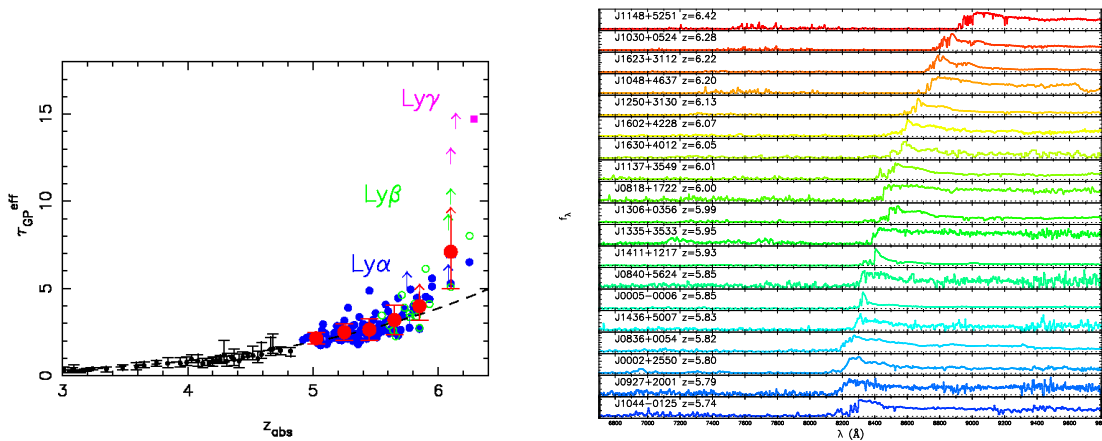
Figure 1.2: Gun-Peterson optical depth versus redshift, obtained from the spectra of high redshift quasars (Fan et al., 2006b). There is a steep increase at redshift $z \sim 6$.

the Lyman-α forest. It changes from less than 10 Mpc to more than 80 Mpc at optical depth $\tau_{GP} > 3.5$. An increase by a factor of 10 of the neutral fraction between redshift $z = 5.7$ and $z = 6.4$ is also observed. Willott et al. (2007) analyze the spectra of high redshift quasars observed by the Canada-France High-z Quasar Survey and find an optical depth of $\tau_{GP} = 5.25$ at redshift $z \sim 6$.

All of the studies above point out that a change in the Lyman-α optical depth is present around redshift $z \sim 6$. This could be a possible clue that reionization was completed around that redshift.

Cosmic Microwave Background

The CMB was created from the last scattering surface, when hydrogen recombined and photons were set free. The radiation has black body spectrum with effective temperature $T = 2.725(1 + z)$ K with fluctuations on all scales, as small as 10^{-5} K. The all sky signal can be decomposed into spherical harmonics and expressed as an angular power spectrum. It provides information about the physics of the early Universe along with the interplay between dark matter, baryons and radiation. Free electrons released through ionizations cause damping proportional to $e^{-\tau_{es}}$, where τ_{es} is the electron Thomson scattering optical depth. The bulk motions of free electrons during the patchy stages of reionization produce a signal in the temperature anisotropies on small angular scales - $l > 2000$ (e.g. Santos et al., 2003; Doré et al., 2007).

Another way to use CMB data to constrain reionization is the CMB E-mode polarization. It is created primarily through Thomson scattering off free electrons. A plot of the temperature–E-mode (TE) cross-correlation angular power spectrum is shown in Figure 1.3. The re-scattering of the CMB photons due to reionization adds to the amplitude at large angular scales ($l < 10$). The position of this peak is proportional to the square root of the reionization redshift $l_{peak} \propto 2\sqrt{z_{reion}}$ (Zaldarriaga, 1997), assuming instanta-
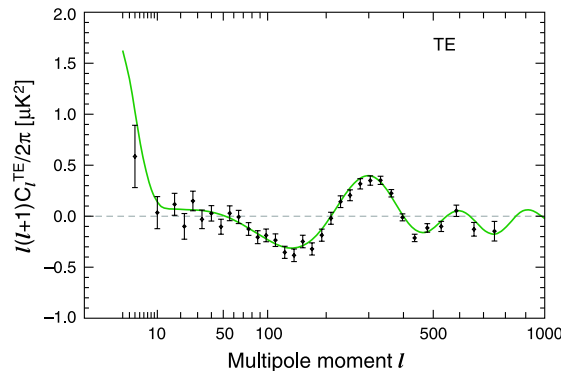
Figure 1.3: Temperature – E-mode polarization cross-correlation angular power spectrum from the 7-year WMAP data (Larson et al., 2010). The peak at multipole moment $l < 10$ corresponds to reionization. The green line is the best-fit ΛCDM model.

neous reionization. An analysis of the latest 7-year WMAP data release shows that the Thomson electron scattering optical depth to the last scattering surface is consistent with an instantaneous reionization at $z_{\mathrm{reion}} \sim 10.5 \pm 1.2$ (Larson et al., 2010). Results will significantly increase in accuracy as data from the state-of-the-art microwave satellite PLANCK (Tauber et al., 2010) becomes available.

21cm line tomography

The ground state of hydrogen exhibits a hyperfine spin-flip transition caused by the different possible spin states of the proton and the electron. The energy difference between the two states has a wavelength of 21 cm. The emission line lies in the radio range, which makes it convenient for ground-based observations. The importance of this transition is that it can be used to observationally determine an all-sky map of the neutral hydrogen distribution. Therefore, mapping the 21cm emission at different redshifted frequencies, according to: $\nu = 1420/(1 + z)\,\mathrm{MHz}$, can provide 3D information about the distribution of neutral hydrogen at different times during reionization and beyond.

The spin temperature of hydrogen, T_{S}, depends on the CMB temperature T_{CMB}, the temperature of the gas T_{K}, and the temperature of the Lyman-α radiation field $T_{\mathrm{Ly}\alpha}$ (Field, 1959). The brightness temperature T_{B} of the 21cm emission depends on both T_{S} and T_{CMB} and is given by:

$$T_{\mathrm{B}}(\theta, z) \sim 7(1 + \delta)x_{\mathrm{HI}} \left(1 - \frac{T_{\mathrm{CMB}}}{T_{\mathrm{S}}}\right)(1 + z)^{0.5}\mathrm{mK}, \tag{1.2}$$

where θ is the position on the sky and δ is the local overdensity of hydrogen.

At very high redshift, $z > 200$, the spin temperature T_{S} is coupled to the CMB temperature T_{CMB} and no signal from the 21 cm line is detected. At redshifts $200 > z > 40$, hydrogen starts to cool adiabatically and the temperature of the CMB becomes larger than the spin temperature. Thus, the brightness temperature of the 21cm line is seen in
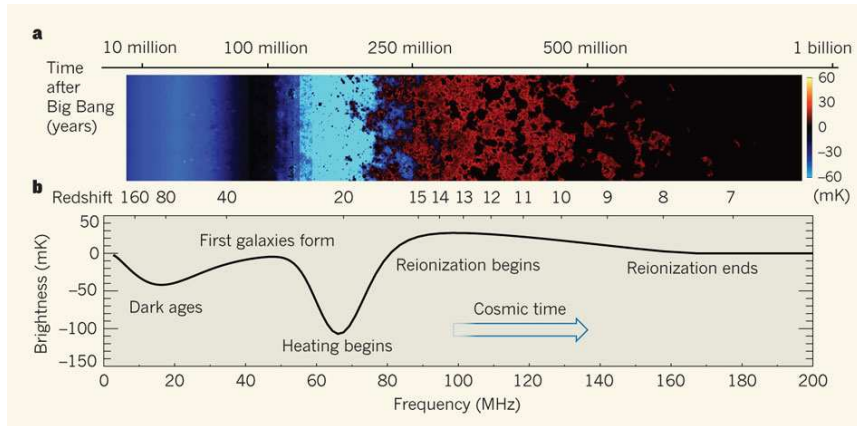
Figure 1.4: Brightness temperature of the 21cm line, seen relative to the CMB temperature. The upper panel shows a spatial view of the fluctuations and the lower panel describes the different epochs, relevant for the evolution of the 21cm signal (Pritchard & Loeb, 2010).

absorption relative to the CMB. Around redshift $z \sim 40$, structure formation has already began, but sources of ionizing photons are scarce and therefore can be ignored. In this era the spin temperature can not be differentiated from the CMB and no signal is seen. Some exceptions are minihalos - virialized objects with overdensity $\delta \sim 200$ (Iliev et al., 2002; Furlanetto & Oh, 2006) and shock-heated filaments (Furlanetto & Briggs, 2004). The objects are heated and the spin temperature equals the gas temperature, thus the 21cm line is seen in emission. In the third epoch around redshift $z \sim 25$, luminous sources begin to ionize the gas. The spin temperature falls below the CMB and the gas is seen in absorption. In the fourth epoch at $z \sim 20$ local heating from X-Ray sources and quasars rises spin temperatures above the CMB and the brightness temperature is then be observed in emission. If uniform heating happened earlier than reionization, the 21cm fluctuations become independent of the temperature field (Furlanetto & Briggs, 2004; Loeb, 2007) and depend only on overdensity. This complicated time evolution of T_{B} is illustrated in Figure 1.4 in more detail.

There have been several numerical and semi-analytical studies (e.g. Ciardi & Madau, 2003; Gnedin & Shaver, 2004; Furlanetto & Briggs, 2004; Santos et al., 2008; Mellema et al., 2006; Zaldarriaga et al., 2004; Pritchard et al., 2010) of the 21cm brightness temperature power spectrum at different redshifts. We point the reader to Morales & Wyithe (2010) for a recent review on studying reionization with 21cm fluctuations.

21 cm line - CMB cross-correlation

Even though the 21 cm signal can ideally present a 3D map of the neutral hydrogen sky, future observations may be highly contaminated by foreground sources, e.g. radio halos (Jelić et al., 2008; Rudnick et al., 2009). Cross-correlations between the 21 cm signal and
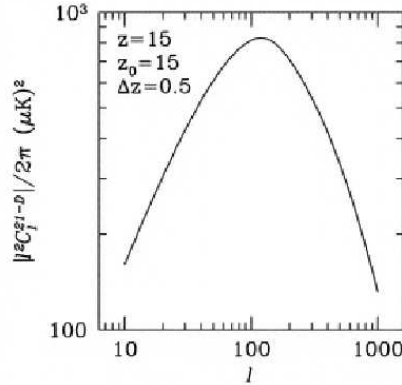
Figure 1.5: Doppler CMB anisotropies – 21 cm cross-correlation angular power spectrum model, assuming reionization at redshift $z = 15$ with duration $\Delta z = 0.5$.

the E-mode polarization of the CMB may be a more powerful tool as the relative error will be reduced.

The velocities of ionized baryons induce Doppler anisotropies in the CMB that trace gas overdensities and therefore correlate positively with the 21 cm signal. The signal peaks at angular scales $l \sim 100$ at large physical scales $k \sim 10^{-2}\,\mathrm{Mpc}^{-1}$, where structure formation is linear (Alvarez et al., 2006; Adshead & Furlanetto, 2008). Since the cross-correlation relates a signal from ionized gas to a signal from neutral gas, it peaks at redshift where the global neutral fractions is $x_{\mathrm{HI}} = 0.5$. A model of the signal is shown in Figure 1.5.

Gamma Ray Bursts

Gamma ray bursts are believed to originate from the collapse of compact objects, such as neutron stars or massive stars. Since galaxy masses decrease towards higher redshift, the luminosity of quasars also tends to decrease with increasing redshift. The GRB luminosities, however, do not depend on the mass of the host-galaxy, outshine any other high-redshift source, and are detected as far as redshift $z = 8.1$ (Salvaterra et al., 2009), which makes them potential unique probes for reionization.

The time evolution and statistics in the absorption portions of a GRB afterglow spectrum present a unique opportunity to study different reionization models. Totani et al. (2006) give an upper limit of $x_{\mathrm{HI}} < 0.6$ on the IGM neutral fraction at redshift $z = 6.3$ by fitting an Lyman-α absorption profile to the spectra of GRB 050904; Gallerani et al. (2008) find a neutral fraction $x_{\mathrm{HI}} = 7 \pm 4 \times 10^{-4}$ at redshift $z \sim 6$; and Patel et al. (2010) pose an upper limit of $x_{\mathrm{HI}} < 0.73$ at redshift $z = 6.7$. These results are, however, of weak statistical power as they are based on the analysis of only three GRB afterglow spectra. McQuinn et al. (2008) compute that the global neutral fraction of the Universe can be estimated no better than $\delta x_{\mathrm{HI}} \sim 0.3$ from a single GRB spectrum since individual lines of sight are not representative due to the patchy nature of reionization. Therefore we need a
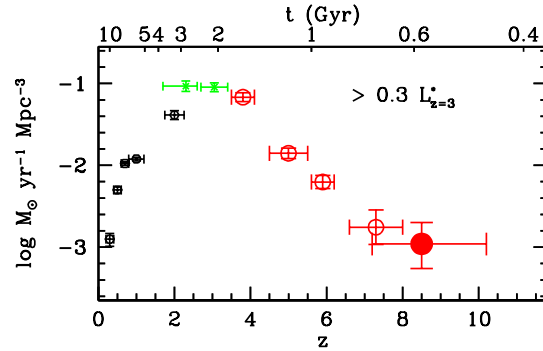
Figure 1.6: Cosmological star formation rate density, composed of different surveys and combined by González et al. (2010)

much larger sample of GRB spectra in order to study reionization.

1.2.3. Sources of Ionizing Photons

Assuming that the Universe is fully ionized since redshift $z \sim 6$, we can estimate the minimum required photon luminosity to keep it ionized:

$$\dot{N}_{\mathrm{ion}}(z) = 10^{51.2} \mathrm{s}^{-1} \, \mathrm{Mpc}^{-3} \frac{C}{30} \left(\frac{1+z}{6} \right)^3 \left(\frac{\Omega_{\mathrm{b}} h^2}{0.0457} \right), \qquad (1.3)$$

where $C = \langle n_{\mathrm{H}}^2 \rangle / \langle n_{\mathrm{H}} \rangle^2$ is the clumping factor (Miralda-Escudé et al., 2000). The main sources of these ionizing photons are quasars and stars. Some more exotic candidates include annihilation radiation and particle decay (Fan et al., 2006), but they go beyond the scope of this work and we will therefore not discuss them here.

Quasars are very luminous and emit radiation over a broad range of frequencies, which makes them perfect candidates for sources of ionizing photons. Observations show that they dominate the UV background at redshift $z \sim 2.5$ (Haardt & Madau, 1996), but the density function of luminous quasars ($M_{1450} < -27$) declines exponentially thereafter and drops by a factor of 40 by redshift $z \sim 6$ (e.g. Fan, 2004; Richards et al., 2006). As the quasar density decreases faster than the stellar density for redshift $z > 3$, the UV background becomes dominated by stellar sources at higher redshift (Haehnelt et al., 2001).

For the aforementioned reasons, most theoretical models assume stars to be the primary sources for reionization photons. However, there are big uncertainties about the total stellar UV photon emissivity at high redshifts (Fan et al., 2006). Madau et al. (1999) predict a critical star formation rate (SFR) density needed to reionize the Universe by redshift $z \sim 6$

$$\dot{\rho}_{\mathrm{SFRD}}^{\mathrm{crit}} = \frac{0.04 \mathrm{M}_{\odot} \, \mathrm{yr}^{-1} \, \mathrm{Mpc}^{-3}}{f_{\mathrm{esc}}} \left(\frac{1+z}{7} \right)^3 \left(\frac{\Omega_{\mathrm{b}} h^2}{0.0457} \right)^2 \left(\frac{C}{30} \right), \qquad (1.4)$$

where f_{esc} is the escape fraction of UV photons from galaxies (discussed in the next section). A composite of the observed cosmic SFRD, compiled by González et al. (2010) from different sources, is shown in Figure 1.6. The observed values are lower than the theoretical prediction in equation (1.4), even for an escape fraction of 100%, which suggests there are not enough ionizing photons from stellar sources to reionize the Universe by redshift $z = 6$. This may hint that we are still not able to observe sufficiently well high-redshift faint sources, such as dwarf galaxies, and that the current observational estimate of the SFR density is still affected by systematic biases.

Another way to categorize the sources of ionizing photons is by the size of the galaxy DM halo they originate from. In many scenarios, reionization is assumed to be driven mainly by high-mass objects with mass $M_{\mathrm{DM}} > 10^9 \, M_\odot$ (Ciardi et al., 2000). However, the dim, but abundant low mass sources ($M_{\mathrm{DM}} < 10^9 \, M_\odot$) may still strongly influence the way in which the ionized regions grow and provide a substantial part of the ionizing photon budget, approximately 80% at $z \sim 7$ (Sokasian et al., 2003; Choudhury & Ferrara, 2007). These small galaxies are preferentially found in low-density environments along the cosmic web and may contain many metal-free population III stars in the early Universe. Disregarding them may lead to an overestimate of the number of photons required to reionize the Universe (Sokasian et al., 2003).

1.3. Simulating reionization

There are several critical aspect in simulating cosmological reionization: simulation volume and resolution, escape fractions, and the numerical treatment of radiative transfer. In the following sections we will discuss these issues in more detail.

1.3.1. Notes on the resolution

An important aspect in simulating a sensible reionization history is the box size of the simulation. A cosmological box has to be big enough to be representative of the whole Universe and to limit the cosmic variance. Aside from this cosmological requirement, the volume has to fit to reionization specifications as well. Considering this and the typical ionized bubble sizes at redshift $z = 6$ of $10 \, \mathrm{Mpc}$, it is often assumed that desirable box sizes are of the order of $100 h^{-1}$ comoving Mpc (Iliev et al., 2006; Shin et al., 2008). Moreover, as the evolution of the neutral fraction in a void region is very different than in a proto-cluster region (Ciardi et al., 2003; Furlanetto & Oh, 2005; Furlanetto & Mesinger, 2009) large volumes are desirable. Since reionization takes place in voids as well as in high density regions, spatial and mass resolution of the discretized elements are also very important. Therefore, there is often a trade-off made between box size and particle or cell resolution (e.g. Ciardi et al., 2003; Zahn et al., 2007; Croft & Altay, 2008; Petkova & Springel, 2010), where a compromise between a smaller volume of the order of $10^3 - 60^3 h^{-3} \, \mathrm{Mpc}^3$ and a higher resolution is made.

Another constraint on the total volume and mass resolution of simulations, relevant for
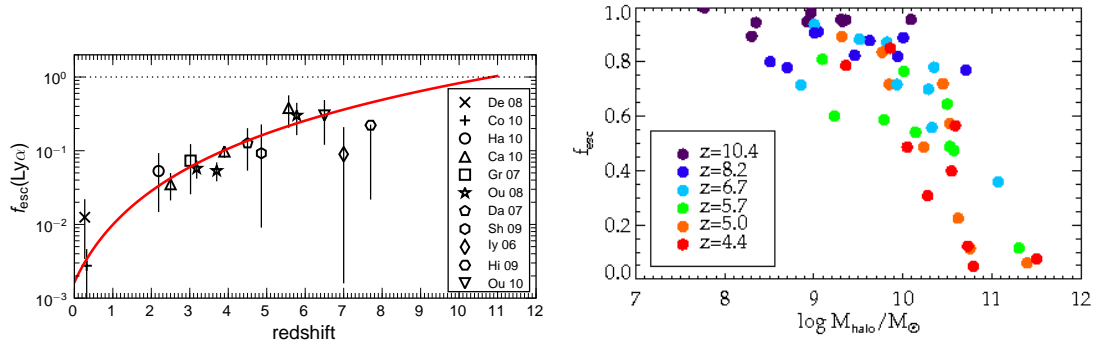
Figure 1.7: Left panel: escape fractions from different galaxy surveys compiled by Hayes et al. (2010). Right panel: escape fractions evolution with halo mass and redshift from simulations by Razoumov & Sommer-Larsen (2010).

reionization, is postulated by Bolton & Becker (2009). They argue that a minimum box size of $10h^{-1}$ Mpc and particle mass of $1.61 \times 10^6 h^{-1}\,M_\odot$ in smoothed particle hydrodynamics simulations are necessary to reproduce realistic Lyman-α absorption spectra.

1.3.2. Escape fractions

The UV escape fraction f_{esc} of galaxy halos is defined as the ratio between photons that leave the halo compared to the total number of originally emitted photons. There is no universal escape fraction since dust obscuration and internal absorption change from galaxy to galaxy. The most recent report on Lyman-α escape fractions in high redshift galaxies by Blanc et al. (2010) give a median value of $f_{\mathrm{esc}} = 0.22 \pm 0.04$ for a sample at redshift $2.8 < z < 3.8$. Hayes et al. (2010) present a review of known escape fractions from other authors (see left panel of Figure 1.7) and find an evolution with redshift, described by $f_{\mathrm{esc}} \propto (1 + z)^{2.6 \pm 0.2}$ for redshift range $0.3 < z < 6$.

There have also been numerous numerical studies of galaxy halo escape fractions, combining high resolution simulations with recipes for star formation and feedback. Ricotti & Shull (2000) present a parameter study to understand the dependence of the escape fraction on redshift, halo mass, baryon fraction, star formation efficiency, and luminosity. They find that escape fractions increase from high mass to low mass halos, and decrease with resolution over all mass ranges.

More recently, Gnedin et al. (2008) examined high resolution halos with mass $M > 10^{11}\,M_\odot$ and found escape fractions $f_{\mathrm{esc}} = 0.01 - 0.03$ over redshift range $3 < z < 9$. Wise & Cen (2009) study high-redshift dwarf galaxies with mass $M < 10^{9.5}\,M_\odot$, since they are considered of crucial importance for driving reionization. They find an escape fraction of $f_{\mathrm{esc}} = 0.5$ at the lower mass range $M \sim 5 \times 10^6\,M_\odot$, and $f_{\mathrm{esc}} = 0.8$ for $M \sim 5 \times 10^6\,M_\odot$. Razoumov & Sommer-Larsen (2010) present results from high resolution simulations, summarized in the right panel of Figure 1.7. Their estimate of the escape fractions decreases with redshift and increases with mass.
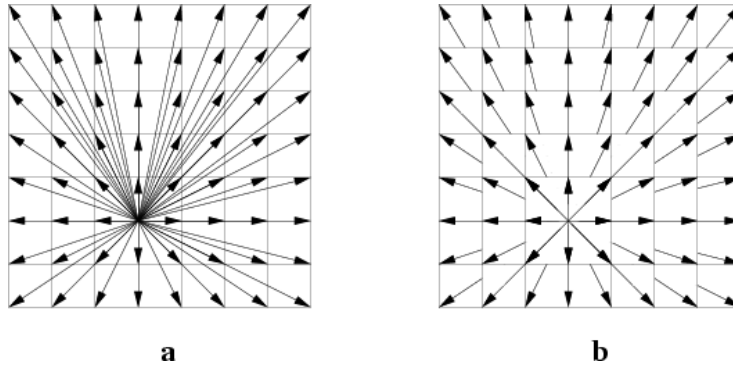
Figure 1.8: An example of long (left) and short (right) characteristics method. Figure from Rijkhorst et al. (2006).

All studies find that there is no universal escape fraction. Values differ with ionization rate (Ciardi et al., 2002), line of sight orientation (Gnedin et al., 2008), star formation history and duration (Wise & Cen, 2009), and other factors (Ricotti & Shull, 2000).

1.3.3. Numerical radiative transfer

The transport of radiation and its interaction with matter is of fundamental importance in astrophysics, playing a crucial role in the formation and evolution of objects as diverse as stars, black holes, or galaxies. It would therefore be highly desirable to be able to calculate radiative transfer (RT) processes with equal accuracy and ease as ordinary hydrodynamical and gravitational dynamics. Unfortunately, the difficult mathematical structure of the radiative transfer equation, which takes the form of a partial differential equation in six dimensions (3 spatial dimensions, 2 angular dimensions, 1 frequency dimension) makes this an extremely challenging goal. In fact, the RT problem is so hard, even in isolation, that coupled radiation hydrodynamics methods are still in their infancy in cosmology thus far.

However, a large array of different approximations to the RT problem have been developed over the years, which are often specifically tuned to the requirements and characteristics of particular types of problems, and in many cases are applied to static density fields only. In this study, we are primarily concerned with RT in calculations of cosmological reionization and in star formation, leaving aside other important areas such as stellar atmospheres and accretion disks. Especially for the reionization problem, recent years have seen a flurry of activity in the development of new RT solvers that are well suited to this problem. These numerical methods include long and short characteristics schemes, ray-tracing, moment methods and direct solvers, and other particle- or Monte-Carlo-based transport methods. In the following we briefly describe these schemes.

Long and short characteristics methods

In the long characteristics method (Mihalas & Weibel Mihalas, 1984; Abel et al., 1999; Sokasian et al., 2001; Cen, 2002; Abel & Wandelt, 2002; Razoumov & Cardall, 2005; Susa, 2006) (see left panel of Figure 1.8), each source cell in the computational volume is connected to all other relevant cells. Then the RT equation is integrated individually from that cell to each of the selected cells. While this method is relatively simple and straightforward, it is also very time consuming, since it requires $\mathcal{O}(N^2)$ interactions between the cells. Moreover, parallelization of this approach is cumbersome and requires large amounts of data exchange between the different processors.

Short characteristics methods (Kunasz & Auer, 1988; Nakamoto et al., 2001; Mellema et al., 1998, 2006; Shapiro et al., 2004; Whalen & Norman, 2006; Alvarez et al., 2006; Ahn & Shapiro, 2007; Altay et al., 2008; Ciardi et al., 2001; Maselli et al., 2003; Gritschneder et al., 2009; Cantalupo & Porciani, 2010; Hasegawa & Umemura, 2010; Baek et al., 2009) (see right panel of Figure 1.8) try to gain efficiency by integrating the equation of radiative transfer only along lines that connect nearby cells, and not to all other cells in the computational domain. This reduces the redundancy of the computations and makes the scheme easier to parallelize.

A widely used incarnation of the long-characteristics method are so-called ray-tracing schemes. Here a discrete number of rays is traced from each source, along which the RT equation is integrated in 1D, considering absorptions and recombinations. As the angular resolution decreases with increasing distance from the source, rays may be split into subrays (e.g. Abel & Wandelt, 2002; Trac & Cen, 2007) for higher efficiency. The ray-tracing itself can be performed either on grids (Mellema et al., 2006; Whalen & Norman, 2006) or using particles as interpolation points (Baek et al., 2009; Gritschneder et al., 2009; Altay et al., 2008). Other innovative methods trace photons on unstructured grids, for example Delaunay tessellations, that are adapted to the mean photon optical depth of the gas (Rijkhorst et al., 2006; Paardekooper et al., 2010; Ritzerveld & Icke, 2006).

Stochastic Monte Carlo methods

Stochastic integration methods, specifically Monte Carlo methods, employ a ray-casting strategy where the rays are discretized into photon packets (Maselli et al., 2003; Baek et al., 2009) or particles (Nayakshin et al., 2009). For each photon packet, its frequency and its direction of propagation are determined by sampling the appropriate distribution function of the emitters that have been assigned in the initial conditions. A particular advantage of this approach is that comparatively few approximations to the radiative transfer equations need to be made, so that the quality of the results is primarily a function of the number of photon packets employed, which can be made larger in proportion to the CPU time spent. A disadvantage of these schemes is the comparatively high computational cost and the sizable level of noise in the simulated radiation field, which only slowly diminishes as more photon packets are used. The 'cone' transport scheme of (Pawlik & Schaye, 2008), where radiation is directly transferred between particles, tries to improve on these limitations. If

needed, this method can also create further sampling points dynamically to improve the resolution locally.

Moment methods

Using moments of the radiative transfer equations instead of the full set of equations can lead to very substantial simplifications that can drastically speed up the calculations. In this approach, the radiation is represented by its mean intensity field throughout the computational domain, which is evolved either in a diffusion approximation or based on a suitably estimated local Eddington tensor (Gnedin & Abel, 2001; Aubert & Teyssier, 2008; Petkova & Springel, 2009; Finlator et al., 2009). Instead of following rays, the moment equations are solved directly on the grid, or in a mesh-less fashion on a set of sampling particles. Due to its local nature, the moment approach is comparatively easy to parallelize, but its accuracy is highly problem dependent, making it difficult to judge whether the simplifications employed still provide sufficient accuracy. The simplest and most popular moment method is radiative diffusion (e.g. Whitehouse et al., 2005; Reynolds et al., 2009), where the RT equation is approximated in terms of an integrated energy density in each discretized mass or volume element, and this radiation energy density is then evolved through the flux-limited diffusion approximation, where the flux limiter is introduced to prevent the occurrence of transfer speeds larger than the speed of light. While the diffusion approximation works very well in the optically thick regime, its accuracy is hard to judge in general situations.

Implications

It is very difficult to evaluate the accuracy and efficiently of all the methods, relative to each other. Iliev et al. (2006a) and Iliev et al. (2009) have compiled a radiative transfer code comparison study, showing test results from more than ten codes. The tests include Strömgren sphere expansion, static cosmological density field ionization, minihalo evaporation, and others. Most codes give accurate results and agree well with each other. However, it is still unclear how they compare in a more sophisticated setting, such as a reionization simulation. In these cases other factors come into play, like the treatment of star formation and radiative cooling.

Another aspect to be considered about RT codes is the speed and efficiency of the calculation. Solving the RT equation can take up most of the computing time for a dynamic cosmological simulation. A slow-down of the code due to these computations of the order of five can be considered reasonable. A higher slow-down would be prohibitive and undesirable. Code parallelization is very important in this respect as well. The demand for larger boxes, higher resolution and faster computational times requires that multiple processors are used. As shown in Table 1 in Iliev et al. (2006a), and in Table 1 in Iliev et al. (2009), many of the current RT codes are serial, which can be a drawback when it comes to reionization simulations.

It is important to note that RT codes can be used for simulating other astrophysical

problems as well. Those, among others, include stellar spectra calculations, star formation in molecular clouds and galaxy formation. Therefore, issues such as parallelization can be rather problem dependent and should not be considered in isolation for the particular RT method.

Another aspect of RT codes is their ability to handle multiple frequency ranges. As shown in Iliev et al. (2006a) and Iliev et al. (2009), some implementations are able to evolve many photon wavelengths and therefore give more accurate predictions of the thermal and ionization state of the gas. However, the treatment of multiple frequencies usually implies a very large increase in computational cost and is therefore avoided by most applications. Iliev et al. (2006a) and Iliev et al. (2009) show that single frequency schemes perform very well compared to multi-frequency ones in the given tests and are therefore a preferred choice for reionization simulations.

The final aspect to consider about RT codes is whether they are used on-the-fly – self-consistently with the hydrodynamics of the gas – or as post-processing. Simultaneous treatment of the gas and RT requires more computational power and therefore many codes evolve the RT equation as post-processing on outputs from simulations. However, such separated treatments miss the feedback effects of radiation hydrodynamics, which are important for problems like galaxy formation (e.g. Iliev et al., 2005; Yoshida et al., 2007; Croft & Altay, 2008)

1.4. Thesis outline

The aim of this thesis is to develop a novel numerical implementation of radiative transfer and simulate self-consistently the hydrogen reionization of the Universe.

In Chapter 2 we present a new numerical implementation of radiative transfer in the cosmological smoothed particle hydrodynamics (SPH) simulation code GADGET. We present several tests of our implementation, including single and multiple sources in static uniform density fields with and without temperature evolution, shadowing by a dense clump, and multiple sources in a static cosmological density field. All tests agree quite well with analytical computations or with predictions from other radiative transfer codes, except for shadowing.

In Chapter 3 we present our results from hydrodynamical simulations of galaxy formation that simultaneously follow radiative transfer of hydrogen-ionizing photons, based on the optically-thin variable Eddington tensor approximation as implemented in the GADGET code. We show that the radiation field has an important impact on the star formation rate density in our simulations and significantly lowers the gaseous and stellar fractions in low-mass dark matter halos. Our results thus directly demonstrate the importance of radiative feedback for galaxy formation.

In Chapter 4 we present another innovative and novel method for the treatment of radiative transfer, that has been implemented in the moving-mesh code AREPO. We present several diverse tests of the implementation, including multiple shadowing configurations in two and three dimensions, isothermal ionized sphere expansion and static cosmological

density field ionization. Finally, we present a self-consistent hydrogen reionization simulation based on this method and compare to results obtained by using our moment-based scheme.

2

An implementation of radiative transfer in the cosmological simulation code GADGET

Based on Petkova, M., & Springel, V., 2009, MNRAS, 396, 1383

2.1. Introduction

In this work we develop a moments method that is closely related in spirit to the Optically Thin Variable Eddington Tensor (OTVET) scheme proposed by Gnedin & Abel (2001). However, we try to implement it directly on top of the irregular set of positions sampled by the particles of Smoothed Particle Hydrodynamics (SPH) simulations, and we use quite different numerical techniques to solve the resulting transport equations. In OTVET, the system of moment equations is closed by estimating the local Eddington tensor with a simple optical thin approximation, i.e. one pretends that all sources of light are 'visible' at a given location. Once the Eddington tensors are found, the local radiation transfer reduces to an anisotropic diffusion problem. The particular attraction of this moment-based formulation is that it is potentially very fast, allowing a direct coupling with cosmological hydrodynamic simulations. In particular, if a rapid method for calculating the Eddington tensors can be found, the scheme should be able to easily deal with an arbitrary number of sources. Also, the radiation intensity field does not suffer from the Poisson shot noise inherent in Monte Carlo approaches. Together with the local nature of the diffusion problem, this makes this approach particularly attractive for trying to address the cosmological reionization problem with self-consistent simulations of galaxy formation, since it is likely that low-mass star-forming galaxies of high number density play an important role for the reionization process. We therefore adopt in this work the suggestion of Gnedin & Abel (2001) and work out an implementation of the OTVET scheme in SPH. As we shall see, this entails a number of numerical challenges in practice. We will describe our solutions for these problems, and carry out a number of tests to evaluate the accuracy of the resulting implementation.

The near complete lack of analytical results for non-trivial radiative transfer problems makes it actually hard to validate different numerical techniques and to compare their performance with each other. A very useful help in this respect is provided by the cosmological radiative transfer code comparison project, carried out by Iliev et al. (2006b). In their paper, they present a comparison of 11 independent cosmological radiative transfer codes when applied to a variety of different test problems. A number of our tests are based on this study, which hence allows a comparison with results of these other codes.

We start this chapter with a brief introduction to the radiative transfer equations in Section 2.2. We then describe in Section 2.3 the moment-based method that is the basis for our approximate treatment of the radiation transfer problem. In Section 2.4 we elaborate in detail the numerical implementation of this scheme in a smoothed particle hydrodynamics formalism. This is followed by a presentation of results for various test problems in Section 2.5. Finally, we conclude with a summary and an outlook in Section 2.6.

2.2. The equation of radiative transfer

Let us briefly derive the radiative transfer (RT) equation in comoving coordinates, which is also useful for introducing our notation. Let $f_\gamma(t, \mathbf{x}, \mathbf{p})$ be the photon distribution function for comoving coordinates $\mathbf{x}$ and comoving photon momentum

$$\mathbf{p} = a\frac{h\nu}{c}\hat{\mathbf{n}},\tag{2.1}$$

where $a \equiv a(t)$ is the cosmological scale factor, h is the Planck constant, ν is the frequency of the photons, and $\hat{\mathbf{n}}$ is the unit vector in the direction of photon propagation. Then the number of photons in some part of the Universe is

$$N_\gamma = \int \mathrm{d}\mathbf{x}\,\mathrm{d}\mathbf{p}\, f_\gamma(t, \mathbf{x}, \mathbf{p})\,.\tag{2.2}$$

We can further define the phase-space continuity equation for the distribution function $f_\gamma \equiv f_\gamma(t, \mathbf{x}, \mathbf{p})$ of photons as

$$\frac{\partial f_\gamma}{\partial t} + \frac{\partial}{\partial \mathbf{x}}(\dot{\mathbf{x}}f_\gamma) + \frac{\partial}{\partial \mathbf{p}}(\dot{\mathbf{p}}f_\gamma) = \left.\frac{\partial f_\gamma}{\partial t}\right|_{\mathrm{sources}} - \left.\frac{\partial f_\gamma}{\partial t}\right|_{\mathrm{sinks}}.\tag{2.3}$$

Here the source and sink terms on the right hand side of the equation represent photon emission and absorption processes, respectively. We define the specific radiation intensity I_ν as the energy of photons in a frequency bin $\Delta\nu$ that pass through an area ΔA and solid angle $\Delta\Omega$ for a time Δt. The specific intensity I_ν is then related to the photon distribution f_γ as follows

$$I_\nu = h\nu f_\gamma \frac{\mathrm{d}^3 x\, \mathrm{d}^3 p}{\mathrm{d}\nu\, \mathrm{d}\Omega\, \mathrm{d}A\, \mathrm{d}t} = \frac{h^4\nu^3}{c^2}f_\gamma\,.\tag{2.4}$$

Substituting into equation (2.3), rearranging and adding the proper absorption and emission terms, one obtains the following radiative transfer equation in comoving variables (Gnedin & Ostriker, 1997):

$$\frac{1}{c}\frac{\partial I_\nu}{\partial t} + \frac{\mathbf{n}}{a}\frac{\partial I_\nu}{\partial \mathbf{x}} - \frac{H}{c}\left(\nu\frac{\partial I_\nu}{\partial \nu} - 3I_\nu\right) = -\kappa_\nu I_\nu + j_\nu\,, \tag{2.5}$$

where $H \equiv \dot{a}/a$ is the Hubble expansion rate, κ_ν is the absorption coefficient and j_ν is the emission coefficient.

Unfortunately, this full radiative transfer (RT) equation is in practice very difficult to solve in full generality. In particular, the high dimensionality (comprised of 3 spatial variables, 2 directional angles, 1 frequency variable, and time) of this partial differential equation makes a direct discretization on a mesh highly problematic. We will hence apply in Section 2.3 simplifications to the RT equation that yield an approximation that can be more easily calculated in cosmological codes.

2.2.1. Basic physics of hydrogen photoionization

If we consider pure hydrogen gas, the rate equations describing photoionization and photo-heating processes become comparatively simple. For the most part we will restrict ourselves to this chemical composition in this work, but we note that an extension of our formalism to include other elements is readily possible. In fact, we have already implemented helium as well, but we omit an explicit discussion of it in the following for the sake of simplicity.

The photoionization rate $k_{\rm ion}$ of hydrogen ($H + h\nu \to H^+ + e^-$) is given by

$$k_{\rm ion} = \int d\Omega \int_{\nu_o}^\infty d\nu\, \frac{I_\nu \sigma_\nu}{h\nu}\,, \tag{2.6}$$

where $h\nu_o = 13.6\,\mathrm{eV}$ is the hydrogen ionization potential and σ_ν is the photoionization cross-section:

$$\sigma_\nu = \sigma_o \left(\frac{\nu}{\nu_o}\right)^4 \frac{\exp\{4 - [(4\tan^{-1}\epsilon)/\epsilon]\}}{1 - \exp(-2\pi/\epsilon)} \quad \text{for } \nu \geq \nu_o, \tag{2.7}$$

where $\sigma_o = 6.30 \times 10^{-18}\,\mathrm{cm}^2$ and $\epsilon = \sqrt{(\nu/\nu_o) - 1}$.

The corresponding photoheating rate of hydrogen is given by

$$\Gamma = n_{\rm HI} \int d\Omega \int_{\nu_o}^\infty d\nu\, \frac{I_\nu \sigma_\nu}{h\nu}(h\nu - h\nu_o), \tag{2.8}$$

where $n_{\rm HI}$ is the number density of neutral hydrogen. Furthermore, the change in the neutral gas density due to recombinations is given by

$$\frac{\partial n_{\rm HI}}{\partial t} = \alpha\, n_{\rm e} n_{\rm p}, \tag{2.9}$$

where α is the temperature-dependent recombination coefficient, $n_{\rm e}$ is the electron number density and $n_{\rm p} \equiv n_{\rm HII}$ is the proton number density, which is in turn equal to the ionized hydrogen number density (for a pure hydrogen gas).

The change of the density of the neutral gas due to ionizations is given by

$$\frac{\partial n_{\text{HI}}}{\partial t} = -c\,\sigma_o n_{\text{HI}} n_\gamma, \tag{2.10}$$

where c is the speed of light and n_γ is the number density of ionizing photons. Thus, the total change in the neutral gas density, due to ionizations or recombinations, is given by

$$\frac{\partial n_{\text{HI}}}{\partial t} = \alpha\,n_{\text{e}} n_{\text{HII}} - c\,\sigma_o n_{\text{HI}} n_\gamma. \tag{2.11}$$

For all our calculations described in this work we use the on-the-spot approximation (Osterbrock & Ferland, 2006), i.e. photons emitted due to recombinations to excited levels are re-absorbed immediately by neutral hydrogen atoms in the vicinity. This behavior is described by the so called case-B recombination coefficient α_{B}.

2.3. The variable Eddington tensor formalism

We now turn to a description of the moment-based approximation to the radiation transfer problem that we use in this study. The first three moments of the specific intensity, the mean intensity J_ν, the radiation flux vector F_ν^i, and the radiation pressure tensor P_ν^{ij}, are defined as follows:

$$J_\nu = \frac{1}{4\pi} \int d\Omega\, I_\nu, \tag{2.12}$$

$$F_\nu^i = \frac{1}{4\pi} \int d\Omega\, n^i I_\nu, \tag{2.13}$$

$$P_\nu^{ij} = \frac{1}{4\pi} \int d\Omega\, n^i n^j I_\nu, \tag{2.14}$$

where n is a direction vector and the indices i and j run through the three elements of the vector in Cartesian space. We can further define h^{ij}, the so-called Eddington tensor, based on $P_\nu^{ij} = J_\nu h^{ij}$.

We can for the moment ignore the frequency derivative in the RT equation if we can assume that the Universe does not expand significantly before a photon is absorbed. With this simplification, the first moments of the RT equation take the form:

$$\frac{1}{c}\frac{\partial J_\nu}{\partial t} + \frac{1}{a}\frac{\partial F_\nu^i}{\partial x^i} = -\hat{\kappa}_\nu J_\nu + j_\nu, \tag{2.15}$$

$$\frac{1}{c}\frac{\partial F_\nu^j}{\partial t} + \frac{1}{a}\frac{\partial J_\nu h^{ij}}{\partial x^i} = -\hat{\kappa}_\nu F_\nu^j, \tag{2.16}$$

where

$$\hat{\kappa}_\nu = \kappa_\nu + \frac{3H}{c}. \tag{2.17}$$

In the second moment equation (2.16), we can ignore the term of the order c^{-1} and solve for the flux

$$F_\nu^j = -\frac{1}{\hat{\kappa}_\nu}\frac{1}{a}\frac{\partial J_\nu h^{ij}}{\partial x^i}, \tag{2.18}$$

which we then insert back into equation (2.15). This leads to the following approximation to the RT equation:

$$\frac{\partial J_\nu}{\partial t} = \frac{c}{a^2}\frac{\partial}{\partial x_j}\left(\frac{1}{\hat{\kappa}_\nu}\frac{\partial J_\nu h^{ij}}{\partial x_i}\right) - c\hat{\kappa}_\nu J_\nu + cj_\nu. \tag{2.19}$$

This form of the RT equation is already much simpler than the fully general form of equation (2.5). In particular, each of the terms in equation (2.19) has a simple physical interpretation. The time evolution of the local mean radiation intensity is given by a transport term, described by the anisotropic diffusion term on the right hand side, a sink term describing absorptions, and an emission term that accounts for sources. However, in order to be able to solve this equation an expression for the Eddington tensor h^{ij} is needed, which is left undefined by these moment equations. We therefore need to assume a certain form for the Eddington tensor, or in other words, a *closure relation*.

For the closure relation, we follow Gnedin & Abel (2001) and estimate the local Eddington tensor with an optically thin approximation. This means that we assume that a reasonable approximation to the Eddington tensor can be obtained by approximating all lines-of-sight to the sources as being optically thin. The radiation intensity pressure tensor P^{ij} in this optically thin regime can then be computed as

$$P^{ij} \propto \int \mathrm{d}^3x'\rho_*(\mathbf{x}')\frac{(\mathbf{x}-\mathbf{x}')_i(\mathbf{x}-\mathbf{x}')_j}{(\mathbf{x}-\mathbf{x}')^4}, \tag{2.20}$$

and thus the Eddington tensor is given by

$$h^{ij} = \frac{P^{ij}}{\mathrm{Tr}(P)}. \tag{2.21}$$

Note that the Eddington tensor only determines in which *direction* the local radiation propagates, but the magnitude of the radiation intensity tensor is unimportant as far as the Eddington tensor is concerned. This means that even in situations where the lines-of-sight to the sources are not optically thin at all, one will often end up with fairly accurate estimates of the Eddington tensor based on equations (2.20) and (2.21), simply because the radiation will typically mainly propagate away from the sources, even in optically thick cases. In particular, note that the above approximation is always correct for a single source. When there are multiple sources of equal strength, the optically thin approximation will weight the sources that are closest most strongly, in accordance with the $1/r^2$ decay of the intensity. While this can be expected to result in reasonably accurate estimates of the Eddington tensor in many situations (especially in the vicinity of a dominating source), errors can certainly arise in particular situations, for example at locations that are

equidistant from two sources of equal strength. How serious these errors are in problems of interest needs to be analyzed with appropriate test problems.

As we describe later in more detail in Section 2.4.8, we note that equation (2.20) can be accurately calculated with a hierarchical multipole approach similar to the one applied in gravitational tree algorithms. This allows a fairly efficient treatment of an arbitrarily large number of sources, which is a distinctive advantage of the moments based approach compared with other methods.

2.3.1. Choice of convenient Lagrangian variables

We will now rewrite the RT equations into a form that is more convenient for use with a Lagrangian method such as SPH. In particular, it is advantageous to pick variables in the numerical scheme that are normalized to unit mass, not unit volume. For example, if we express the ionization state of the gas as the number density of ionized hydrogen per unit volume, then we have to readjust this number somehow any time we re-estimate the local gas density (which may change if the gas moves around), otherwise the ionized fraction would change. However, if we use convenient variables that are normalized to unit mass, we do not need to worry about such corrections.

For chemical networks of hydrogen, it is convenient (and often done in practice) to express abundances relative to the total abundance of hydrogen nuclei:

$$n_{\mathrm{H}} = \frac{X_{\mathrm{H}} \, \rho}{m_{\mathrm{p}}}. \tag{2.22}$$

Here $X_{\mathrm{H}} = 0.76$ is the cosmological mass fraction of hydrogen and m_{p} is the proton mass. In the following, we use the notation n_{HI} for neutral hydrogen, and n_{HII} for ionized hydrogen, such that

$$n_{\mathrm{H}} = n_{\mathrm{HI}} + n_{\mathrm{HII}}. \tag{2.23}$$

In our actual numerical code, we will use a variable $\tilde{n}_{\mathrm{HII}}$ to express the abundance of ionized hydrogen, defined as

$$\tilde{n}_{\mathrm{HII}} = \frac{n_{\mathrm{HII}}}{n_{\mathrm{H}}}, \tag{2.24}$$

where n_{HII} is the ordinary number density of HII atoms (i.e. number of protons per unit volume). Note that this quantity is now normalized to unit mass, as desired. In addition, it is dimensionless, which avoids numerical problems due to large numbers if we use astronomical length units.

A similar reasoning also applies to the radiation intensity itself. In principle, the fundamental quantity we work with is the frequency dependent, angle-averaged mean intensity. However, we cannot afford to carry around a full spectrum with each fluid element in a hydrodynamical code. This would be too cumbersome and also is not really necessary of we are interested only in the reionization problem. Instead, it is sufficient to store the intensity integrated over a narrow frequency interval around the ionization potential of hydrogen. Or in other words, a more convenient quantity to work with would be something

like the number density of photons capable of ionizing hydrogen. We now formulate the relevant equations using this concept.

In general, the photon number density is

$$n_\gamma = \frac{1}{c} \int \frac{4\pi J_\nu}{h\nu} \, d\nu. \tag{2.25}$$

However, we will only consider the spectrum in a small band around the frequencies of interest. For simplicity, we assume that the spectrum has the form

$$J_\nu = J_0 \, \delta(\nu - \nu_0) \tag{2.26}$$

around the ionization frequency ν_0, where $h\nu_0 = 13.6\,\text{eV}$ is the hydrogen ionization potential. This form of the radiation intensity limits the spectrum to effectively just the hydrogen ionization frequency. We therefore obtain this simple form

$$n_\gamma = \frac{1}{c} \frac{4\pi J_0}{h\nu_0} \tag{2.27}$$

for the number density of ionizing photons.

We also note that the absorption coefficient κ_ν for ionization in the equation for radiation transport is

$$\kappa_\nu = n_{\text{HI}} \, \sigma_\nu, \tag{2.28}$$

where σ_ν is the cross-section for hydrogen ionization. If we multiply the loss term $\kappa_\nu J_\nu$ in the RT equation by $4\pi/(c\,h\nu)$ and integrate over ν, we get the so-called ionization rate k_{ion}, given by

$$k_{\text{ion}} = \int \frac{4\pi J_\nu}{h\nu} \sigma_\nu d\nu. \tag{2.29}$$

For our narrow spectrum, this leads to the simple expression

$$\int d\nu \frac{4\pi}{ch\nu} \kappa_\nu J_\nu = \sigma_0 n_{\text{HI}} \, n_\gamma \,, \tag{2.30}$$

where σ_0 is the cross section at the resonance. Another consequence of these definitions is that we can write the number density evolution of ionized hydrogen due to new reionizations as

$$\frac{dn_{\text{HII}}}{dt} = c\,\sigma_0\, n_\gamma\, n_{\text{HI}}. \tag{2.31}$$

The photon field loses energy at the same rate, i.e. the loss term for the radiation field should be of the form

$$\frac{dn_\gamma}{dt} = -c\,\sigma_0\, n_\gamma\, n_{\text{HI}}, \tag{2.32}$$

which is also what the loss term in the RT equation gives in this notation.

The above suggests that we can cast the moment-based RT equation into a more convenient form if we multiply it through with $4\pi/(ch\nu)$ and integrate over ν. This gives:

$$\frac{\partial n_\gamma}{\partial t} = c\frac{\partial}{\partial x_j}\left(\frac{1}{\kappa}\frac{\partial n_\gamma h^{ij}}{\partial x_i}\right) - c\,\kappa\,n_\gamma + s_\gamma, \tag{2.33}$$

where $\kappa = \sigma_0 n_{\mathrm{HI}}$ and the cosmological scale factor has been dropped for simplicity. The source function s_γ gives the rate per unit volume at which new ionizing photons are produced. This is the formulation of the RT equation that we implemented in this work in the simulation code GADGET-3.

We have to augment equation (2.33) with the changes of the different chemical species as a result of interactions with the radiation field. If we consider only hydrogen, this is just:

$$\frac{\partial \tilde{n}_{\mathrm{HII}}}{\partial t} = c\,\sigma_0 \tilde{n}_{\mathrm{HI}} n_\gamma - \alpha\, n_{\mathrm{H}}\,\tilde{n}_e \tilde{n}_{\mathrm{HII}}\,, \tag{2.34}$$

where α is the temperature-dependent recombination coefficient. If we have only hydrogen, we can set $\tilde{n}_e = \tilde{n}_{\mathrm{HII}}$ and $\tilde{n}_{\mathrm{HI}} = 1 - \tilde{n}_{\mathrm{HII}}$.

For hydrogen reionization problems, we want to solve the two basic equations (2.33) and (2.34) as efficiently, accurately and robustly as possible. We recall that the three terms of (2.33) have a straightforward interpretation. The first term on the right hand side is a diffusion like equation, which is conservative, i.e. it leaves the total number of photons unchanged. The second term describes photon losses, and each photon lost will cause one hydrogen atom to be ionized. Finally, the third term is the source term, and describes the injection of new photons. This suggests that the total number of ionizations must always be equal to to the total number of photons lost. If we can maintain numerically accurate photon conservation, then this property should ensure a proper speed of the ionization front even for relatively inaccurate time stepping, as the propagation of the front should largely be determined by the injection rate of photons at the source.

The above suggests a simple possibility for treating the time evolution of the photon number density in each timestep in terms of three parts, corresponding to an *operator-splitting*, or *fractional-step* approach: One may first inject new photons according to the source function, then transport photons conservatively by treating the diffusion part, and finally, advance the "chemical network" (eqn. 2.34) by treating only ionizations and recombinations, making sure again that we do not lose any photons. The chemical equations can be easily "subcycled" or treated with an integrator for stiff differential equations, if needed, because they are completely local. On the other hand, the most expensive part of the time advance is given by the diffusion part. This not only involves a coupling with neighboring fluid elements but also cannot easily be integrated with an explicit time integration scheme, because the diffusion equation becomes easily unstable in this case. We will therefore treat this part with an implicit method. While involving an expensive iteration scheme, this provides good stability and allows for comparatively large timesteps.

2.4. Numerical Implementation

In this section we describe the numerical formalism we have implemented in order to solve the moment-based RT equations coupled to the parallel Tree/SPH code GADGET-3, which is a significantly evolved and extended version of the public GADGET-2 code (Springel, 2005). We first give a very brief overview of the basic concepts of smoothed particle hydro-

dynamics (SPH), and then present a derivation of a new anisotropic diffusion operator in SPH, which is needed for the radiation transfer in moment form when a spatially varying Eddington tensor is used. We also explain how the diffusion equation can be integrated robustly in time based on an implicit scheme with an iterative sparse matrix solver. The time integration of the rate equations for ionization and recombination also requires special methods because they involve stiff differential equations. Finally, we describe the calculation of the Eddington tensors, and how this can be best combined existing algorithms in the GADGET-3 code.

2.4.1. Smoothed Particle Hydrodynamics

SPH is a widely used Lagrangian scheme that follows the evolution of gas properties based on discrete tracer particles (see, e.g., Monaghan, 1992, for a review). The particle properties are averaged, 'smoothed', over a kernel function, yielding so-called kernel interpolants for the fluid properties based on a few sampling points. For example, the kernel-interpolant of a property $\langle Q \rangle$ is given by

$$\langle Q(\mathbf{r}) \rangle = \int d\mathbf{r}' Q(\mathbf{r}') W(|\mathbf{r}' - \mathbf{r}|, h), \tag{2.35}$$

where h is called the smoothing length and is defined such that the kernel W drops to zero for $|\mathbf{r}'| > h$. In a discretized form this equation becomes

$$\langle Q(\mathbf{r}_i) \rangle = \sum_j \frac{m_j}{\rho_j} Q(\mathbf{r}_j) W(|\mathbf{r}_j - \mathbf{r}_i|, h_i), \tag{2.36}$$

where the sum is over all the particles that lie inside radius h. In the GADGET code, the kernel has the following standard spline form:

$$W(r) = \frac{8}{\pi h^3} \begin{cases} 1 - 6\left(\frac{r}{h}\right)^2 + 6\left(\frac{r}{h}\right)^3 & \text{for } 0 \le \frac{r}{h} \le \frac{1}{2} \\ 2\left(1 - \frac{r}{h}\right)^3 & \text{for } \frac{1}{2} < \frac{r}{h} \le 1 \\ 0 & \text{for } 1 < \frac{r}{h}. \end{cases} \tag{2.37}$$

An important property of the kernel interpolant is that it can also be used to obtain a derivative of the reconstructed function, which can be simply approximated by

$$\nabla_i Q(\mathbf{r}_i) = \nabla_i \sum_j \frac{m_j}{\rho_j} Q(\mathbf{r}_j) W(|\mathbf{r}_j - \mathbf{r}_i|, h_i) = \sum_j \frac{m_j}{\rho_j} Q(\mathbf{r}_j) \nabla_i W(|\mathbf{r}_j - \mathbf{r}_i|, h_i). \tag{2.38}$$

Starting from a density estimate in the form

$$\rho_i = \sum_j m_j W(|\mathbf{r}_j - \mathbf{r}_i|, h_i), \tag{2.39}$$

this allows one to calculate pressure gradients, and from this, equations of motion for the gas elements which represent the Euler equations. The particular formulation for the

equation of motion we use here is based on the 'entropy-formulation' of SPH discussed by Springel & Hernquist (2002). The entropy is generated only by the artificial viscosity of shocks and by external sources of heat as follows

$$\frac{\mathrm{d}A_i}{\mathrm{d}t} = -\frac{\gamma - 1}{\rho_i^{\gamma-1}}\mathcal{L}(\rho_i, u_i) + \frac{\mathrm{d}A_i}{\mathrm{d}t}\bigg|_{\mathrm{visc}}. \tag{2.40}$$

Here $\mathcal{L}(\rho_i, u_i)$ denotes any sources or sinks due to radiative cooling or photoheating.

2.4.2. Obtaining anisotropic second order derivatives with a kernel interpolant

Discretization of the diffusion term in the RT transfer equation in SPH poses some difficulties. We are basically confronted with the task to find an efficient and accurate approximation to terms of the form

$$\frac{\partial^2 Q_{\alpha\beta}}{\partial x_s \partial x_k}, \tag{2.41}$$

where $Q_{\alpha\beta}$ is the product of the local Eddington tensor $\mathbf{h}$ and the photon density n_γ . Simply differentiating a kernel interpolant twice is not a good solution, as this becomes very noisy because the kernel-interpolant of SPH is only second-order accurate. On the other hand, the discretization of the Laplacian discussed by Jubelgas et al. (2004) does not work either, as it only works for the isotropic case.

We now describe the solution we have found for this problem, which basically consists of the task to approximate the second order partial derivatives of an element $Q_{\alpha\beta}(\mathbf{x})$ of the matrix $\mathbf{Q}(\mathbf{x})$ with a kernel-interpolant. We consider a Taylor-series for $Q_{\alpha\beta}(\mathbf{x}_j)$ in the proximity of $Q_{\alpha\beta}(\mathbf{x}_i)$, i.e.

$$Q_{\alpha\beta}(\mathbf{x}_j) - Q_{\alpha\beta}(\mathbf{x}_i) = \nabla Q_{\alpha\beta}\bigg|_{\mathbf{x}_i} \cdot (\mathbf{x}_j - \mathbf{x}_i) + \frac{1}{2}\sum_{s,k}\frac{\partial^2 Q_{\alpha\beta}}{\partial x_s \partial x_k}\bigg|_{\mathbf{x}_i}(\mathbf{x}_j - \mathbf{x}_i)_s(\mathbf{x}_j - \mathbf{x}_i)_k + \mathcal{O}(\mathbf{x}_j - \mathbf{x}_i)^3. \tag{2.42}$$

Let us use the short-hand notation $\mathbf{x}_{ij} = \mathbf{x}_j - \mathbf{x}_i$ and $W_{ij} = W(|\mathbf{x}_j - \mathbf{x}_i|)$, where $W(r)$ is the SPH smoothing kernel. Neglecting higher order terms, we multiply the above expansion with

$$\frac{(\mathbf{x}_{ij})_l \, W_{ij,m}}{|\mathbf{x}_{ij}|^2}, \tag{2.43}$$

and integrate over all $\mathbf{x}_j$. Here $(\mathbf{x}_{ij})_l$ is the l-th component of the vector $\mathbf{x}_{ij}$, and $W_{ij,m}$ is the partial derivative of W_{ij} with respect to the m-component of $\mathbf{x}_i$. In particular, this means we have

$$W_{ij,m} = (\nabla_i W_{ij})_m = -(\nabla_j W_{ij})_m = \frac{\partial W(|\mathbf{x}_{ij}|)}{\partial(\mathbf{x}_i)_m} = -W'(|\mathbf{x}_{ij}|)\frac{(\mathbf{x}_{ij})_m}{|\mathbf{x}_{ij}|}. \tag{2.44}$$

We now find that

$$\int \frac{(\mathbf{x}_{ij})_k \, (\mathbf{x}_{ij})_l \, W_{ij,m}}{|\mathbf{x}_{ij}|^2} \, \mathrm{d}\mathbf{x}_j = 0, \tag{2.45}$$

for all combinations of k, l and m. This is because there is always at least one single component of $\mathbf{x}_{ij}$ left so that the integral vanishes by symmetry. As a result, the first order term of our integrated Taylor expansion drops out.

We now consider the second order term, where we encounter the expression

$$T_{sklm} = \int \frac{(\mathbf{x}_{ij})_s \, (\mathbf{x}_{ij})_k \, (\mathbf{x}_{ij})_l \, (\mathbf{x}_{ij})_m \, W'(|\mathbf{x}_{ij}|)}{|\mathbf{x}_{ij}|^3} \, \mathrm{d}\mathbf{x}_j. \tag{2.46}$$

There are a number of different cases. If l and m are equal, then s and k must also be equal, otherwise the integral vanishes. So here we would have three possible contributions to a s, k-sum, corresponding to the three coordinates that s and k can assume. If l and m are unequal, then we must either have $s = l$ and $k = m$, or have $s = m$ and $k = s$. So here there are two contributions to a s, k-sum in this case. Evaluating the integral T_{sklm} for these cases gives:

$$T_{sklm} = \begin{cases} -\frac{3}{5} & \text{if } l = m \text{ and } s = k = l = m, \\[2mm] -\frac{1}{5} & \text{if } l = m \text{ and } s = k, \text{ but } s \neq l, \\[2mm] -\frac{1}{5} & \text{if } l \neq m, \text{ and } s = l, \, k = m \\ & \quad \text{or } s = m, \, k = l, \\[2mm] 0 & \text{in all other cases.} \end{cases} \tag{2.47}$$

Note that we can pick l and m freely when we multiply the Taylor expansion with the term (2.43) and integrate over it. In particular, we can also use several different choices one after the other and then form a linear combination of the results. This can in fact be used to isolate any of the second derivatives of the Hessian matrix of $Q_{\alpha\beta}$. Let us assume for example that we want to calculate the second derivative of $Q_{\alpha\beta}$ with respect to x_0. Choosing $l = m = 0$, then the three choices $k = s = 0$, $k = s = 1$ and $k = s = 2$ all give terms that contribute to the integral over the expansion. These are:

$$2 \int \frac{Q(\mathbf{x}_j) - Q(\mathbf{x}_i)}{|\mathbf{x}_{ij}|^2} (\mathbf{x}_{ij})_0 W_{ij,0} \, \mathrm{d}\mathbf{x}_j = \frac{3}{5} \frac{\partial^2 Q}{\partial x_0^2} + \frac{1}{5} \frac{\partial^2 Q}{\partial x_1^2} + \frac{1}{5} \frac{\partial^2 Q}{\partial x_2^2}. \tag{2.48}$$

Here Q is to be understood as $Q = Q_{\alpha\beta}$ for brevity. Based on this, we can now isolate the desired partial derivative by forming a linear combination:

$$\frac{\partial^2 Q}{\partial x_0^2} = 2 \int \frac{Q(\mathbf{x}_j) - Q(\mathbf{x}_i)}{|\mathbf{x}_{ij}|^2} \times \left[2(\mathbf{x}_{ij})_0 W_{ij,0} - \frac{1}{2}(\mathbf{x}_{ij})_1 W_{ij,1} - \frac{1}{2}(\mathbf{x}_{ij})_2 W_{ij,2} \right] \mathrm{d}\mathbf{x}_j. \tag{2.49}$$

In a similar fashion, we can obtain a mixed partial derivative in the following way:

$$\frac{\partial^2 Q}{\partial x_0 \partial x_1} = 2 \int \frac{Q(\mathbf{x}_j) - Q(\mathbf{x}_i)}{|\mathbf{x}_{ij}|^2} \times \left[\frac{5}{4}(\mathbf{x}_{ij})_0 W_{ij,1} + \frac{5}{4}(\mathbf{x}_{ij})_1 W_{ij,0} \right] \mathrm{d}\mathbf{x}_j. \tag{2.50}$$

Formulae for all other second-order partial derivatives can be obtained from these expressions by cyclic permutation. Also, they are valid for each of the matrix elements $Q_{\alpha\beta}$.

Using these results, we can now turn to obtaining an expression for the sum of the second derivatives, as needed in the anisotropic diffusion equation. Based on the above, we can write the desired expression in the compact form:

$$\left.\frac{\partial^2 Q_{\alpha\beta}}{\partial x_\alpha \partial x_\beta}\right|_{\mathbf{x}_i} = 2 \int \frac{\mathbf{x}_{ij}^{\mathrm{T}} \left[\tilde{\mathbf{Q}}(\mathbf{x}_j) - \tilde{\mathbf{Q}}(\mathbf{x}_i)\right] \nabla_i W_{ij}}{|\mathbf{x}_{ij}|^2} \, \mathrm{d}\mathbf{x}_j. \tag{2.51}$$

Here we defined a new matrix $\tilde{\mathbf{Q}}$ through the matrix elements of the original matrix $\mathbf{Q} = (Q_{\alpha\beta})$, in the following way:

$$\tilde{\mathbf{Q}} = \frac{5}{2}\mathbf{Q} - \frac{1}{2}\mathrm{Tr}(\mathbf{Q})\mathbf{I}. \tag{2.52}$$

Inspection of this result highlights one interesting issue that could potentially become a numerical stability problem in certain situations. The matrix $\tilde{\mathbf{Q}}$ is not guaranteed to correspond to a positive definite quadratic form when it is used in the SPH discretization form of equation (2.51). If the radiation transfer is very anisotropic, the matrix $\tilde{\mathbf{Q}}$ can contain negative diagonal elements and thus gives rise to an 'anti-diffusive' behavior in the discretized radiation transfer equation, where radiation is transported from a particle of lower radiation intensity to one with higher radiation intensity. It is not clear right away whether this will lead to numerical stability problems of the radiative diffusion treatment, but it could.

In case this is a problem, one way to avoid it would be to somehow suppress transport of radiation opposite to the direction of the gradient of the radiation intensity between a particle pair. Another way is to add in an isotropic component to $\tilde{\mathbf{Q}}$ such that

$$\tilde{\mathbf{Q}}^* = \alpha\tilde{\mathbf{Q}} + (1 - \alpha)\frac{\mathbf{I}}{3}. \tag{2.53}$$

Here the idea is to make $\tilde{\mathbf{Q}}^*$ slightly more isotropic, such that $\tilde{\mathbf{Q}}^*$ becomes positive definite again. In order to guarantee this, we need to assign $\alpha = \frac{2}{5}$. Form equations (2.52) and (2.53) we can see that this 'anisotropy-limited' matrix is then actually $\tilde{\mathbf{Q}}^* = \mathbf{Q}$. One interpretation of this result is that the unmodified matrix $\mathbf{Q}$ mediates diffusion which is a mix of 2/5 of the 'correct' anisotropic diffusion and 3/5 of isotropic diffusion. In some of our tests we will compare results from both formulations of the matrix. We will refer to $\tilde{\mathbf{Q}}^*$ as the 'anisotropy-limited' tensor and to $\tilde{\mathbf{Q}}$ as the 'fully-anisotropic' tensor.

Note that in the case where $\mathbf{Q}$ is diagonal and proportional to the identity matrix, equation (2.51) reduces to the isotropic result for a scalar function derived by Jubelgas et al. (2004) for the thermal conduction problem. The important point about equation (2.51) is that it involves only a first order derivative of the kernel function. As a result, it can be discretized straightforwardly in the usual SPH way, where the integration is replaced by a sum over all neighboring SPH particles within the kernel volume.

2.4.3. Discretization of the anisotropic diffusion term in SPH

As we have shown in detail in the previous section, kernel-interpolated second-order derivatives of some tensor $Q_{\alpha\beta}$ can be obtained as in equation (2.51) for a suitably defined modified tensor $\tilde{Q}$. Furthermore, we note the identity

$$\frac{\partial}{\partial x}\left(\frac{1}{s}\frac{Q}{\partial y}\right) = \frac{1}{2}\left(\frac{\partial^2}{\partial x \partial y}\frac{Q}{s} - Q\frac{\partial^2}{\partial x \partial y}\frac{1}{s} + \frac{1}{s}\frac{\partial^2 Q}{\partial x \partial y}\right) \tag{2.54}$$

and thus inserting equation (2.51) we obtain

$$\frac{\partial}{\partial x_\alpha}\left(\frac{1}{s}\frac{Q_{\alpha\beta}}{\partial x_\beta}\right) = 2\int \frac{\mathbf{x}_{ij}^{\mathrm{T}}\frac{1}{2}\left(\frac{1}{s_i}+\frac{1}{s_j}\right)[\tilde{\mathbf{Q}}(\mathbf{x}_j) - \tilde{\mathbf{Q}}(\mathbf{x}_i)]\,\nabla_i W_{ij}}{|\mathbf{x}_{ij}|^2}\,\mathrm{d}\mathbf{x}_j\,. \tag{2.55}$$

For our application, let us denote the correspondingly modified Eddington tensor as $\tilde{h}^{ij}$. We can then write down an SPH discretization of the diffusion part of the radiation transfer equation. This can be expressed as:

$$\frac{\partial n_\gamma^i}{\partial t} = 2\sum_j \frac{c}{\kappa_{ij}}\frac{\mathbf{x}_{ij}^{\mathrm{T}}\left[n_\gamma^j\tilde{\mathbf{h}}_j - n_\gamma^i\tilde{\mathbf{h}}_i\right]\,\nabla_i W_{ij}}{\mathbf{x}_{ij}^2}\frac{m_j}{\rho_{ij}}\,. \tag{2.56}$$

Here

$$\frac{1}{\kappa_{ij}} = \frac{1}{2}\left[\frac{1}{\kappa_i} + \frac{1}{\kappa_j}\right] \tag{2.57}$$

is a symmetric average of the absorption coefficients of the two particles i and j, and ρ_{ij} is a symmetrized density. It is however important to be careful about how exactly the symmetrizations are done in practice, because this can affect the performance of the scheme if there are particles of varying mass. In particular, we would like to use a formulation where the conservation of the number of photons is guaranteed in this case as well. If possible, we would also like to obtain a formulation where the effective coupling matrix is symmetric, because this is a prerequisite for using certain, particularly efficient solution methods from linear algebra, such as the conjugate gradient (CG) method.

The photon conservation property is best analyzed by switching to variables that directly encode the photon number of each particle. Let us define for this purpose the quantity

$$N_i = m_i n_\gamma^i \tag{2.58}$$

for each particle. The real photon number of a particle is actually $N_\gamma = n_\gamma * \rho/m$. Multiplying Eqn. (2.56) through with m_i gives now

$$\frac{\partial N_i}{\partial t} = 2\sum_j \frac{c}{\kappa_{ij}\rho_{ij}}\frac{\mathbf{x}_{ij}^{\mathrm{T}}\left[m_i N_j\tilde{\mathbf{h}}_j - m_j N_i\tilde{\mathbf{h}}_i\right]\,\nabla_i W_{ij}}{\mathbf{x}_{ij}^2}\,. \tag{2.59}$$

Note that we can also write this as

$$\frac{\partial N_i}{\partial t} = \sum_j (w_{ij}N_j - w_{ji}N_i), \tag{2.60}$$

where

$$w_{ij} \equiv \frac{c}{\kappa_{ij}\rho_{ij}} \frac{\mathbf{x}_{ij}^{\mathrm{T}} m_i \tilde{\mathbf{h}}_j \nabla_i W_{ij}}{\mathbf{x}_{ij}^2}. \tag{2.61}$$

From the formulation in equation (2.60) we easily see that the total photon number, $\sum_i N_i$, is conserved, but in general the matrix w_{ij} is not symmetric. Even though other linear solvers may work, this would prevent us from safely applying the CG scheme to calculate a solution for an backwards-Euler timestep of equation (2.60), as the required implicit solution involves the inversion of a matrix that linearly depends on w_{ij} (see below).

To fix this problem, we also symmetrize the mass-weighted Eddington tensor in (2.60), which results in the following final form of the anisotropic diffusion equation that we use for our numerical implementation:

$$\frac{\partial N_i}{\partial t} = \sum_j w_{ij}(N_j - N_i), \tag{2.62}$$

where w_{ij} is now redefined in a symmetric form:

$$w_{ij} \equiv \frac{2\,c\,m_{ij}}{\kappa_{ij}\rho_{ij}} \frac{\mathbf{x}_{ij}^{\mathrm{T}} \tilde{\mathbf{h}}_{ij} \nabla_i W_{ij}}{\mathbf{x}_{ij}^2}. \tag{2.63}$$

We may also include the sink term, which yields

$$\frac{\partial N_i}{\partial t} = \sum_j w_{ij}(N_j - N_i) - c\hat{\kappa}_i N_i. \tag{2.64}$$

This equation is still symmetric and can thus also be treated with the CG method, as we explain in more detail in the next subsection.

2.4.4. Time integration of the radiative transfer equation

As discussed earlier, we use an operator-split approach for the time integration of the radiation transfer equation, in which we effectively treat the time integration of the source term and that of the transport through anisotropic diffusion and the absorption through the sink terms as separate problems. In fact, we extend the operator-split idea also to the hydrodynamical evolution of the system, i.e. we alternate the timestepping of the diffusion equation with that of the Euler equations that describe the dynamical evolution of the gas. In the following, we first discuss the time integration of the diffusion and sink part, which is the most complicated part in our scheme.

It is well known that explicit time integration schemes of the diffusion equation becomes easily numerically unstable, unless a very small timestep is used. To ensure numerical stability, we therefore adopt an implicit method, namely the simple 'backwards Euler' scheme, which provides sufficient accuracy for the diffusion problem. To advance equation (2.64) for one timestep, we therefore want to solve the equation

$$N_i^{n+1} = N_i^n + \Delta t s_i m_i + \sum_j \Delta t\, w_{ij}(N_j^{n+1} - N_i^{n+1}) - \Delta t c \sigma_0 n_{\mathrm{HI}} N_i^{n+1}, \tag{2.65}$$

where N_i^{n+1} are the new photon numbers at the end of the timestep, and N_i^n are the ones at the beginning of step n. The last term in this equation encodes the photon loss term, which we also integrate implicitly. We note that the source term, on the other hand, can be simply advanced with an explicit Euler step.

The equations (2.65) are in fact a large, sparsely populated linear system of equations that can be written in the generic form

$$\mathbf{A}\mathbf{x} = \mathbf{b}, \tag{2.66}$$

where $\mathbf{A}$ is a coefficient matrix, $\mathbf{b}$ is a vector of known values and $\mathbf{x}$ is a vector of unknown values. For our application, the components of vector $\mathbf{b}$ are $b_i = N_i^n + \Delta t s_i m_i$, and the matrix elements are given by

$$A_{ij} = \delta_{ij}\left(1 + \sum_k \Delta t\, w_{ik} + \Delta t c \sigma_0 n_{\mathrm{HI}}\right) - \Delta t\, w_{ij}\,, \tag{2.67}$$

where the indexes i and j run over all the SPH particles. The solution vector of the linear problem defines the new photon numbers at the end of the step, $x_i = N_i^{n+1}$.

There are many different approaches for solving linear systems of equations, but the huge size of the matrix $\mathbf{A}$ in our problem (which is equal to the particle number squared) makes many standard approaches that rely on storing the whole matrix $\mathbf{A}$ impractical. Fortunately, the matrix $\mathbf{A}$ is only sparsely populated because in each row only approximately $\sim N_{\mathrm{sph}}$ elements are non-zero, those that describe the coupling of a particle to its neighbors. Sparse systems of this type can often be solved well with iterative schemes. We use such an iterative scheme in our work, the conjugate gradient (CG) method.

The conjugate gradient approach applies successive corrections to a trial solution that is used as a starting point. With every iteration, the solution becomes better. Since the corrections added in each of the steps are all orthogonal to each other, the rate of convergence of this method is often quite high, this is why we think it is a promising iteration scheme for the problem at hand. For reference, a derivation of the well-known CG method is given in B.1. However, a prerequisite for the applicability of the conjugate gradient method is that the matrix $\mathbf{A}$ is positive definite and symmetric. The symmetry is evident from our formulation and the matrix is positive definite since $w_{ij} \geq 0$, and thus $\sum_{ij} x_i A_{ij} x_j \geq 0 \,\forall\, x_i$.

To find a solution for the new photon number field, we iterate with the CG scheme until the difference between two successive approximations to $\mathbf{x}$ has dropped to a small percentage of $|\mathbf{x}|$. Note that the expensive parts in the calculation of one iteration are the matrix-vector multiplications. For each particle, they reduce to sums over all of its SPH neighbors, which is equivalent to an ordinary SPH loop, similar in computational cost to, e.g., the SPH density estimation. Since in our parallel code some of the SPH neighbors of a particle can be stored on other processors, this step also involves communication.

In practice, we start the iteration with the current photon distribution for $\mathbf{x}$, which is usually a fairly good starting point, since the expected solution for the photon distribution does not differ significantly from the previous state, except in the vicinity of the sources. In

the absence of a radiation field we set the vector to zero. The closer the guessed values for the vector $\mathbf{x}$ are to the solution, the faster the algorithm converges. One could also start from a random photon distribution, which will not affect the solution, but will slow down the algorithm and is therefore not a desirable choice. The number of iterations required to reach convergence depends on the condition number of the matrix $\mathbf{A}$, where the condition number is defined as $\lambda_{\max}/\lambda_{\min}$, the ratio of the largest to the smallest eigenvalue of the matrix. A large condition number slows down the convergence rate of iterative solvers of linear systems of equations. However, the number of required iterations can be reduced by *preconditioning* the matrix $\mathbf{A}$. For this purpose we employ the simple Jacobi preconditioner. More specifically, we modify our matrix equation as follows,

$$\mathbf{C}^{-1}\mathbf{A}\mathbf{x} = \mathbf{C}^{-1}\mathbf{b}, \tag{2.68}$$

where the matrix $\mathbf{C}$ is the Jacobi preconditioning matrix. It is defined as

$$C_{ij} = A_{ii}\delta_{ij}, \tag{2.69}$$

and has the rather simple inverse form

$$C_{ij}^{-1} = \frac{\delta_{ij}}{A_{ii}}. \tag{2.70}$$

Applying the Jacobi preconditioner to the matrix $\mathbf{A}$ basically means to divide the matrix $\mathbf{A}$ by its diagonal, which is simple to implement and to parallelize. While the associated reduction of the condition number improves the convergence speed, it would be desirable to find still better preconditioners that are more effective in this respect.

2.4.5. Time integration of the chemical network

The abundances of hydrogen and helium species are updated by accounting for the processes of photoionization, collisional ionization and recombination:

$$\frac{\partial \tilde{n}_{\mathrm{HII}}}{\partial t} = \gamma_{\mathrm{HI}}\tilde{n}_{\mathrm{HI}}\tilde{n}_e n_{\mathrm{H}} + c\sigma_0 \tilde{n}_{\mathrm{HI}}\tilde{n}_\gamma n_{\mathrm{H}} - \alpha_{\mathrm{HII}}\tilde{n}_e \tilde{n}_{\mathrm{HII}} n_{\mathrm{H}}, \tag{2.71}$$

$$\frac{\partial \tilde{n}_{\mathrm{HeII}}}{\partial t} = \gamma_{\mathrm{HeI}}\tilde{n}_{\mathrm{HeI}}\tilde{n}_e n_{\mathrm{H}} - \gamma_{\mathrm{HeII}}\tilde{n}_{\mathrm{HeII}}\tilde{n}_e n_{\mathrm{H}} + \alpha_{\mathrm{HeIII}}\tilde{n}_{\mathrm{HeIII}}\tilde{n}_e n_{\mathrm{H}}, \tag{2.72}$$

$$\frac{\partial \tilde{n}_{\mathrm{HeIII}}}{\partial t} = \gamma_{\mathrm{HeII}}\tilde{n}_{\mathrm{HeII}}\tilde{n}_e n_{\mathrm{H}} - \alpha_{\mathrm{HeIII}}\tilde{n}_{\mathrm{HeIII}}\tilde{n}_e n_{\mathrm{H}}, \tag{2.73}$$

where all abundances of hydrogen species ($\tilde{n}_{\mathrm{HI}}$, $\tilde{n}_{\mathrm{HII}}$) are expressed in dimensionless form relative to the total number density n_{H} of hydrogen, all helium abundances are fractions with respect to the helium number density, and the electron abundance is expressed as $\tilde{n}_e = n_e/n_{\mathrm{H}}$. Furthermore, γ denotes the collisional ionization coefficient, α is the recombination coefficient and $\sigma_0 = 6.3 \times 10^{-18}\,\mathrm{cm}^2$ is the photoionization cross-section for hydrogen at $13.6\,\mathrm{eV}$. These rate equations are solved using a semi-implicit scheme.
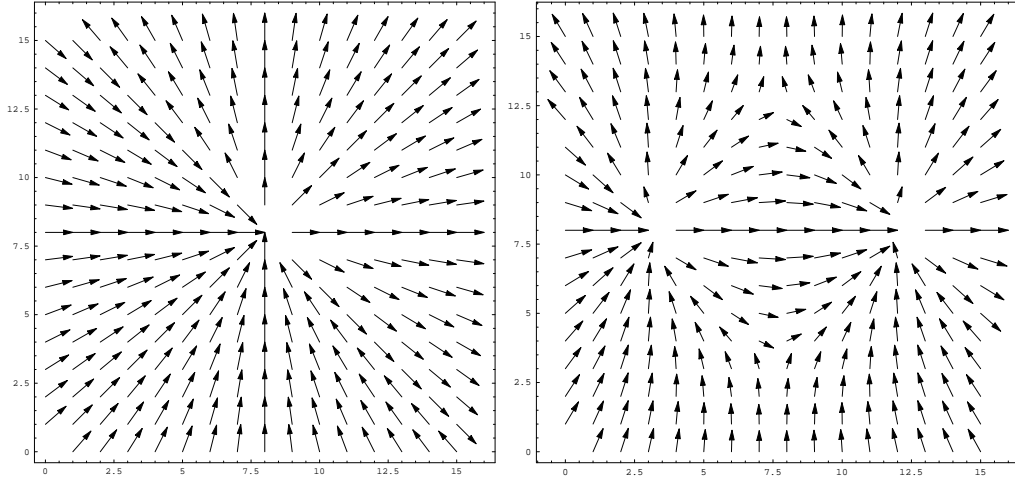
Figure 2.1: Eigenvectors of the Eddington tensor for a single source (left panel), and for two sources (right panel), calculated with our tree-code extensions of the GADGET-3 code. Both vector fields match the expectations. Note that the directions of the vectors can be turned 180º without affecting the direction of the transport of radiation, an effect due to the symmetric nature of the Eddington tensor.

2.4.6. Photoheating and cooling with a multi-frequency scheme

The photoheating of the gas by the ionizing part of the spectrum is described by the heating rate

$$\Gamma = n_{\text{HI}} \int_{\nu_0}^{\infty} \mathrm{d}\nu \frac{4\pi I_\nu}{h\nu} \sigma_\nu (h\nu - h\nu_0) \tag{2.74}$$

$$= n_{\text{HI}} \, c \, n_\gamma \, \tilde{\epsilon}_{\text{HI}} \, \tilde{\sigma}_{\text{HI}}, \tag{2.75}$$

where

$$\tilde{\sigma} = \int_{\nu_0}^{\infty} \mathrm{d}\nu \frac{4\pi I_\nu}{h\nu} \sigma_\nu \times \left(\int_{\nu_0}^{\infty} \mathrm{d}\nu \frac{4\pi I_\nu}{h\nu} \right)^{-1} \tag{2.76}$$

is a frequency averaged photoionization cross-section and

$$\tilde{\epsilon} = \int_{\nu_0}^{\infty} \mathrm{d}\nu \frac{4\pi I_\nu \sigma_\nu}{h\nu} (h\nu - h\nu_0) \times \left(\int_{\nu_0}^{\infty} \mathrm{d}\nu \frac{4\pi I_\nu \sigma_\nu}{h\nu} \right)^{-1} \tag{2.77}$$

is a frequency averaged photon excess energy (Spitzer, 1998). For our calculations, we usually assume a black body spectrum with $T_{\text{eff}} = 10^5 \, \text{K}$, which leads to $\tilde{\sigma}_{\text{HI}} = 1.63 \times 10^{-18} \, \text{cm}^2$ and $\tilde{\epsilon}_{\text{HI}} = 6.4 \, \text{eV}$.

In order to evolve the temperature of the gas correctly we consider cooling processes such as recombination cooling, collisional ionization cooling, collisional excitation cooling and Bremsstrahlung cooling. All rates have been adopted from Cen (1992) and are summarized in Appendix A. As a combination of heating and cooling terms the entropy of each particle is then evolved as in equation 2.40.

2.4.7. The source terms

As given in equation (2.33), the source term in the RT equation is s_γ in our formulation. This represents the number of photons emitted per unit time and per hydrogen atom. In our cosmological applications we usually want to represent this term by the stars that have formed in the simulation. To more accurately account for the short-lived massive stars, we can also use star-forming SPH particles as sources, converting their instantaneous star formation rates into an ionizing luminosity. Alternatively, we can also consider harder sources like Active Galactic Nuclei (AGN), if they are followed in the simulation. The time integration of the source function is unproblematic, and can be done with a simple explicit scheme on the dynamical timestep of the simulation. We only need to assign the source luminosities in a conservative fashion to the nearest SPH particles, provided they are not already gas particles anyway.

In some of our test problems considered in Section 2.5, the source term is prescribed as a certain number $\dot{N}_\gamma$ of ionizing photons per second, independent of the mass of the source. In this case we have

$$s_\gamma = \dot{N}_\gamma V = \dot{N}_\gamma \qquad (2.78)$$

where $V = m/\rho$ is a measure of the volume of the SPH particle with mass m that hosts the source. If we choose to distribute the source function to more than one particle, we use the 'scatter' approach. In this case the source function has the form

$$s_\gamma = \dot{N}_\gamma \sum_j \frac{m_j}{\rho_j} W(r)\, V, \qquad (2.79)$$

where the sum is over the SPH neighbors of the emitting particle.

2.4.8. Eddington tensor calculation

An important quantity in our formulation of the RT problem are the local Eddington tensors, which we estimate based on an optically thin approximation, as defined by equations (2.20) and (2.21). The $1/r^2$ dependence of the contribution of each source suggests a calculation method similar to that of gravity – via a hierarchical tree algorithm. To this end we extend the gravitational tree code in GADGET-3 with additional data structures. For each node of the tree, we also calculate the total luminosity and the luminosity-weighted center-of-mass. Depending on whether we consider the star particles as sources, the star-formation rate of gas particles, or also black hole particles, this can involve different types of particles.

The individual elements of the Eddington tensor are then computed by walking the tree in a way exactly analogous to the procedure for calculating gravitational forces. If a tree node appears under a small enough angle as seen from the point of interest, all its sources can be represented by the total luminosity of the node. Otherwise, the tree node is opened, and the daughter nodes are considered in turn. As a result, we obtain a multipole approximation to the local radiation pressure tensor, with a typical accuracy of $\sim 1\%$, provided a similar node-opening threshold value is used as for collisionless gravitational
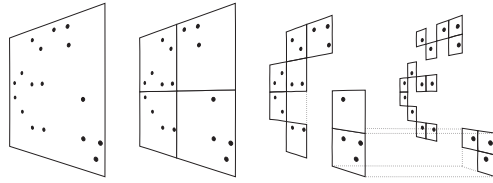
Figure 2.2: Schematic illustration of the Barnes and Hut oct-tree in two dimensions. The particles are first enclosed in a square (root node). This square is then iteratively subdivided in four squares of half the size, until exactly one particle is left in each final square (leaves of the tree). In the resulting tree structure, each square can be progenitor of up to four siblings. Note that empty squares need not to be stored Springel (2005)

dynamics. However, since for the Eddington tensor only the direction of the radiation pressure tensor ultimately matters, the final accuracy of the Eddington tensor is even better, and more than sufficient for our purposes. A very important property of this calculational method is that its overall speed is essentially independent of the number of sources that are present since the calculation is done simultaneously with the tree-walk that computes gravity, and involves only few additional floating point operations. This is quite different from the widely employed ray-tracing or Monte-Carlo schemes for radiation transfer, where the calculation cost may scale linearly with the number of sources.

As an example, Figure 2.1 shows the eigenvectors of the Eddington tensor for two different source configurations, calculated with our modified version of the GADGET-3 code. The left panel is for a single source. The vectors point radially outward or inward from the source, as expected. Note that the directions of the vectors can be turned by 180º without changing the radiation transport, because the tensor is symmetric. The panel on the right hand side shows the vector field around two sources, in the plane of the stars. The field is a dipole in this case and matches the expectations well.

2.4.9. Flux limited diffusion

If n_γ is the density of photons, then the maximum photon flux f that can occur is limited by the speed of light to $f = c\,n_\gamma$. This physical limit for the possible photon flux can in principle be violated under certain conditions when the diffusive approximation to the photon flux,

$$f^j = -\frac{1}{\hat{\kappa}_\nu}\frac{1}{a}\frac{\partial n_\gamma h^{ij}}{\partial x^i},\qquad(2.80)$$

is used. In treatments of radiative transfer in the isotropic diffusion approximation one therefore often invokes so-called flux limiters that are designed to enforce the condition

$$f \le cn_\gamma\qquad(2.81)$$

by damping the estimated flux when needed.
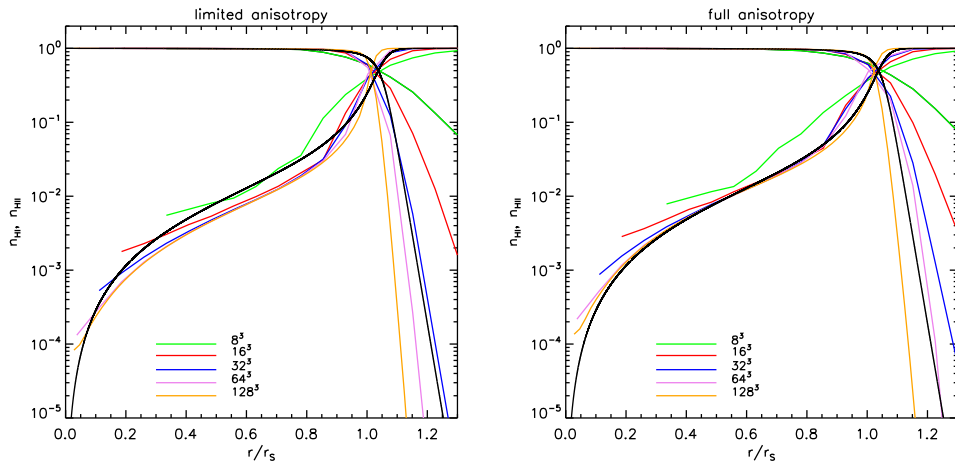
Figure 2.3: *Test (1)*. Resolution comparison of spherically averaged ionized and neutral fractions as a function of radial distance from the source, normalized by the Strömgren radius r_S. Results are shown for an anisotropy-limited (left panel) and fully anisotropic (right panel) Eddington tensor formulation at time $t = 500\,\mathrm{Myr} \sim 4t_\mathrm{rec}$. The compared resolutions are 8^3, 16^3, 32^3, 64^3 and 128^3 particles. The black lines show the analytical solution, integrated radially outward from the source as in equation (2.90). In both formulations the accuracy clearly increases with resolution and saturates when the highest number of particles is reached. In all cases, the final Strömgren radius agrees with the analytical predictions. The anisotropy-limited Eddington tensor formalism gives very accurate predictions for the ionized fraction in the regions outside the Strömgren radius ($r > r_\mathrm{S}$), but fails to give a correct value for the inner parts of the ionized regions. The fully anisotropic Eddington tensor formalism, however, predicts accurate values in both regions.

In our anisotropic diffusion treatment, we have also implemented an optional limiter that serves the same purpose. We observe the maximum flux constraint with the help of a parameter R, which is a function of the gradient of the photon density

$$R \equiv \frac{|\nabla n_\gamma|}{\kappa n_\gamma}. \tag{2.82}$$

We then define a flux limiter of the form

$$\lambda(R) = \frac{1 + 0.1R}{1 + 0.1R + 0.01R^2}, \tag{2.83}$$

where $\lambda(R) \to 0$ as $R \to \infty$. The detailed form of the analytic expression used for the flux limiter is arbitrary as long as it ensures a smooth transition between the two limiting states. We have chosen this form since it is widely used in other numerical RT codes, for example, a similar version is used by Whitehouse & Bate (2004). The flux limiter λ is then introduced into the diffusion part of equation (2.33) as follows:

$$\frac{\partial n_\gamma}{\partial t} = c \frac{\partial}{\partial x_j} \left(\frac{\lambda}{\kappa} \frac{\partial n_\gamma h^{ij}}{\partial x_i} \right) - c\,\kappa\,n_\gamma + s_\gamma. \tag{2.84}$$
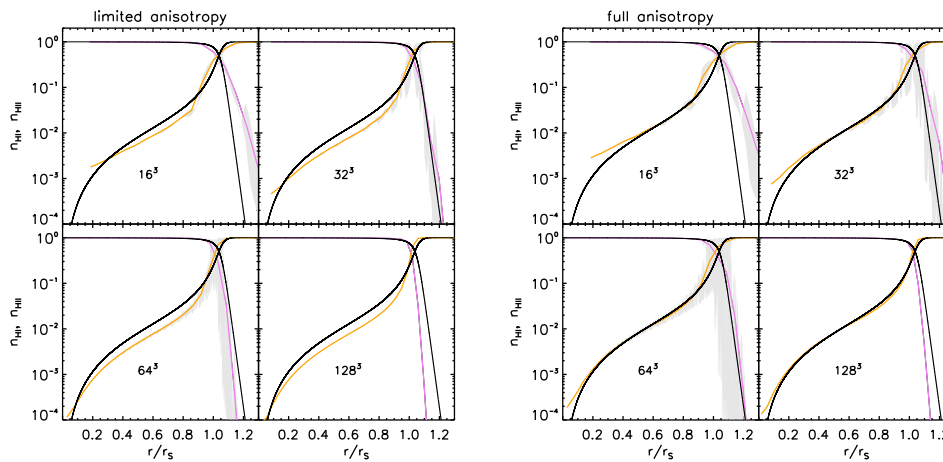
Figure 2.4: *Test (1)*. Resolution comparison of the scatter (gray areas) of the spherically averaged ionized and neutral fraction as function of radial distance from the source, normalized by the Strömgren radius r_S. Results are shown for an anisotropy-limited (left panel) and fully anisotropic (right panel) Eddington tensor formulation at time $t = 500\,\mathrm{Myr} \sim 4t_{\mathrm{rec}}$. The compared resolutions are 16^3, 32^3, 64^3 and 128^3 particles. The black lines show the analytical solution, integrated radially outward from the source as in equation (2.90). The orange lines show the spherically averaged neutral fraction and the violet lines the spherically averaged ionized fraction. The range of the scatter does not change significantly with resolution, since it is due to the intrinsic diffusive nature of SPH and the inaccuracies of the SPH density estimate. The highest resolution simulation has no scatter due to the high accuracy of the density estimates. The scatter in the fully anisotropic Eddington tensor formalism is larger due to the larger anisotropy in the diffusion terms of the RT equation.

However, we note that superluminal propagation of photons is usually not a problem in the ionization problems we are interested in. Here the speed of the ionization fronts is not limited by the speed of light, but rather by the luminosity of the sources and the density of the absorbing medium. Nevertheless, the flux limiter can also be usefully employed as a means to control the behavior of the ionization front (I-front) propagation in dense media. Due to the specific dependence of the R parameter, the photon propagation can effectively be limited in high-density regions, where the intensity gradient becomes very large.

2.4.10. Notes on the performance of the code

An important consideration in the development of RT codes is the calculational cost of the implemented scheme, as this determines whether the method is sufficiently fast to allow a coupling with hydrodynamic simulation codes. It is difficult to make general statements about the computational cost of our new RT scheme as this depends strongly on the particular physical problem that it is applied to. Arguably of most interest is a comparison of the speed of the method to other parts of the simulation code when applied to
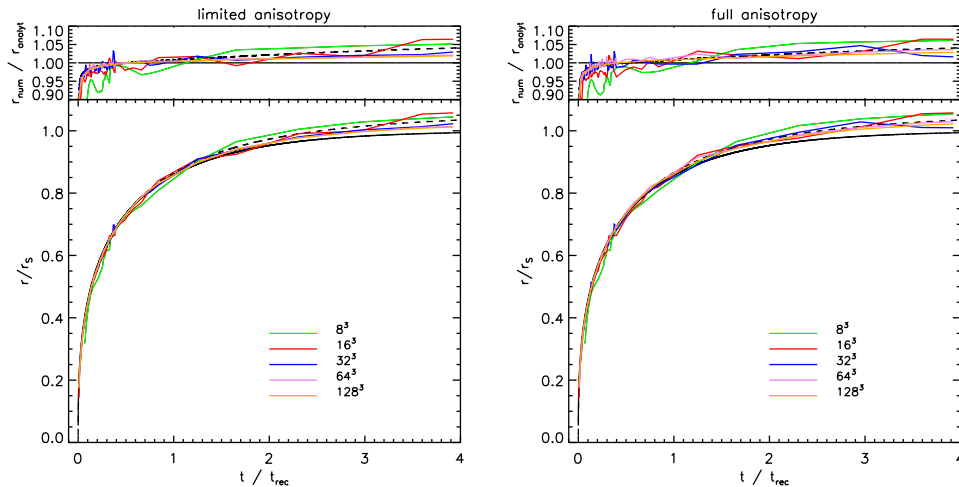
Figure 2.5: *Test (1)*. I-front expansion for an anisotropy-limited (left panel) and a fully anisotropic (right panel) Eddington tensor formulation with 16^3, 32^3, 64^3 and 128^3 particles. The dashed line is the exact solution obtained from equation (2.90) and the solid one as obtained from equation (2.86). Both results agree very well with the analytical predictions, but the fully anisotropic Eddington tensor formulation shows better results and smaller relative error for the I-front position.

the problem of cosmological structure formation with a self-consistent treatment of cosmic reionization. We here report approximate numbers for the speed of our new method in this situation, based on work in preparation that studies this problem.

First we note that in our implementation, when gravity is also integrated, the computation of the Eddington tensor incurs negligible costs, since it is done together with the gravity. Therefore, we find that in our implementation the increase of the computational cost with respect to the other relevant code modules (gravity, SPH density and SPH hydrodynamical forces) is primarily a function of the number of iterations required at each timestep to construct the implicit solution of the anisotropic diffusion equation. One iteration is approximately as costly as one SPH hydro computation, and the average number of iterations required ranges from typically 10 up to 200 in the most extreme cases. However, the RT equation is integrated only on a relatively coarse timestep, whereas the hydrodynamics is done also for many more smaller sub-steps. This reduces the effective cost of the whole RT calculation to several times the total cost of the hydrodynamics calculations. In practice, we measure a slow-down of the simulation code by a factor of order of 2 to 5 when the radiative transfer is included. While this is non-negligible, it does not seriously impact the ability to carry out large cosmological simulations. We also note that further optimizations in the radiative transfer algorithms, perhaps through an improved preconditioner, may reduce the cost of the RT calculation in the future.
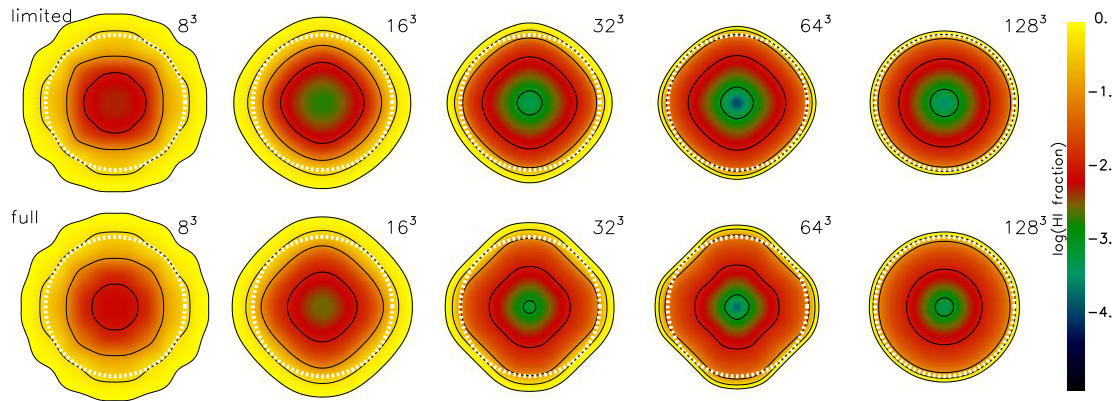
Figure 2.6: *Test (1)*. Slices of the neutral fraction through the ionized sphere at the position of the source. The upper row shows the results from the anisotropy-limited Eddington tensor formulation and the lower row from the fully anisotropic Eddington tensor formalism. Five different resolutions are compared: 8^3, 16^3, 32^3, 64^2 and 128^3 particles. The contours mark neutral fractions of $\tilde{n}_{\mathrm{HI}} = 0.9, 0.5, 0.1, 0.01$ and 0.001. The white circles give the radius of the Strömgren sphere. The geometrical distribution of the SPH particles affects the shape of the ionized sphere. The spheres are elongated in the x- and y-direction of the Cartesian grid, where the particle spacing is smaller and the SPH-kernel interpolant leads to slightly different couplings as in diagonal directions. This effect is stronger for the anisotropic Eddington tensor formulation.

2.5. Testing the code

In the following we present several basic tests for our new radiative transfer code. Where possible, we compare our results with analytical solutions or with results from other simulations (from the RT code comparison study by Iliev et al., 2006b). In section 2.5.1 we discuss our results for the classic test of the isothermal expansion of an ionized sphere in a homogeneous and static density field. In section 2.5.2 we study the effects of different timesteps on the accuracy of our simulations, while in section 2.5.3 we evolve two nearby sources with interacting ionized spheres. Then in section 2.5.4 we repeat the single ionized sphere expansion test, but this time allowing the temperature to evolve. In section 2.5.5 we present a shadowing test, where a dense clump is placed in the way of a plane-parallel I-front. Finally, in section 2.5.6 we evolve the radiation transport in a static cosmological density field.

2.5.1. Test (1) - Isothermal ionized sphere expansion

The expansion of an I-front in a static, homogeneous and isothermal gas is the only problem in radiation hydrodynamics that has a known analytical solution and is therefore the most widely used test for RT codes. A monochromatic source emits steadily $\dot{N}_\gamma$ photons with energy $h\nu = 13.6\,\mathrm{eV}$ per second into an initially neutral medium with constant gas density n_{H}. Then the Strömgren radius, at which the ionized sphere around the source has reached

its maximum radius, is defined as

$$r_{\mathrm{S}} = \left(\frac{3\dot{N}_\gamma}{4\pi\alpha_{\mathrm{B}}n_{\mathrm{H}}^2} \right)^{1/3}, \tag{2.85}$$

where α_{B} is the recombination coefficient. This radius is obtained by balancing the number of emitted photons by the number of photons lost due to recombinations along a given line of sight. If we assume that the I-front is infinitely thin, i.e. there is a discontinuity in the ionization fraction, then the expansion of the Strömgren radius can be solved analytically and the I-front radius r_{I} is given by

$$r_{\mathrm{I}} = r_{\mathrm{S}}[1 - \exp(-t/t_{\mathrm{rec}})]^{1/3}, \tag{2.86}$$

where

$$t_{\mathrm{rec}} = \frac{1}{n_{\mathrm{H}}\alpha_{\mathrm{B}}} \tag{2.87}$$

is the recombination time and α_{B} is the recombination coefficient.

The neutral and ionized fraction as a function of radius of the stable Strömgren sphere can be calculated analytically (e.g. Osterbrock & Ferland, 2006) from the equation

$$\frac{\tilde{n}_{\mathrm{HI}}(r)}{4\pi r^2} \int \mathrm{d}\nu \, \dot{N}_\gamma(\nu) \, e^{-\tau_\nu(r)} \, \sigma_\nu = \tilde{n}_{\mathrm{HII}}^2(r) \, n_{\mathrm{H}} \, \alpha_{\mathrm{B}}, \tag{2.88}$$

where $\tilde{n}_{\mathrm{HI}}$ is the neutral fraction, $\tilde{n}_{\mathrm{HII}}$ is the ionized fraction and

$$\tau_\nu(r) = n_{\mathrm{H}} \, \sigma_\nu \int_0^r \mathrm{d}r' \, \tilde{n}_{\mathrm{HI}}(r'). \tag{2.89}$$

Moreover, considering spherical symmetry and a point source we can solve analytically for the photon density radial profile $n_\gamma(r)$, yielding

$$n_\gamma(r) = \frac{1}{c} \frac{\dot{N}_\gamma}{4\pi r^2} \exp\left\{ -\int_0^r \kappa(r') \, \mathrm{d}r' \right\}. \tag{2.90}$$

From this we obtain ionized fraction profiles $\tilde{n}_{\mathrm{HII}}(r)$ for the whole evolution time.

The Strömgren radius obtained by direct integration of equation (2.88) differs from the one obtained from equation (2.85) because it does not approximate the ionized region as a sphere with constant, but with varying ionized fraction. We compare our results with both analytical solutions.

For definiteness, we follow the expansion of the ionized sphere around a source that emits $\dot{N}_\gamma = 5 \times 10^{48}$ photons s^{-1}. The surrounding hydrogen number density is $n_{\mathrm{H}} = 10^{-3}\,\mathrm{cm}^{-3}$ at a temperature of $T = 10^4\,\mathrm{K}$. At this temperature, the case B recombination coefficient is $\alpha_{\mathrm{B}} = 2.59 \times 10^{-13}\,\mathrm{cm}^3\,\mathrm{s}^{-1}$. Given these parameters, the recombination time is $t_{\mathrm{rec}} = 125.127\,\mathrm{Myr}$ and the expected Strömgren radius is $r_{\mathrm{S}} = 5.38\,\mathrm{kpc}$. We impose periodic boundary conditions in order to make sure that the density field is effectively infinite and

uniform. We note that this does not affect our RT calculation since the Eddington tensor is computed non-periodically.

We present results from the fully-anisotropic and the anisotropy-limited Eddington tensor formalism simulations by comparing first the final state of the ionized sphere and then the evolution of the I-front. Figure 2.3 shows the spherically averaged ionized and neutral fraction as a function of radial distance from the source, normalized by the Strömgren radius r_{S}, at time $t = 500\,\mathrm{Myr} \sim 4\,t_{\mathrm{rec}}$. In this case we compare the resolution effects on the accuracy of our numerical predictions by using simulations with 8^3, 16^3, 32^3, 64^3 and 128^3 particles, corresponding to mean spatial resolutions of 2.0 kpc, 1.0 kpc, 0.5 kpc and 0.25 kpc. In both formalisms the accuracy increases with resolution and the profiles converge for the higher resolutions. We also note that the anisotropy-limited Eddington tensor formalism gives very accurate predictions for the ionized fraction in the regions outside the Strömgren radius ($r > r_{\mathrm{S}}$), but fails to give correct values in the inner parts of the ionized sphere. The fully anisotropic Eddington tensor formalism, on the other hand, predicts the ionization state in both regions quite accurately.

We compare also the scatter of the ionized and neutral fraction profiles. Figure 2.4 shows the scatter (gray areas) of the spherically averaged ionized and neutral fraction profiles for four different resolutions (16^3, 32^3, 64^3 and 128^3 particles) at the end of the I-front expansion. All results agree well with the analytical radius of the Strömgren sphere. The range of the scatter does not change significantly with resolution, since it is due to the intrinsic diffusive nature of SPH and the inaccuracies of the SPH density estimate. This means that we obtain a density scatter of about 0.01% and thus introduce fluctuations in the gas density, which result in fluctuations in the hydrogen densities of the SPH particles and thus of the ionized and neutral fractions. The SPH density scatter in the 128^3 particle simulation is zero (thanks to the use of a Cartesian grid – but note that in real-world dynamical applications some density scatter is unavoidable) and thus there is no scatter in the ionized and neutral fractions. Moreover, the scatter in the fully anisotropic Eddington tensor formalism simulations is larger than in the other formalism simulations due to the larger retained anisotropy in the diffusion term of the RT equation.

The evolution of the I-front expansion is shown in Figure 2.5, comparing the two formalisms at different resolutions. The results from both formalisms agree very well with the analytical predictions and the accuracy increases with resolution. The fully anisotropic Eddington tensor formalism simulations show better results and smaller relative error for the I-front position. In both formalisms the error stays within 5% of the analytical solution and traces the analytical result obtained by direct integration of equation (2.90).

However, we note that the geometrical distribution of the SPH particles we used in our simulations introduces slight deviations from perfect sphericity into the shape of the ionized region. This reflects the Cartesian grid of particles used for these tests, an effect that can be clearly seen in the shapes of the ionized regions displayed in Figure 2.6. The spheres are elongated in the x- and y-directions of the Cartesian grid, where the particle spacing is smaller and the SPH-kernel interpolant weights the nearest neighbors slightly differently than in off-axis directions. This discreteness effect is stronger for the anisotropic Eddington tensor formulation.
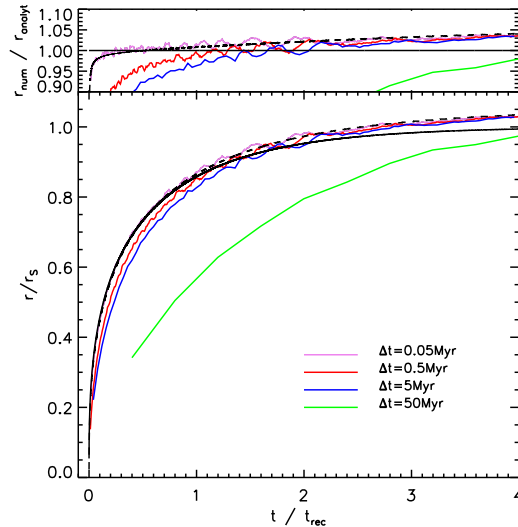
Figure 2.7: *Test (2)*. I-front expansion as a function of the recombination time. Results are shown for four different simulation timesteps: $\Delta t = 0.05, 0.5, 5 \text{ and } 50 \,\text{Myr}$. The dashed line is the exact solution obtained from equation (2.90) and the solid one is obtained from equation (2.86). The smallest timestep simulation agrees very well with the analytical solution. As the timestep increases, the results in the early phases of the expansion become more inaccurate. However, after about two recombination times, the I-front radius catches up with the analytical solution. The simulation with timestep $\Delta t = 50 \,\text{Myr}$ is very inaccurate, but in the end of the expansion the I-front radius is still within 5% of the analytical solution.

Considering all our results that compare the limited and fully anisotropic Eddington tensor formalisms, we use in all our further tests and simulations only the fully anisotropic formulation because it shows more accurate results. It turns out that this formulation is also robust, i.e. it does not show stability problems due to its 'anti-diffusive' terms when used in conjunction with an implicit solver, at least we have not experienced such problems in our test calculations.

2.5.2. Test (2) - Timestep comparison

In order to test the accuracy of our RT scheme we perform simulations of 64^3 particle resolution with different fixed timesteps: $\Delta t = 0.05, 0.5, 5 \text{ and } 50 \,\text{Myr}$. Applying the von Neumann stability criterion for an explicit integration of the diffusion part of our RT equation (2.19), we find a bound of the timestep equal to

$$\Delta t \leq \frac{1}{2} \frac{\kappa (\Delta x)^2}{c}, \tag{2.91}$$

where Δx is the mean spatial resolution, c is the speed of light and $\kappa = n_{\text{HI}} \sigma$ is the absorption coefficient. At the I-front the assumed neutral fraction is $\tilde{n}_{\text{HI}} = 0.5$ and thus
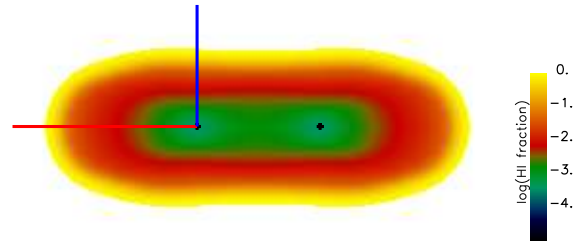
Figure 2.8: *Test (3)*. Ionized fraction in a plane of two equally luminous sources. The positions of the sources (8 kpc apart) are marked with black crosses. The snapshot is taken at time $t = 500$ Myr, when the expansion of the ionized regions has stopped, and the region where the Strömgren spheres overlap is approximately 3 kpc wide. There is a clear elongation along the axis connecting the two sources, as also described by Gnedin & Abel (2001). Figure 2.9 shows the evolution of the I-front along the aligned (red) and perpendicular (blue) directions with respect to the axis through the sources.

the absorption coefficient is $\kappa = 3.15 \times 10^{-21}$ cm^{-1}, resulting in an upper limit for the timestep $\Delta t \leq 10^{-3}$ Myr. However, this limit on the timestep is only a reference point for our results. Because we use an implicit scheme that is stable for all timestep sizes, we are fortunately not bound by this timestep limit and can in principle use much larger timesteps, subject only to the condition that the final accuracy reached is still acceptable.

We compare results for our simulations with the four different timestep sizes in Figure 2.7. The smallest timestep that we use is ten times as big as the analytical upper limit for an explicit scheme, yet its results agree perfectly with the analytical solution. For the other simulations the timestep sizes increase progressively by factors of 10, and the numerical results start to deviate from the analytical calculation. The changes are largest in the early phase of the I-front expansion. As the source "suddenly" switches on, very small time steps are needed in order to achieve good accuracy in the beginning, where the gradients in the photon density are very large. But later, after a couple of recombination times, the numerical results approach the analytical solution even for coarse timesteps and follow it until the expansion of the I-front ends. The $\Delta t = 50$ Myr simulation is initially very inaccurate, but note that its Strömgren radius is still within 5% of the analytical result. Therefore, our method manages to essentially produce correct Strömgren radii of the ionized spheres for all considered timesteps.

2.5.3. Test (3) - Two nearby sources

In our next test we follow the expansion of ionized regions around two nearby sources, where we expect to see inaccuracies due to the optically thin assumption used for estimating the Eddington tensors. Both sources emit $N_\gamma = 5 \times 10^{48}$ photons s^{-1} and are 8 kpc away from each other. The number density of the surrounding static and uniform hydrogen gas is $n_{\mathrm{H}} = 10^{-3}$ cm^{-3}, at a temperature of $T = 10^4$ K. From tests conducted by Gnedin & Abel (2001) we expect that the ionized regions are not spherical, but rather elongated along the
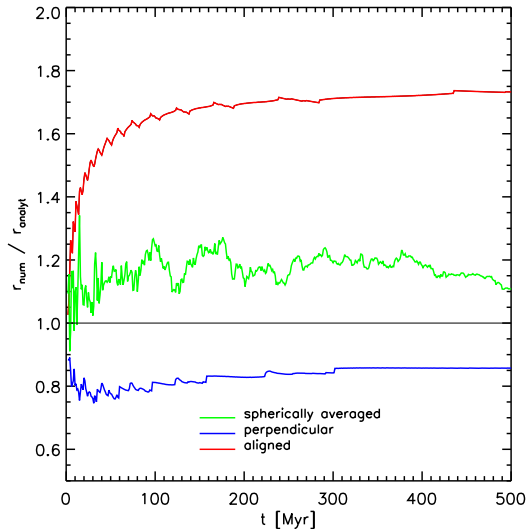
Figure 2.9: *Test (3)*. I-front expansion around a source in a double system, normalized by the analytical solution from equation (2.86), as a function of time. The red line is the I-front in the direction aligned with the two sources and the blue line is for the orthogonal direction. The green line shows the spherically averaged I-front position. As observed by Gnedin & Abel (2001), the ionized spheres are elongated along the axis of the two sources and compressed in the perpendicular direction. The spherically averaged I-front position is within 20% of the analytical expectation.

axis through the sources. This effect results from the calculation of the Eddington tensor, whose values along the symmetry axis are estimated high and boost the diffusion in this direction, while reducing it in the perpendicular direction.

In Figure 2.8, we show the neutral fraction for this test in a slice in the plane of the sources, taken at time $t = 500\,\mathrm{Myr}$ when the expansion of the regions has stopped. The expected elongated shape of the ionized regions is clearly visible. In Figure 2.9 we show the time evolution of three characteristic radii of the expanding ionized regions: one radius is measured in a direction aligned with the axis through the sources, one is measured perpendicular to it, and the third is a spherically averaged radius. We note that we do not expect the radii to match the analytical prediction from equation (2.86) exactly since the approximations there are valid only for a single ionized region expansion, but we here use the obtained value to compare the expansion of the ionized regions around two nearby sources. As expected, the aligned radius is always larger than the analytical result, while the perpendicular radius is smaller. However, the spherically averaged radius of the expanding region stays within 20% of the analytical value. We conclude that the optically thin approximation to estimate Eddington tensors can in certain situations introduce errors in the shapes of ionized bubbles, but these errors should be quite moderate or negligible in situations where the Eddington tensor is dominated by a bright nearby source, which is probably generic in many scenarios for cosmological reionization.
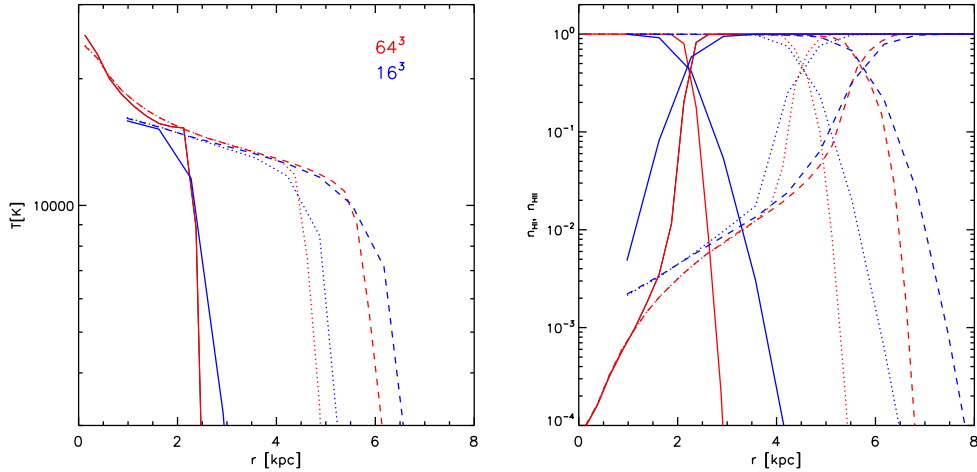
Figure 2.10: *Test (4)*. Time evolution of temperature (left panel) and ionized and neutral fraction (right panel) profiles of an expanding ionized sphere for two different resolutions: 16^3 (blue) and 64^3 (red) particles. Results at times $t = 10, 100$ and 500 Myr are shown in solid, dotted and dashed lines, respectively. The temperature profiles inside the ionized sphere converge for both resolutions at all times. The position of the I-front agrees well for both resolutions at all times.

2.5.4. Test (4) - Ionized sphere expansion with varying temperature

In this test we use the same setup as in section 2.5.1, but we initialize the gas temperature with $T_0 = 10^2$ K and let it evolve due to the coupling to the radiation field. We furthermore approximate the recombination coefficient α_B with

$$\alpha_B(T) = 2.59 \times 10^{-13} \left(\frac{T}{10^4 \, \mathrm{K}} \right)^{-0.7} \mathrm{cm}^3 \, \mathrm{s}^{-1}, \tag{2.92}$$

and assume a black body spectrum of temperature 10^5 K for the source, setting the parameters from equation (2.8) to $\tilde{\sigma} = 1.63 \times 10^{-18} \, \mathrm{cm}^2$ and $\tilde{\epsilon} = 29.65 \, \mathrm{eV}$. Then we evolve equation (2.40) for every particle, at every time step, considering photoheating, recombination cooling, collisional ionization cooling, collisional excitation cooling and Bremsstrahlung cooling. In this way we test a realistic expansion of an ionized sphere around a single source.

We test our scheme with two different resolutions: 16^3 and 64^4 particles. The time evolution of the temperature profile in both tests is shown in the left panel of Figure 2.10. The temperature close to the source rises to approximately 2×10^4 K and then drops down to 10^2 K outside the ionized region. From left to right, the profiles are shown at three different times: $t = 10, 100$, and 500 Myr. The results from the simulations converge inside the ionized sphere. Outside the ionized region the low resolution simulation produces, as expected, a smaller slope of the temperature drop further from the ionized sphere radius. In the right panel of Figure 2.10, we compare the neutral and ionized fractions at the same times. Both resolutions converge at the radius of the ionized sphere.
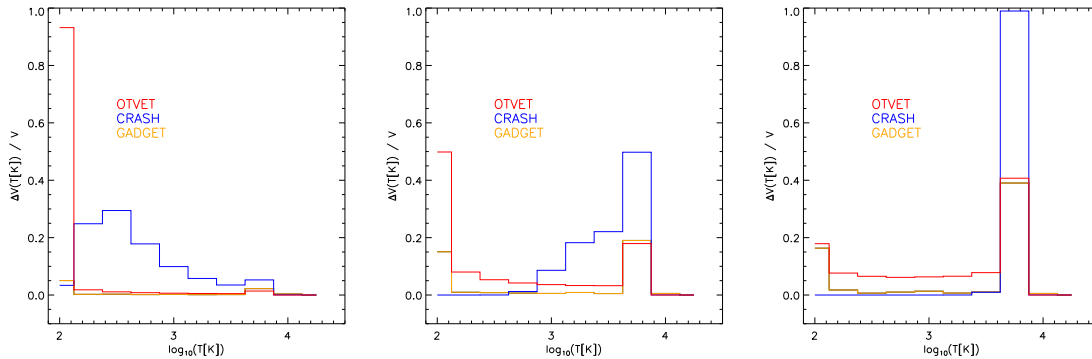
Figure 2.11: *Test (4)*. Volume fraction of the temperature for a comparison between CRASH, OTVET and GADGET at three different times $t = 10, 100 \text{ and } 500 \, \text{Myr}$ (left to right). The results of GADGET and OTVET are comparable, but CRASH has a harder spectral distribution and employs multiple frequency bins and thus gives slightly different results. Differences between GADGET and OTVET may also be due to different resolutions (OTVET has $0.05 \, \text{kpc}$, while for GADGET $\sim 0.25 \, \text{kpc}$).

In order to verify our results we compare them with results obtained with the codes CRASH (Maselli et al., 2003) and OTVET (Gnedin & Abel, 2001), as summarized by Iliev et al. (2006b) in the RT Code Comparison Project. In Figure 2.11, we show a comparison of the volume fraction of the temperature and in Figure 2.12 we present a comparison of the ionized volume fractions, at three different times: $t = 10, 100, \text{ and } 500 \, \text{Myr}$. The temperature volume fractions are all somewhat different due to the very different heating schemes employed. The results of GADGET and OTVET are comparable, but CRASH uses a harder spectral distribution and multiple frequency bins and thus gives different results. With increasing time GADGET produces a larger strongly ionized volume, and smaller intermediately ionized volume fraction than the other codes, which is also mirrored in the larger gradient of the ionized fraction that it produces. These differences are due to the different treatments of the source spectra that the codes employ, which are in general difficult to compare. Deviations might also be due to the different temperature structures of the ionized spheres and the different resolutions of the codes (OTVET and CRASH used $0.05 \, \text{kpc}$, GADGET only $\sim 0.25 \, \text{kpc}$).

2.5.5. Test (5) - Shadowing by a dense clump

As a further test problem, we consider the interaction of a plane-parallel front of ionizing photons with a uniform dense cylinder of neutral gas. The setup of our problem consists of a box with dimensions $(x, y, z) = (40 \, \text{kpc}, 10 \, \text{kpc}, 20 \, \text{kpc})$. One side of which (the xy-plane) is aligned with a plane of stars that produce the ionizing photons. A dense cylinder of gas is located 5 kpc from this sheet-like source and has a radius $r_C = 2.5$ kpc. The axis of the cylinder is oriented parallel to the z-axis of the box. The particle resolution is $(N_x, N_y, N_z) = (256, 64, 8)$. The hydrogen number density in the cylinder is 10^5 times
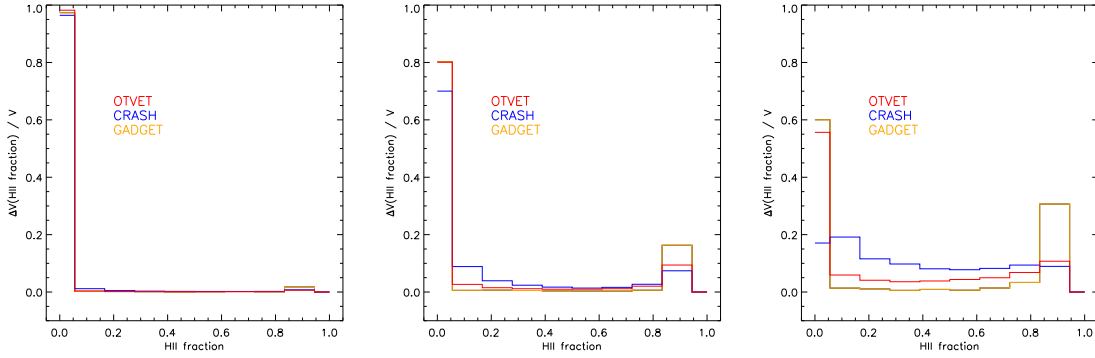
Figure 2.12: *Test (4).* Volume fraction of the ionized fraction in a comparison between CRASH, OTVET and GADGET for three different times $t = 10,\, 100$ and $500\,\mathrm{Myr}$ (left to right). With increasing time, GADGET produces larger strongly ionized volume and smaller intermediately ionized volume than the other codes, mirrored in the larger gradient of the ionized fraction that it produces. These deviations are likely due to different source spectra treatments, temperature structures of the ionized spheres, and different numerical resolutions.

the surrounding density of $n_{\mathrm{H}} = 10^{-3}\mathrm{cm}^{-3}$. There are 512 stars and each of them emits $\dot{N}_\gamma = 1.2 \times 10^{48}\,\mathrm{photons\,s^{-1}}$.

We first present results obtained with an Eddington tensor that mimics a plane-parallel I-front, of the form

$$\tilde{\mathbf{h}} = \left(\begin{array}{ccc} 1 & 0 & 0 \\ 0 & 0 & 0 \\ 0 & 0 & 0 \end{array} \right), \tag{2.93}$$

which represents photon transport only in the x-direction. We also consider two other cases where the Eddington tensor is calculated differently. In the first case we use the OTVET approximation, where the tensor is computed assuming all gas is optically thin. In the second case we account for the fact that the dense clump is optically thick by enforcing that no radiation is transported into the shadowed region. We achieve this by setting the Eddington tensor in the shadowed area to zero, such that the product $h^{ij}J_\nu$ vanishes. Note that for a vanishing radiation pressure tensor, the trace condition for the Eddington tensor needs not to be fulfilled. This second case is only meant to produce the expected solution with a sharp shadow.

Figure 2.13 shows the ionized fraction in a cut through the simulation volume, in the plane $z = z_{\mathrm{box}}/2$, at three different times: $t = 0.5,\, 1,$ and $2\,\mathrm{Myr}$. In the case of the OTVET approximation (first row), the dense cylinder fails to produce a sharp shadow. Instead, the radiation also diffuses around the obstacle, and is propagated eventually also in directions different from the x-direction, albeit more slowly. However, if we account for the fact that the dense clump is optically thick (second row), a clear and sharp shadow is produced, as expected. In Figure 2.14, we show the position of the I-front with respect to the center of the dense clump as a function of time. It is clear that the I-front moves faster in the case
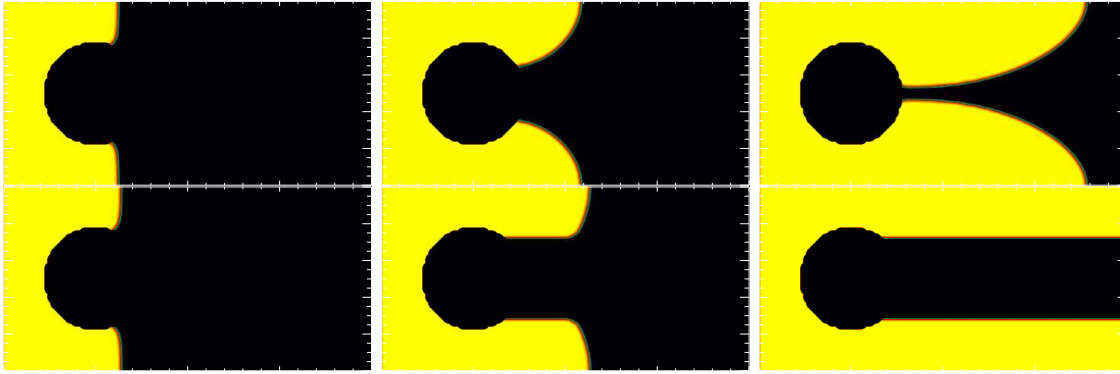
Figure 2.13: *Test (5).* Ionized fraction (yellow) in a slice through the middle of the simulation box. Time increases from left to right and the three different columns of snapshots are taken at $t = 0.5$, 1, and 2 Myr. In the upper row the Eddington tensor has been approximated with the OTVET scheme. In the second row the Eddington tensor has been set to zero in the shadowed region, given that the dense clump is optically thick, which should yield the correct result. The optically thin Eddington tensor approximation fails to produce a sharp shadow since radiation diffuses away from the plane-parallel front direction. In the optically thick approximation, however, a sharp shadow is obtained, implying that the failure of our method to produce a sharp shadow can also be blamed on using a non-vanishing Eddington tensor in the shadowed region.

where the Eddington tensor is approximated closer to the analytical case, i.e. it is zero in the shadow area.

The inability to create a sharp shadow is a limitation of the OTVET approximation implemented in SPH, as we have shown above. This limitation of codes using a moment method together with an OTVET approximation has already been noted by several groups, e.g. Gnedin & Abel (2001); Aubert & Teyssier (2008). It appears that despite our attempts to fully account for the anisotropic diffusion, the diffusion operator we have derived remains quite diffusive in SPH. This is simply a consequence of the non-vanishing coupling between particles with separation vectors not perfectly aligned with the direction of radiation propagation (here the x-axis). Unfortunately, this deficiency may also have other detrimental effects besides just slowing down the expansion of the I-front itself. We acknowledge that this can be an important limitation of our scheme for certain applications, especially when shielding is common and shadowing is important. Nevertheless, this limitation can influence the morphology of the reionization, but properties such as redshift and duration of the process, as well as temperature evolution of the gas and the radiation field, should still be accurate.

2.5.6. Test (6) - Static cosmological density field

In our final and most demanding test calculation we follow hydrogen ionization in a realistic cosmological density field, which is taken to be static for simplicity. In order to compare our results with those of the cosmological radiative transfer comparison project (Iliev et al.,
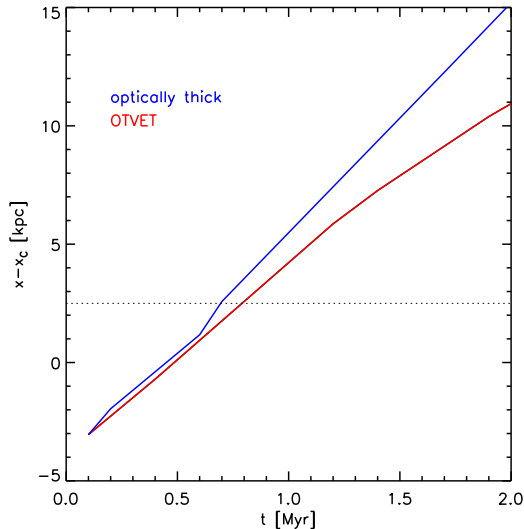
Figure 2.14: *Test (5).* Position of the I-front, relative to the center of the dense clump, as a function of time. The I-front moves faster in the case where the Eddington tensor is computed accounting for the optically thick clump (blue line). In the case where the OTVET scheme is used (red line), the I-front expands slower. The dashed line shows the position at the end of the clump, where the difference between the expansion rates begins to grow.

2006b) we use the same cosmological box parameters and assign sources in the same way. The box with size $0.5\,h^{-1}$comoving Mpc is evolved with a standard ΛCDM model with the following cosmological parameters: $\Omega_0 = 0.27$, $\Omega_{\mathrm{b}} = 0.043$, $h = 0.7$, until redshift $z = 9$. The density field at this point is considered for our further analysis.

The source distribution is determined by finding halos within the simulation box with a FOF algorithm and then assigning sources to the 16 most massive ones. The photon luminosity of the sources is

$$\dot{N}_\gamma = f_\gamma \frac{M\Omega_{\mathrm{b}}}{\Omega_0 m_{\mathrm{p}} t_{\mathrm{s}}}, \tag{2.94}$$

where M is the total halo mass, $t_{\mathrm{s}} = 3\,\mathrm{Myr}$ is the lifetime of the source, m_{p} is the proton mass and $f_\gamma = 250$ is the number of emitted photons per atom during the lifetime of the source. We find that the total source luminosity in our simulated box agrees well with the one from Iliev et al. (2006b). For simplicity we also set the initial temperature of the gas to 100 K throughout the whole box.

We found that simply mapping the grid cells onto a Cartesian mesh of SPH particles with different masses introduces large noise into our RT calculation, due to the large variations in the mass of neighboring particles. It is therefore not straightforward to translate the mesh-based data of the code comparison project into an equivalent SPH realization, and we therefore needed to created our own initial conditions. We note that simple methods to create an equal particle mass SPH realization from the given grid cells, e.g. through random sampling, tend to introduce large amounts of Poisson noise and wash out extrema
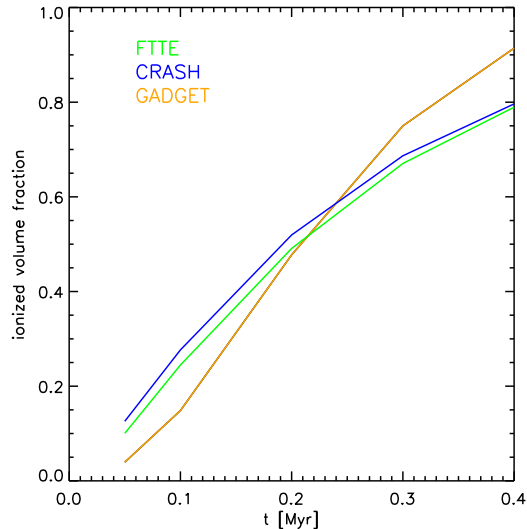
Figure 2.15: *Test (6)*. Time evolution of the volume-averaged ionized fraction in the whole simulation box. in comparison to CRASH (blue) and FTTE (green), GADGET (orange) produces lower ionized fractions at earlier times and higher ionized fractions at later times. The overall trend in the increase of the ionized fraction is the same, and the speed of ionization first accelerates and then decelerates. Differences between our results and the ones from the Comparison Project are in part also due to differences in the initial conditions, as we had to transform the grid-based density field to an SPH realization.

in the density field.

The evolution of the total volume-averaged ionized fraction in the box is very similar for GADGET and the Comparison Project codes, as shown in Figure 2.15. In the beginning of the simulation the total ionized fraction rises rapidly and then the increase decelerates. GADGET produces an overall lower ionized fraction until approximately $t = 0.2\,\mathrm{Myr}$ and higher one at later times. This mismatch is in part certainly caused by the morphological differences in the initial conditions that introduce different clumping properties of matter and therefore different I-front expansion histories. We recall that the true solution of the problem is unknown. Given the non-linearity of the system, the differences in detail of the initial conditions and cooling rates, and the fact that we compare fundamentally different RT schemes, the agreement that we obtain is actually very good.

To illustrate the spatial distribution of the ionized fraction and the temperature of the gas we show in Figure 2.16 slices through the simulation volume at $z = 0.7z_{\mathrm{box}}$ (through the largest group) at three different times $t = 0.05,\,0.2$ and $0.4\,\mathrm{Myr}$. The upper row shows contours of the neutral fraction plotted over a density field, the second row shows a map of the neutral fraction and the third row shows a map of the temperature of the gas. The dense regions trap the I-front and thus produce sharp gradients of the radiation density. In the under-dense regions ionization is more effective and the I-front is extended. Even though the ionized regions are mostly uniform, traces of the dense structures that are less

ionized can be seen near the front-trapping points. As shown in the contour maps, the I-fronts are broader in the low density regions and thinner in the high density regions. The temperature in the ionized regions reaches several 10^4 K and is uniform. It remains unchanged outside, where no photons are present.

We further compare the volume faction of the temperature and the ionized fraction from GADGET, CRASH and FTTE in Figures 2.17 and 2.18, at three different times $t = 0.05$, 0.2, and 0.4 Myr. The temperature volume fractions do not match particularly well due to the different photoheating mechanisms that GADGET, CRASH and FTTE use, but they find a similar maximum temperature. The volume fractions of the ionized fraction for GADGET, CRASH and FTTE have similar shapes. GADGET, in contrast to the other codes, produces less intermediately ionized gas. However, overall the histograms are in a reasonably good agreement with each other, suggesting that our moment-based scheme is quite capable in describing the reionization process and produces results of similar accuracy as other established radiative transfer codes.

2.6. Summary and Conclusions

We have presented a novel method for solving the radiative transfer equations within SPH, which is based on moments of the radiative transfer equation that are closed with a variable Eddington tensor. The radiation transport effectively becomes an anisotropic diffusion problem in this formulation. We have developed a new discretization scheme for anisotropic diffusion in SPH together with an implicit time integration method which for the first time allows a calculation of such anisotropic diffusion in SPH. Together with a scheme to estimate Eddington tensors based on the optically thin approximation, this yields a very fast approximate treatment of radiative transfer that can be used in dynamical SPH calculations.

We have implemented our method into the cosmological simulation code GADGET-3 and presented several test problems where we varied the initial conditions and different numerical parameters to investigate the accuracy of the method. Our test results agree in general very well with analytical predictions and data from other simulations, except that the long-term evolution of sharp geometric shadows is clearly not followed accurately. While this clearly limits the range of applicability of the method, we expect that the method can still provide reasonably accurate results for problems where shadowing is comparatively unimportant, such as cosmological reionization, where the SPH-based variable Eddington tensor approach can be competitive with other techniques. However, our method has two important strengths not shared by most other techniques: It can easily cope with an arbitrary number of sources since its speed is essentially independent of the number of sources, and furthermore, it is fast enough to be included into a cosmological simulation code where radiative transfer is calculated on-the-fly together with the ordinary dynamics. This is especially promising for future calculations of galaxy formation and reionization that we want to carry out with our new code.

All tests problems we have presented in this thesis agree well with theoretical predic-
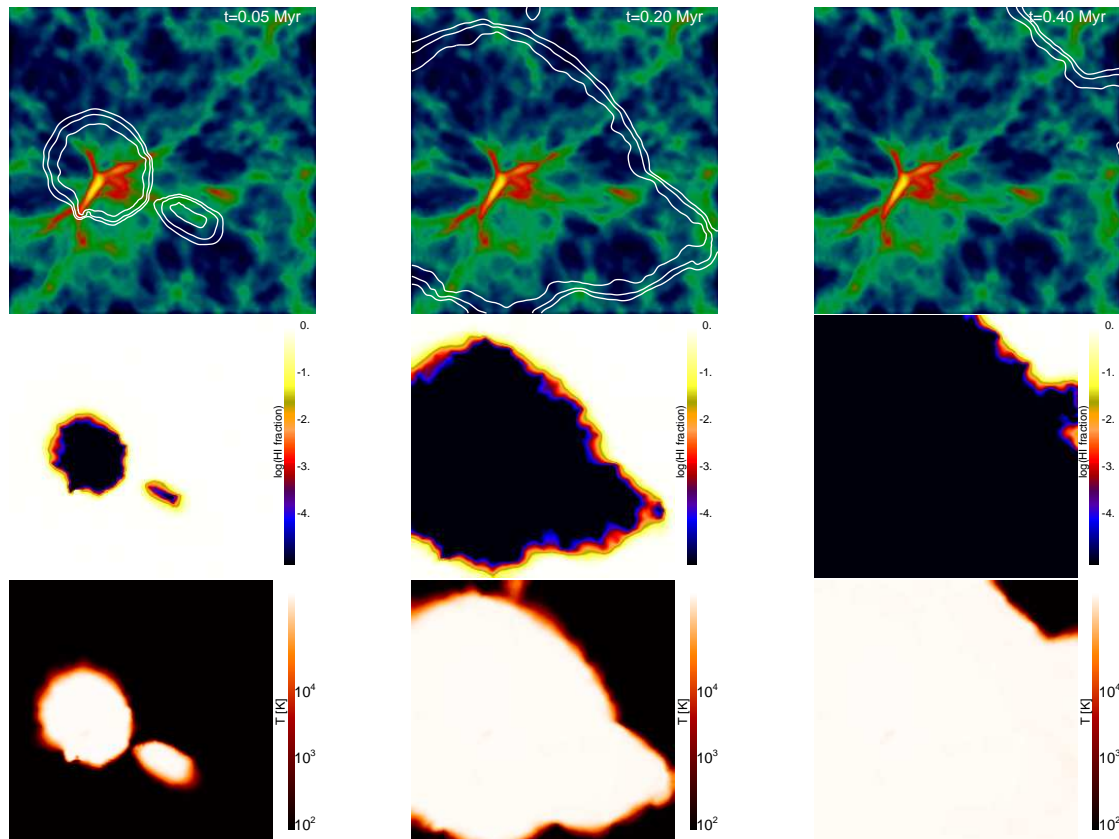
Figure 2.16: *Test (4).* The upper row shows contours of neutral fractions equal to $0.01, 0.5$ and 0.9 in a slice through the simulation volume at $z = 0.7z_{\text{box}}$, through the largest group. The snapshots are taken at times $t = 0.05$, 0.2 and $0.4\,\text{Myr}$ (left to right). The background shows a slice of the density distribution. The ionized regions expand with time as the I-front is trapped at high density regions and extends into low density regions. The second row shows the neutral fraction in the same slice. The ionized regions are uniform with some substructure visible near the front-trapping regions, where the I-front is not as diffuse as in low density regions. The third row shows the temperature distribution in the slice. The temperature in the ionized regions reaches several 10^4K and remains uniform outside these regions.
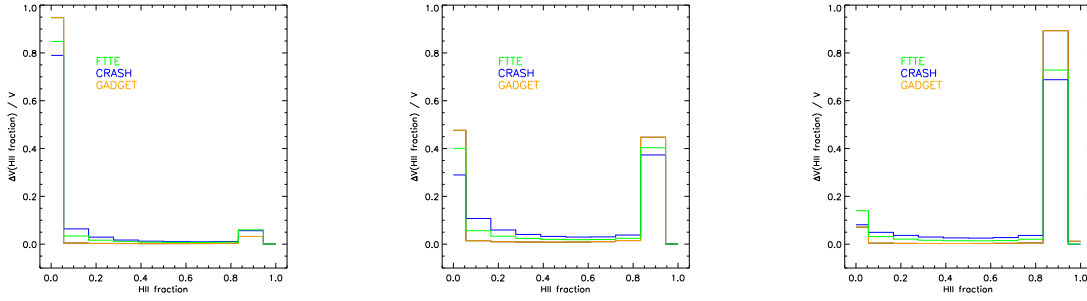
Figure 2.17: *Test (6).* Volume fraction of the ionized fraction at three different times $t = 0.05$, 0.2, and 0.4 Myr (left to right). Results from GADGET are compared with results from CRASH and FTTE from Iliev et al. (2006b). All codes match in the shape of the histograms, but GADGET gives a lower intermediately ionized fraction.
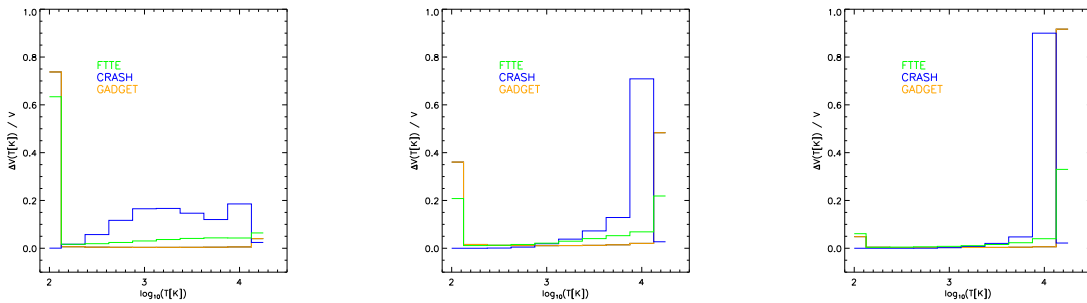
Figure 2.18: *Test (6).* Volume fraction of the temperature at three different times $t = 0.05$, 0.2 and 0.4 Myr (left to right). Results from GADGET are compared with results from CRASH and FTTE from Iliev et al. (2006b). All codes produce different histograms. FTTE and GADGET agree better with each other at later evolution times. CRASH produces higher temperatures due to its use of a different spectral distribution.

tions or results obtained with other radiative transfer codes. We should be able to obtain a realistic and accurate temperature evolution of the Universe during reionization, which is important for setting the 'cosmic equation of state' that regulates the absorption seen as Lyman-α forest in the spectra of distant quasars. Finally, we plan to include the photoionization of other elements besides hydrogen, most importantly of helium. Helium reionization probably happened sometime at redshift $z \sim 2 - 4$, where it may have left a sizable imprint in the temperature evolution of the intergalactic medium. Surprisingly, recent observations suggest that the temperature-density relation of the IGM may be inverted (Bolton et al., 2008b), which could be caused by radiative transfer effects related to helium reionization. Whether this is indeed possible can only be clarified with simulations. Studying this question with our new methods would therefore be particularly timely.

3

Simulations of galaxy formation with radiative transfer: Hydrogen reionization and radiative feedback

Based on Petkova, M., & Springel, V., 2010, MNRAS, p.1851

3.1. Introduction

We use the new radiative transfer algorithm we developed in the previous chapter to carry out high-resolution simulations of cosmic structure growth in the proper cosmological context. The approximation to radiative transfer employed, the optically-thin variable Eddington tensor approach (Gnedin & Abel, 2001), is fast enough to allow coupled radiative-hydrodynamic simulations of the galaxy formation process. At the same time, the employed moment-based approximation to the radiative transfer problem can be expected to be still reasonably accurate for the reionization problem. In particular, thanks to the photon-conserving character of our implementation of radiative transfer and of the chemical network, ionization fronts are bound to propagate with the right speed. The Lagrangian smoothed particle approach (SPH) we use automatically adapts to the large dynamic range in density developing in the galaxy formation problem. Combined with the fully adaptive gravitational force solver implemented in GADGET, this yields a numerical scheme that is particularly well suited for the cosmic structure formation problem.

For a first assessment of our new approach we study simulations of the standard ΛCDM cosmology and treat star formation and supernova feedback with the ISM sub-resolution model developed in Springel & Hernquist (2003a). For simplicity, we shall here only consider ordinary star-formation regions as sources of ionizing radiation. We are especially interested in whether the star formation predicted by the simulations results in a plausible reionization history of the Universe, and whether it at the same time yields a thermal and ionization state of the IGM at intermediate redshifts that is consistent with that probed by observations of the Lyman-α forest. Finally, we are interested in possible differences

induced in galaxy formation due to the spatially varying radiative feedback in the radiative transfer simulations, especially in comparison with the much simpler and so far widely adopted treatment where a spatially homogeneous UV background is externally imposed.

This chapter is structured as follows. We start in Section 3.2 with a brief summary our methods for simulating hydrogen reionization. We then present our results in Section 3.3, focusing on the history of reionization in Section 3.3.1, the Lyman-α forest in Section 3.3.2 and the feedback from reionization in Section 3.3.3. We end with a discussion and our conclusions in Section 3.4.

3.2. Simulating hydrogen reionization

3.2.1. Radiative transfer modeling

For our work we use an updated version of the cosmological simulation code GADGET (Springel et al., 2001; Springel, 2005), combined with the radiative transfer (RT) implementation of Petkova & Springel (2009). The RT equation is solved using a moment-based approach similar to the one proposed by Gnedin & Abel (2001). The resulting partial differential equation essentially describes an anisotropic diffusion of the photon density field n_γ,[1]

$$\frac{\partial n_\gamma}{\partial t} = c \frac{\partial}{\partial x_j} \left(\frac{1}{\kappa} \frac{\partial n_\gamma h^{ij}}{\partial x_i} \right) - c\,\kappa\,n_\gamma + s_\gamma, \tag{3.1}$$

where c is the speed of light, κ is the absorption coefficient, h^{ij} is the Eddington tensor and s_γ is the source function. The closure relation for this particular moment-based method is obtained by approximating the Eddington tensor h^{ij} as

$$h^{ij} = \frac{P^{ij}}{\mathrm{Tr}(P)}, \tag{3.2}$$

where P^{ij} is the radiation pressure tensor

$$P^{ij}(x) \propto \int \mathrm{d}^3 x' \rho_*(\mathbf{x}') \frac{(\mathbf{x} - \mathbf{x}')_i (\mathbf{x} - \mathbf{x}')_j}{(\mathbf{x} - \mathbf{x}')^4}. \tag{3.3}$$

This estimate of the Eddington tensors is carried out in the optically thin regime, giving the method its name.

We have tested our radiative transfer implementation on the static cosmological density field that was used in the radiative transfer code comparison study by Iliev et al. (2006b). In Figure 3.1 we show the ionized fraction in a slice through the simulated volume at evolution time $t = 0.05\,\mathrm{Myr}$. Reassuringly, our result is in good agreement with the ones obtained by other radiative codes in the comparison study.

---

[1]Differently from Petkova & Springel (2009) we solve equation (3.1) for the photon density n_γ, rather than the photon overdensity, with respect to the hydrogen density $\tilde{n}_\gamma = n_\gamma/n_\mathrm{H}$.
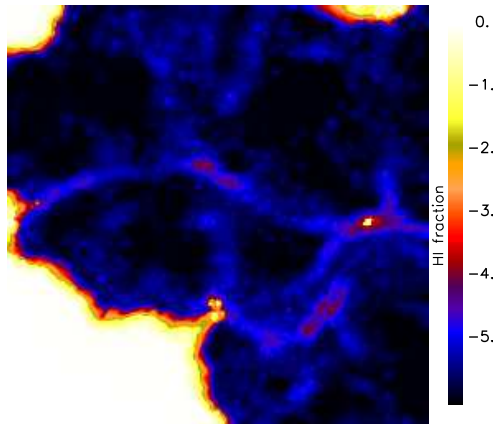
Figure 3.1: Ionized fraction in a slice through the simulated volume at evolution time $t = 0.05\,\mathrm{Myr}$ of the cosmological density field test described in Iliev et al. (2006b)

3.2.2. Treatment of star formation

Winds and star formation in the dense, cold gas is modeled in a sub-resolution fashion (Springel & Hernquist, 2003a), where the interstellar medium is pictured as being composed of cold clouds that are embedded at pressure equilibrium in a hot tenuous phase that is heated by supernova explosions. Through the evaporation of clouds, this establishes a tight self-regulation of the star formation rate. Previous work has shown that this model converges well with numerical resolution and yields star formation rates that are consistent with the Kennicutt relation (Kennicutt, 1998) observed at low redshift. We shall here assume that the same star formation law also holds at high redshift.

We use the star-forming regions in all simulated galaxies as sources of ionizing photons in our radiative transfer model. We adopt an ionizing source luminosity of $\dot{N}_{\mathrm{SFR}} = 10^{53}$ photons $\mathrm{M}_\odot^{-1}\,\mathrm{yr}$ (Madau et al., 1999), which relates the number of emitted photons to the star formation rate in units of $\mathrm{M}_\odot \mathrm{yr}^{-1}$. This source luminosity is released individually by every star-forming gas particle, hence the number of numerically represented sources is a non-negligible fraction of all simulation particles. Fortunately, the speed of our radiative transfer algorithm is almost insensitive to the total number of sources, because the Eddington tensor calculation can be carried out with a tree algorithm similar to the gravity calculation. This insensitivity of the computational cost to the number of sources is a significant advantage of the method used here, and is not shared by most alternatives for treating radiative transfer.

To account for the uncertain absorption that occurs in reality in the spatially unresolved multi-phase structure of our simulations, we impose a phenomenological efficiency factor η on the source luminosities. In our simulation set we explore values in the range $\eta = 0.1-1.0$ to get a feeling for the sensitivity of our results to this uncertainty. We note however that η should not be confused with what is usually called galaxy escape fraction, which has a slightly different meaning. Our η is meant to be just an 'interstellar medium escape
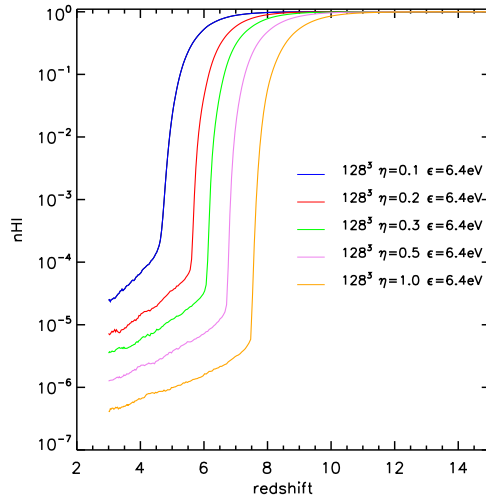
Figure 3.2: Volume averaged neutral fraction as a function of redshift for the low resolution simulations. The different colors represent simulation results for different values of the efficiency parameter (or 'ISM escape fraction') $\eta = 0.1, 0.2, 0.3, 0.5, 1.0$. Reionization happens earlier for higher efficiency since then more photons become available for ionizing the gas. In all cases, the final phase of reionization proceeds rapidly; over a small range of redshift, the neutral volume fraction drops from 10% to negligibly small values.

fraction' whereas photon losses in the gaseous halos of galaxies will be taken into account self-consistently in our simulations.

3.2.3. Simulation set

All our simulations assume a ΛCDM universe with cosmological parameters $\Omega_0 = 0.27$, $\Omega_\Lambda = 0.73$, $\Omega_b = 0.044$, $h = 0.7$ and $\sigma_8 = 0.9$. In order to have sufficiently high mass resolution, we follow a comparatively small region in a periodic box of comoving size $L_{\rm box} = 10h^{-1}\,{\rm Mpc}$ on a side. This region is still sufficiently large to give a representative account of the Lyman-α forest at redshift $z = 3$, which is the final time of our runs.

Our primary simulation set has 2×128^3 dark matter and gas particles, giving a mass resolution of $3.04 \times 10^7\,h^{-1}{\rm M}_\odot$ and $5.29 \times 10^6\,h^{-1}{\rm M}_\odot$ in dark matter and gas, respectively. A selected model was also carried out at the much higher resolution of 2×256^3, giving a gas mass resolution of $6.62 \times 10^5\,h^{-1}{\rm M}_\odot$. The gravitational softening was chosen as $1/35$ of the mean particle spacing in each case, corresponding to $\epsilon = 2.23\,h^{-1}{\rm kpc}$ and $\epsilon = 1.12\,h^{-1}{\rm kpc}$ in the two resolution sets. In order to save computational time, most runs were restarted from $z = 20$ with different radiative transfer treatments, such that the higher redshift evolution did not have to be repeated. We have also systematically varied the 'escape fraction' η and the heating efficiency $\tilde{\epsilon}$, considering the values $\eta = 0.1, 0.2, 0.3, 0.5, 1.0$ and $\tilde{\epsilon} = 6.4\,{\rm eV}, 16\,{\rm eV}, 20\,{\rm eV}, 30\,{\rm eV}$ for the low resolution set. For the high resolution run
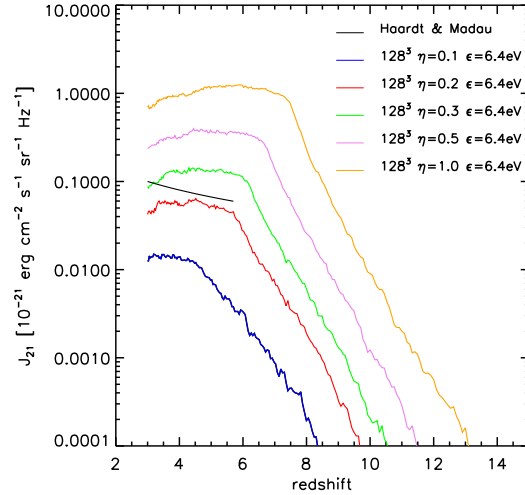
Figure 3.3: Ionizing background for the low resolution simulation as a function of redshift for different efficiency $\eta = 0.1, 0.2, 0.3, 0.5, 1.0$. As expected, the background becomes higher for a larger efficiency since more of the photons emitted by the sources are made available to build up the ionizing background. The thin solid line shows the background computed by Haardt & Madau (1996) for quasars, which provides for an interesting comparison. Our results for the time evolution of the neutral volume fraction agree quite well with previous studies (e.g. Gnedin, 2000).

we chose the parameters $\eta = 0.2$ and $\tilde{\epsilon} = 30\,\text{eV}$. In this way we could systematically determine the settings that give the most promising agreement with the observations.

3.3. Results

3.3.1. Hydrogen reionization history

When star formation starts at around redshift $z = 20$ in our simulations, the process of reionization begins through photoionization of the gas around the star-formation sites. However, as the dense gas has a high recombination rate, the progress in the reionization is sensitively determined by a competition between the luminosity of the sources, the rate with which they turn on, and the density of the neutral gas they are embedded in. Using our simulation set, we first investigate the global reionization history and its dependence on the source efficiency parameter η.

Figure 3.2 shows the reionization histories of our low resolution simulated box for several choices of η. As expected, the results for the reionization redshift depend strongly on η. For larger efficiencies, the Universe gets reionized earlier, since more photons become available to ionize the hydrogen. This effect always overwhelms the reduction in star formation and hence source luminosity that an increased efficiency parameter η also induces. In all cases
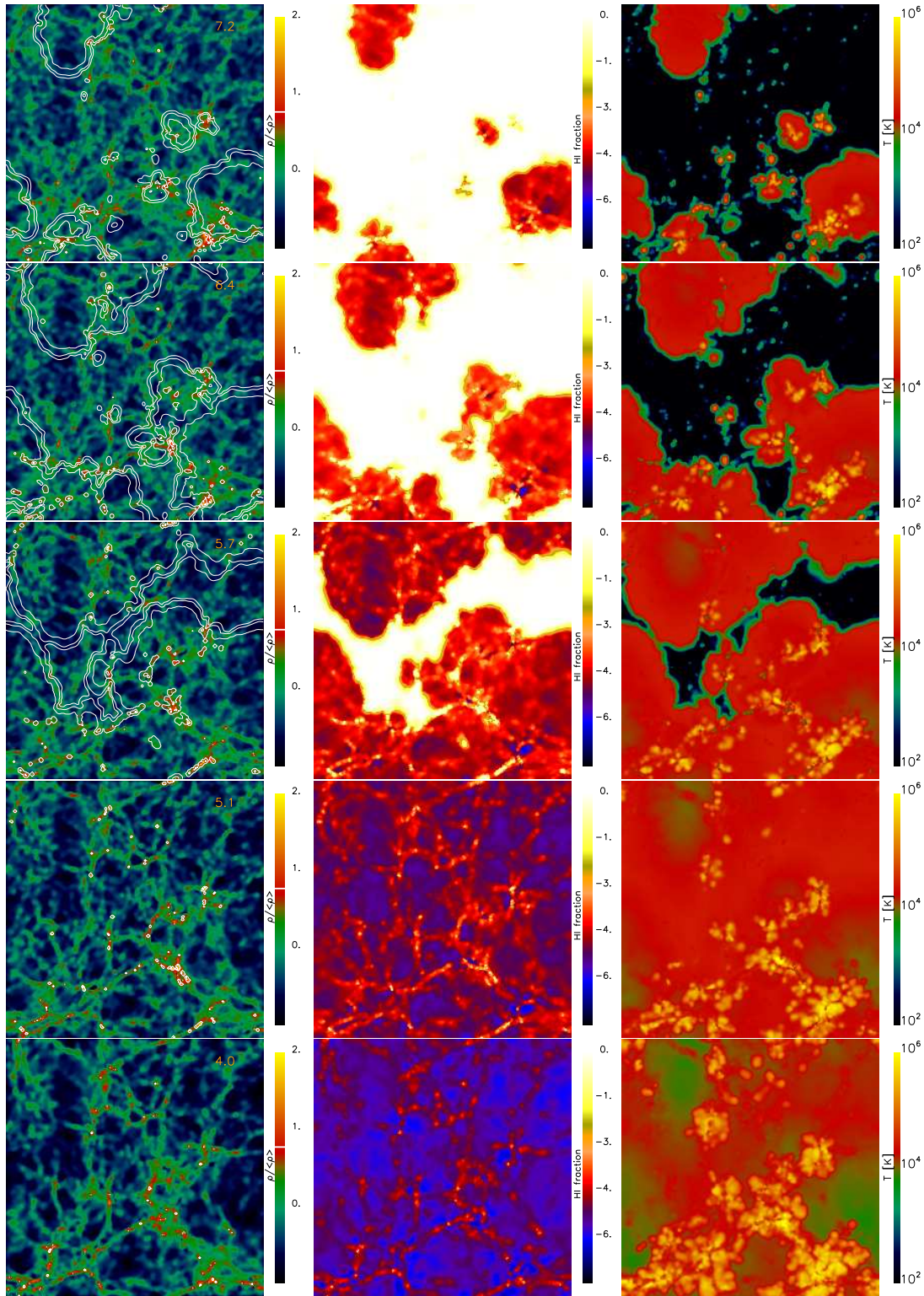
Figure 3.4: Slices through the middle of the simulated volume for the low resolution simulation realization with $\eta = 0.1$ and $\tilde{\epsilon} = 30\,\text{eV}$. The maps are showing the density (left) with contours at ionized fraction $\tilde{n}_{\text{HII}} = 0.001$, 0.5 and 0.9 overlaid, ionized fraction (middle), and temperature (right) of the gas. The snapshots show a time evolution from top to bottom, with individual redshifts $z = 7.2$, $z = 6.4$, $z = 5.7$, $z = 5$ and $z = 4$, respectively.
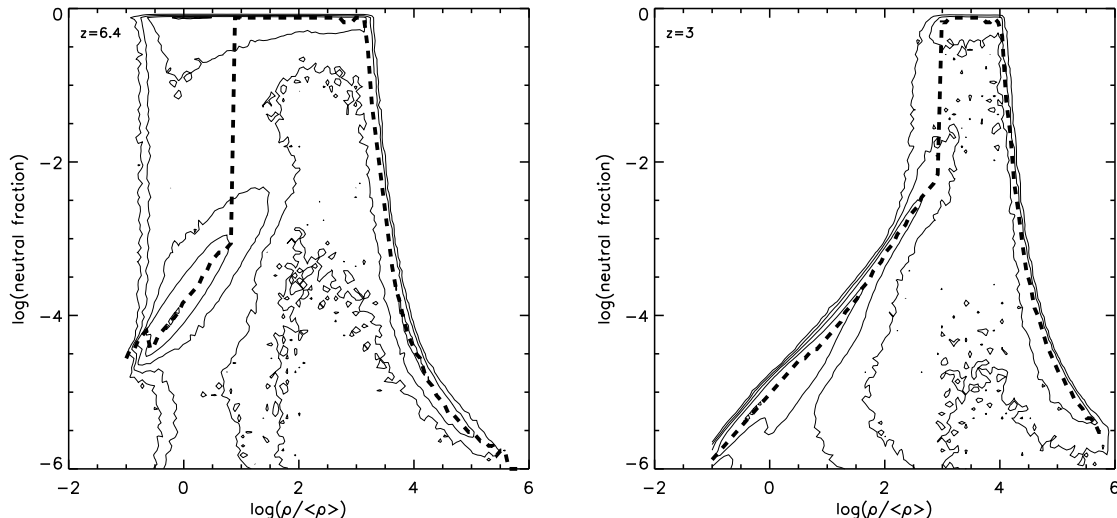
Figure 3.5: Scatter plot of the neutral fraction as a function of overdensity for two different redshift of the low resolution simulation realization with $\eta = 0.1$ and $\tilde{\epsilon} = 30\,\mathrm{eV}$. The thick dashed line is the median neutral fraction. The neutral fraction shows a clear dependence with density, where high density regions are more ionized than low density regions. Very high density gas is highly ionized as well, because it is in the star forming stage.

the last phase of the Epoch of Reionization (EoR) is rather short, i.e. the final 10% of the volume transition very rapidly from being neutral to being essentially fully ionized. The redshift of reionization when this occurs varies between $z \sim 5$ and $z \sim 8$ for $\eta = 0.1$ and $\eta = 1.0$, respectively. In contrast, the EoR starts in general at much higher redshift. For example, the highest efficiency $\eta = 1.0$ model has already ionized nearly 30% of the volume by redshift $z = 10$. Interestingly, there is a systematic variation of the time it takes to complete the last phase of the EoR. This is much more rapid for the high efficiency model than for the lower efficiency ones. Since typical bubble sizes at redshift $z = 6$ are up to $10\,h^{-1}\mathrm{Mpc}$, we note that the size of our simulation box is really too small to draw any definitive conclusions about the global duration of reionization in the Universe. A number of authors (Ciardi et al., 2003; Furlanetto & Oh, 2005; Furlanetto & Mesinger, 2009) have pointed out that the local reionization history depends on the environment, so that, for example, the evolution of the neutral fraction in a field or void region is different than in a protocluster region. As a result, only very large simulation volumes of $100\,h^{-1}\mathrm{Mpc}$ or more on a side can be expected to yield a truly representative account of cosmic reionization. Since at the same time an equal or better mass resolution as we use here is required, such calculations are very expensive and beyond the scope of this work, but the should become feasible in the future on the next generation of high-performance computers.

In Figure 3.3 we compare the ionizing background for the same simulations, which gives further interesting clues about the reionization histories of the different models. The back-
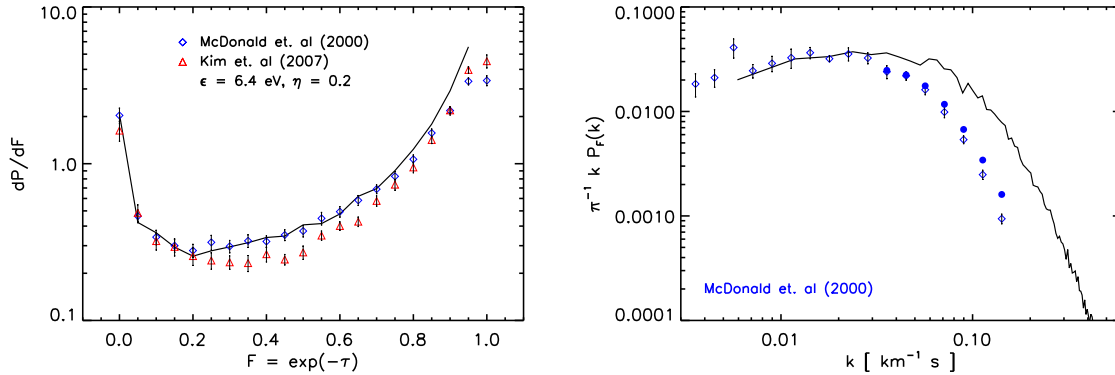
Figure 3.6: Lyman-α flux probability (left) and power spectrum (right) from the low resolution simulation with $\eta = 0.2$ and $\tilde{\epsilon} = 6.4\,\text{eV}$ at redshift $z = 3$. The result is compared with observational data from McDonald et al. (2000) and Kim et al. (2007). The flux probability agrees reasonably well with observations, whereas the power spectrum deviates at the high k end. We discuss this problem in the text.

ground is computed as the volume-averaged intensity in the simulation box. The ionizing background is compared with an analytical estimate by Haardt & Madau (1996) for the meta-galactic ionizing flux from quasars rather than stellar sources, which is an interesting comparison point for the expected value of the background. Clearly, lowering the efficiency η decreases the ionizing background as well, consistent with the findings above. Interestingly, the rapid rise of the mean background intensity ends when reionization is complete. From this point on, the background shows only a weak residual evolution.

The time evolution of the temperature, ionized fraction and density fields in a representative simulation model ($\eta = 0.1$ and $\tilde{\epsilon} = 30\,\text{eV}$) is illustrated in Figure 3.4. The different panels correspond to slices through the middle of the simulation box, between redshifts $z = 7.2$ and $z = 4$, from the top row to the bottom row. It is seen that the ionized regions start to grow first around high density peaks, where the star forming regions are concentrated. Then the radiation diffuses into the inter-cluster medium. The filaments remain less ionized than the voids for a while, since their density is much higher. Initially the photons heat up the gas in the ionized region to temperatures slightly above 10^4K. As the ionizing background declines due to the expansion of the Universe and the drop of star formation, the heating becomes less effective and the temperature of the highly ionized gas in the voids drops somewhat as a result of the expansion cooling.

In Figure 3.5, we present a contour plot of the neutral fraction versus the overdensity of the gas in the representative model for two different redshifts, at $z = 6.4$ before reionization is completed, and at $z = 3$ after reionization is completed. There is a clear dependence of the neutral fraction on overdensity in both cases. The high density regions around star-forming matter are ionized very quickly. The average density regions, e.g. filaments, tend to be less ionized and get ionized after the low density regions. However, note that in the star-forming tale of the diagram all the gas is ionized. This is here due to the star formation
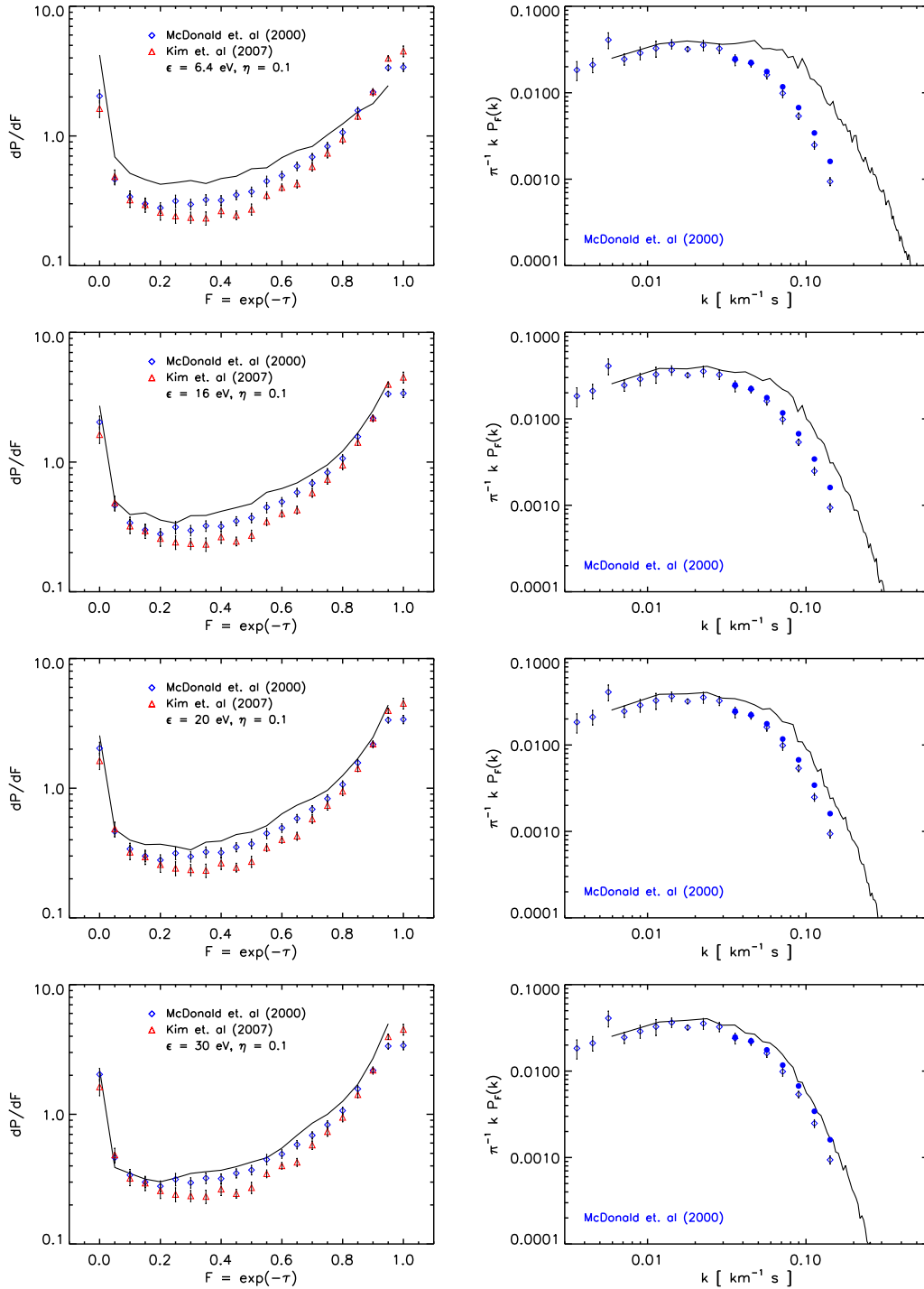
Figure 3.7: Lyman-α flux probability (left) and power spectrum (right) for the low resolution simulation with efficiency $\eta = 0.1$, for four different values of the averaged excess photon energy $\tilde{\epsilon} = 6.4\,\mathrm{eV}$, $16\,\mathrm{eV}$, $20\,\mathrm{eV}$, $30\,\mathrm{eV}$. The simulated data is compared to the observational result from McDonald et al. (2000) and Kim et al. (2007).
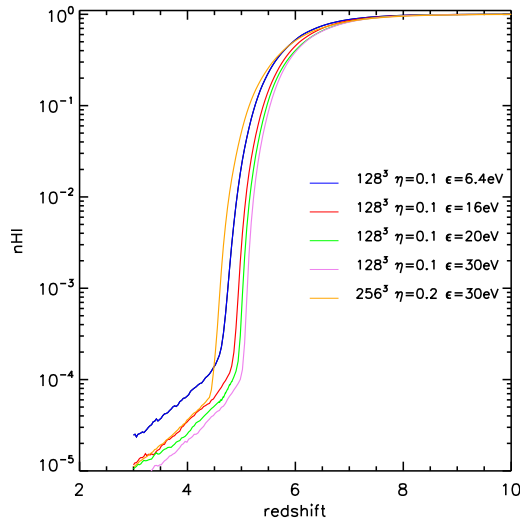
Figure 3.8: Volume averaged neutral fraction as a function of redshift. The set of low resolution simulations with efficiency η = 0.1 and average photon excess energy $\tilde{\epsilon}$ = 6.4 eV, 16 eV, 20 eV, 30 eV is compared with the high resolution run with $\eta = 0.2$ and $\tilde{\epsilon} = 30$ eV. When a higher energy per ionizing event is injected, the universe gets ionized slightly earlier since higher temperatures help to maintain higher ionized fractions.

scheme adopted in GADGET, where star-forming gas particles are assigned a mean mass-weighted temperature which is so high that all this gas is formally collisionally ionized. We note that these results are very similar to the ones reported by Gnedin (2000), where a similar relation between neutral fraction and density is found. However, we are able to probe somewhat higher densities thanks to better spatial resolution of our simulations.

3.3.2. Lyman-α forest

We next turn to an analysis of the thermal state of the intergalactic medium left behind at $z = 3$ by our self-consistent reionization simulations. To this end we use the gas density, gas temperature, gas velocity and ionization state of the gas in the simulation box and compute Lyman-α absorption spectra for random lines of sight. We then compare the statistics of these artificial absorption spectra with observational data on the Lyman-α forest at this epoch, as given by McDonald et al. (2000) and Kim et al. (2007). Here we assume that the main source of ionizing sources is stellar and thus discard any contribution from a quasar-type spectra, in agreement with Madau et al. (1999). We also note that some discrepancies are possible due to the fact that helium is not photoionized in our simulations, but only collisionally ionized.

Our simulations have the necessary gas mass resolution at redshift $z = 3$ required to reproduce realistic Lyman-α absorption in the low density regions (Bolton & Becker, 2009).
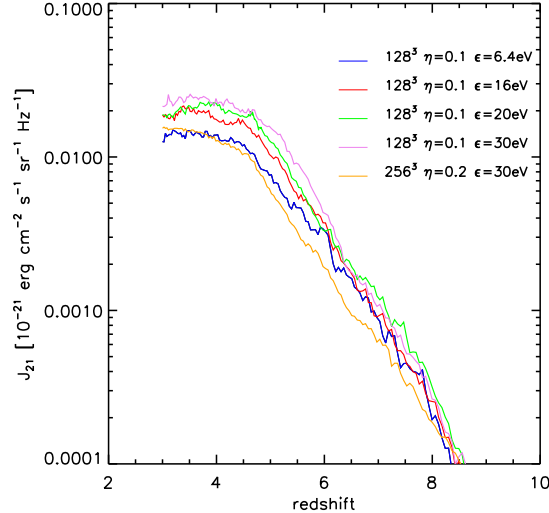
Figure 3.9: Ionizing background as a function of redshift. The set of low resolution simulations with efficiency $\eta = 0.1$ and averaged photon excess energy $\tilde{\epsilon} = 6.4\,\text{eV}$, $16\,\text{eV}$, $20\,\text{eV}$, $30\,\text{eV}$ is compared with the high resolution run with $\eta = 0.2$ and $\tilde{\epsilon} = 30\,\text{eV}$. For a higher injected energy per ionization event, the background also increases as a result of the higher temperature, which leaves more photons unabsorbed so that they can contribute to a higher level of the ionizing background.

However, we can not match the required simulation volume of size $\sim 40\,h^{-1}\text{Mpc}$ to properly sample the largest voids. This can have a significant effect on our predictions of the Lyman-α flux probability distribution and power spectra.

Figure 3.6 shows the flux probability distribution function (PDF) and flux power spectrum for our simulation model, where an efficiency parameter of $\eta = 0.2$ and averaged photon excess energy $\tilde{\epsilon} = 6.4\,\text{eV}$ were adopted. For this choice, we achieve the best fit to the flux PDF. However, for all the other models the power spectrum is overpredicted at high wave numbers. We suggest that this overestimation of the power spectrum is due to the insufficient heating of the gas in low density regions, causing an excess of small-scale structure in the Lyman-α forest.

In order to examine this effect further, we vary the photon excess energy $\tilde{\epsilon}$ used in the photoheating and examine the influence this has on the flux probability and power spectrum. There are two possible reasons why our simulations underestimate the photo heating. First, we expect that some non-equilibrium effects in the photoheating are treated inaccurately due to our implicit treatment of the radiation transport and chemistry (e.g. Bolton & Becker, 2009). Second, photoheating is different in optically thin and optically thick regions. For example, in an optically thick region the average photon excess energy obtained from Eqn. (2.77) is $\tilde{\epsilon} = 29.9\,\text{eV}$. It is however likely that our approximative radiative transfer scheme leads to inaccuracies in the effective heating rates of regions of
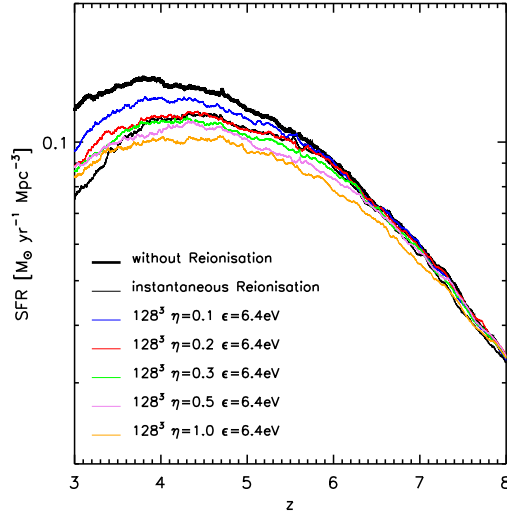
Figure 3.10: Star formation rate density as a function of redshift for the low resolution simulation set at different efficiencies of $\eta = 0.1, 0.2, 0.3, 0.5, 1.0$. The results are compared to the SFR history of a low resolution simulation with instantaneous reionization at $z = 6$ and photoheating by a Haardt & Madau (1996) ionizing background (thin black line), and a simulation with neither reionization nor photoheating (thick black line). The photoheating from stellar sources decreases star formation, as suggested by Pawlik & Schaye (2009). As the escape efficiency gets higher, this effect becomes progressively stronger.

different optical depths, due to the varying accuracy of the scheme in different regimes. Part of these inaccuracies can be absorbed into a suitably modified value of the effective heating rate $\tilde{\epsilon}$. To explore the full range of plausible values, we therefore vary the values for $\tilde{\epsilon}$ as follows: $\tilde{\epsilon} = 6.4\,\mathrm{eV}, 16\,\mathrm{eV}, 20\,\mathrm{eV}$ and $30\,\mathrm{eV}$. We aim to bracket what can be expected when non-equilibrium effects are fully taken into account in future treatments, and want to identify the case that provides the best representation of the Universe at redshift $z = 3$.

Figure 3.7 shows the flux PDF and power spectra for these different heating values. Clearly, the high wave number region of the flux power spectrum is strongly influenced by the amount of injected heat energy into the gas, and the increase of the temperature also affects the flux probability distribution. For the low efficiency of $\eta = 0.1$, there is a substantial mismatch already in the flux PDF, simply because there is too little ionization overall so that the mean transmission ends up being too low. However, as the adopted photoheating energy increases, the gas is getting hotter and is able to stay ionized longer due to the higher temperatures, yielding a better fit to the flux PDF. At the same time, small-scale structure in the flux power spectrum is erased due to thermal broadening, bringing the simulations into agreement with the observation. This shows the power of detailed Lyman-α data to constrain simulations of the reionization process. In our current models we need to adopt a quite extreme heating efficiency of $30\,\mathrm{eV}$ combined with a low
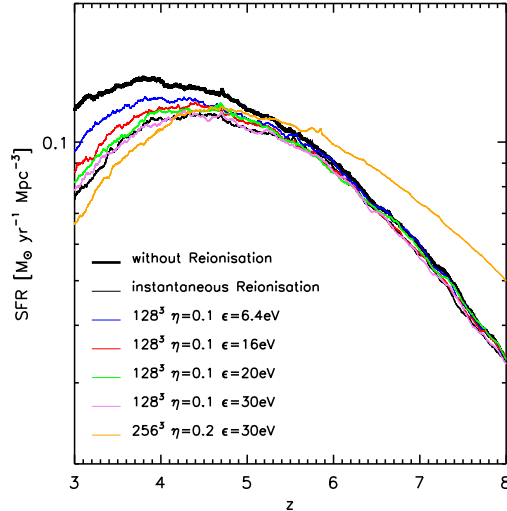
Figure 3.11: Star formation rate density as a function of redshift. The set of low resolution simulations with efficiency $\eta = 0.1$ and averaged photon excess energy $\tilde{\epsilon} = 6.4\,\text{eV}$, $16\,\text{eV}$, $20\,\text{eV}$, $30\,\text{eV}$ are compared to the high resolution run with $\eta = 0.2$ and $\tilde{\epsilon} = 30\,\text{eV}$. The results are compared to the SFR history of a low resolution simulation with instantaneous reionization at $z = 6$ and photoheating by a Haardt & Madau (1996) ionizing background (thin black line), and a simulation with neither reionization nor photoheating (thick black line). The star formation decreases with increasing heating energy, as expected. For the low resolution run with $30\,\text{eV}$, the result of the self-consistent radiative transfer calculation matches the simulation with instantaneous reionization. The high resolution simulation SFR is higher at higher redshift due to better resolution and agrees well with the other results at redshifts less than $z = 6$.

'escape fraction' of $\eta = 0.1$ to achieve a good match to the data.

In Figures 3.8 and 3.9 we compare the impact of the different photoheating efficiencies on the evolution of the neutral volume fraction and the ionizing background. We also show for comparison the results from our high resolution simulation, which is discussed below in the text. As expected, an increase in the heating energy leads to a slightly earlier reionization and to a slightly elevated ionizing background flux. Both of these effects can be readily understood from the higher gas temperature produced in the ionized gas when the higher heating efficiency is adopted. However, the effect is quite weak, and very much smaller than the changes resulting from a different choice of η.

We have also measured the Thomson electron scattering optical depth in our high resolution simulation and found it to be $\tau_{\text{es}} = 0.049$, which is smaller than the WMAP7 value $\tau_{\text{es}}^{\text{WMAP}} = 0.088 \pm 0.015$ (Komatsu et al., 2010). This discrepancy is, however, not critical since the simulated volume is too small to obtain a realistic value and we have also not included photoionization of helium.
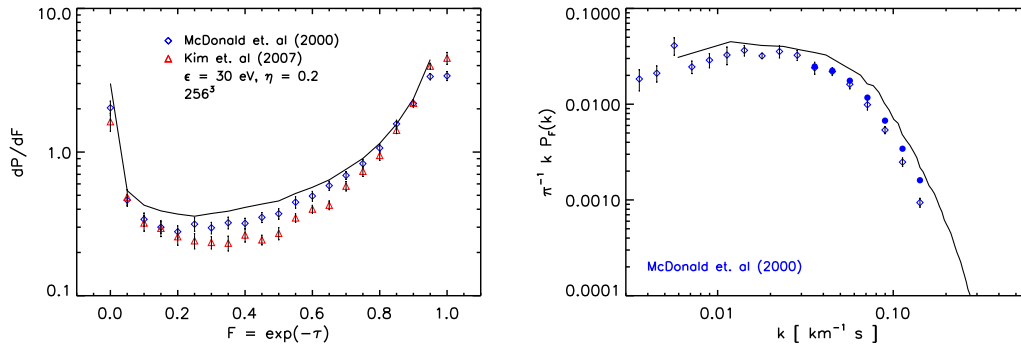
Figure 3.12: Lyman-α flux probability (left) and power spectrum (right) for the high resolution simulation with efficiency $\eta = 0.2$ and averaged excess photon energy $\tilde{\epsilon} = 30\,\mathrm{eV}$, compared to observational results from McDonald et al. (2000) and Kim et al. (2007).

3.3.3. Feedback from reionization

Reionization can in principle exert a strong feedback effect on the gas through the temperature increase induced by photoheating. As the gas temperature increases, the gas densities will be lowered through pressure effects. The gas will then cool and collapse more slowly, such that the star formation rate is ultimately reduced. Especially small dark matter halos should be sensitive to this effect. In the extreme case of halos that have virial temperatures comparable to or only slightly larger than the temperature reached by the gas through reionization, the UV radiation may even completely suppress atomic cooling and efficient star formation. This effect is often invoked to explain why so many of the dark matter satellites expected in ΛCDM in the halos of ordinary $L_\star$ galaxies are apparently largely devoid of stars.

In order to highlight the radiative transfer effects on the star formation in galaxies, we compare our simulations with two fiducial models where no radiative transfer is used. The first is a simulation simply without any photoheating of the gas, while the second one is a simulation where reionization is induced by an externally imposed, spatially homogeneous UV background based on a modified Haardt & Madau (1996) model that causes reionization and an associated photoheating of the gas at $z = 6$ (for details see Davé et al., 1999). The latter model corresponds to the standard approach applied in many previous hydrodynamical simulation models of galaxy formation (e.g. Tornatore et al., 2003; Wadepuhl & Springel, 2010).

In Figure 3.10, we compare our results for the cosmic star formation rate density evolution as a function of the adopted efficiency parameter η (for the low resolution simulation set). We also include the two fiducial comparison models as limiting cases. As we increase the escape efficiency of the ionizing radiation, the star formation drops, as expected, since this makes more photons available to photoheat the gas. We note that our results for the SFR are always lower than the fiducial simulation where no photoheating is included at all, consistent with findings by Pawlik & Schaye (2009). Towards lower redshift, the reduction of the SFR due to the radiation field becomes progressively larger. The run with $\eta = 0.2$
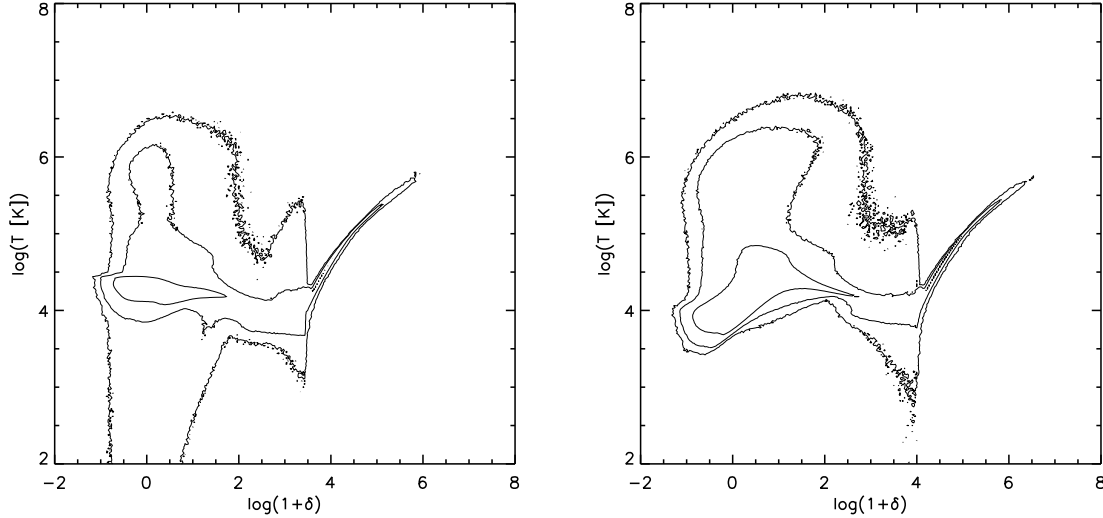
Figure 3.13: Cosmological equation of state: scatter plot of the gas temperature as a function of overdensity for two different redshift $z = 5.09$ (left) and $z = 3$ (right) of the high resolution simulation realization with $\eta = 0.2$ and $\tilde{\epsilon} = 30\,\mathrm{eV}$.

quite closely corresponds to the simulation with the imposed reionization epoch, but starts to slightly differ at redshifts $z < 4$.

We also carry out a corresponding comparison for a low resolution simulation set with constant efficiency $\eta = 0.1$ but different values for the photon excess energy. In Figure 3.11 we show the results for the SFR, again including the two fiducial models as limiting cases for comparison. The results confirm the expectation that an increase of the photon excess energy decreases the star formation rate density. Interestingly, the model that best reproduced the Lyman-α power spectrum observations, the one with $\tilde{\epsilon} = 30\,\mathrm{eV}$, quite closely follows the star formation rate density obtained for the fiducial model where reionization is imposed at $z = 6$.

For our high resolution run we chose to repeat the simulation with averaged photon excess energy $\tilde{\epsilon} = 30\,\mathrm{eV}$ and adopt a higher escape fraction $\eta = 0.2$ rather than $\eta = 0.1$. In this way we make sure we account for the trapping of photons in high density peaks, which were not present in the low resolution runs. In Figure 3.11 we show how the star formation rate history compares to the ones from the low resolution runs. They are in good agreement, except for the higher redshift, where the high resolution captures more star formation, as expected (Springel & Hernquist, 2003b). The Lyman-α forest flux probability and power spectrum at $z = 3$ for this simulation are shown in Figure 3.12. While the simulated data is in reasonable qualitative agreement with the observational results from McDonald et al. (2000) and Kim et al. (2007), it does not provide in this case a detailed fit within the error bars, again highlighting that simultaneously accounting for the cosmic star formation history, cosmic reionization and the state of the IGM at intermediate redshifts provides a
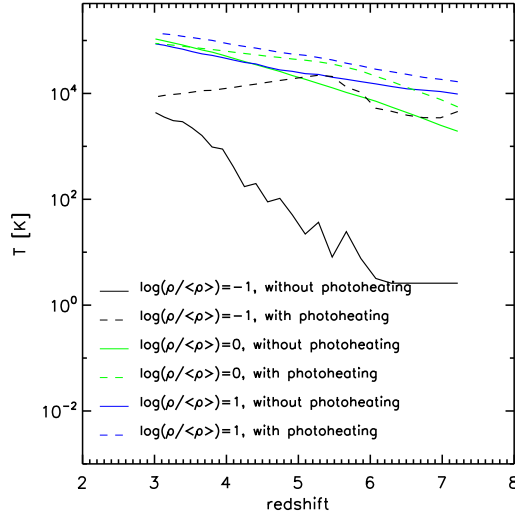
Figure 3.14: Evolution of the mass averaged temperature at three different overdensities $\log_{10}(\rho/\langle\rho\rangle) = -1, 0, 1$ for the low resolution simulation with $\eta = 0.1$ and $\tilde{\epsilon} = 30\,\mathrm{eV}$, with and without photoheating. The strongest effect is observed in the low density gas, which is heated by the photons much more than the higher density gas. At all densities, however, photoheating increases the temperature, as expected.

powerful constraint on self-consistent simulations of galaxy formation and reionization.

In Figure 3.14, we explore the temperature evolution of the gas at different characteristic densities, corresponding to under-dense gas by a factor of 10, gas at the mean density, and overdense gas by a factor of 10 relative to the mean. We compare our default simulation with radiative transfer and photoheating to the fiducial simulation where no such heating is included at all. Clearly, the effect of photoheating is most prominent in the lowest density gas. This gas is only weakly heated by structure formation shock waves when photoheating is not included. In contrast, when reionization is accounted for, the temperature of this gas reaches a high value of $\sim 10^4\,\mathrm{K}$ at the end of the epoch of cosmic reionization, and even before that, the mean temperature of this gas is raised considerably as a result of the patchy and temporally extended reionization transition in our radiative transfer simulations. Interestingly, after reionization is complete, the mean temperature of the under-dense gas starts to slowly decline again, while already for the mean density gas structure formation shocks can provide for a slow further increase of the temperature.

In Figure 3.13 we show the cosmic equation of state for two different redshift $z = 5.09$ and $z = 3$. The plot illustrates the temperature of the gas as a function of overdensity. At the higher redshift, before reionization is completed, some low density gas has temperatures far below $10^4\,\mathrm{K}$. It has not been heated by photons yet. After reionization is completed all low density gas is heated up to approximately $10^4\,\mathrm{K}$.

We also analyzed the median temperature of the gas as a function of overdensity. As
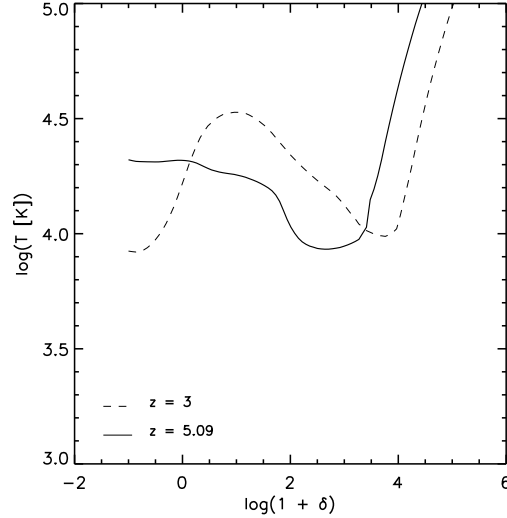
Figure 3.15: Median temperature of the gas as a function of overdensities $\log_{10}(1+\delta)$ at redshifts $z = 5.09$ and $z = 3$ for the high resolution simulation with $\eta = 0.2$ and $\tilde{\epsilon} = 30\,\mathrm{eV}$. At redshift $z = 5.09$, shortly after reionization is completed, the temperature at low densities is clearly higher than that at higher densities (apart from the gas in the star-forming phase). This can be interpreted as an inverted equation of state. At lower redshift the relation reverts again to normal form as the gas in the low density regions cools down adiabatically due to the expansion of the Universe.

shown in Figure 3.15, after reionization has been completed, the low density gas ends up with a higher median temperature than the higher density gas (except for the gas in the star-forming phase). This points towards an 'inverted equation of state', as observed by Bolton et al. (2008a), Trac et al. (2008) and Furlanetto & Oh (2009). At later times, the equation of state reverts again to a normal positive slope, when the low density gas cools down due to the adiabatic expansion of the Universe.

Finally, in Figure 3.16, Figure 3.17 and Figure 3.18 we explore the impact of the ionizing radiation field on the gas and stellar mass content of individual dark matter halos. To this end we run a group finder on our simulations and simply determine the average gas mass, stellar mass and baryon fraction of halos as a function of their dark matter mass. We compare the $z = 3$ results of our higher resolution radiative transfer simulation with the simulation where photoheating is completely ignored. Interestingly, we find a reduction of the gas and stellar mass for all halo masses when radiative transfer is included. The effect is quite weak for large halos but becomes progressively larger for small halos. At dark matter halo masses of $M_{\mathrm{DM}} = 10^9\,\mathrm{M}_\odot$ the suppression in baryonic content is approximately 60%, while at $M_{\mathrm{DM}} = 10^{12}\,\mathrm{M}_\odot$ it drops to only a few percent. This shows clearly the important impact of the ionizing radiation field on small dwarf galaxies, in particular. While an externally imposed UV background can perhaps account for the mean effect of
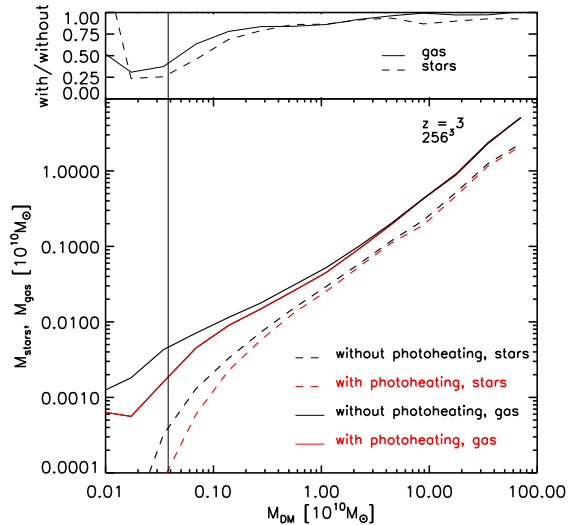
Figure 3.16: Mean stellar and gas masses as a function of the DM halo mass at $z = 3$ in the high resolution simulation. The black vertical corresponds to a mass of 100 DM particles, which can be taken as an (optimistic) resolution limit of the simulation. Photoheating slows down the collapse of gas in halos, which in turn also decreases their stellar and gas masses. The effect becomes stronger for low mass DM halos.

this radiative feedback process (Hoeft et al., 2006; Okamoto et al., 2008), only a spatially resolved treatment of radiative transfer can account for effects of proximity that may well play an important role in shaping, e.g., the satellite luminosity function (Muñoz et al., 2009; Busha et al., 2010; Iliev et al., 2010).

3.4. Discussion and conclusions

We have presented the first application of our new implementation of radiation hydro-dynamics in the cosmological simulation code GADGET. We focused on the problem of cosmic reionization, aiming in particular at a first test on whether the default star formation model in the code combined with our radiative transfer modeling can yield a plausible reionization history of the Universe and a reasonable thermal state of the intermediate redshift intergalactic medium. For simplicity, we have here only studied star-forming galaxies as ionizing sources, and restricted the analysis to hydrogen reionization alone. Based on the encouraging results collected here, it is clearly worthwhile to extend the model further in future work.

Since the level of internal absorption in the interstellar medium is uncertain and cannot be resolved by our simulations, we have examined models with different effective source efficiencies η. Likewise, as we have not included a detailed spectral treatment and the time
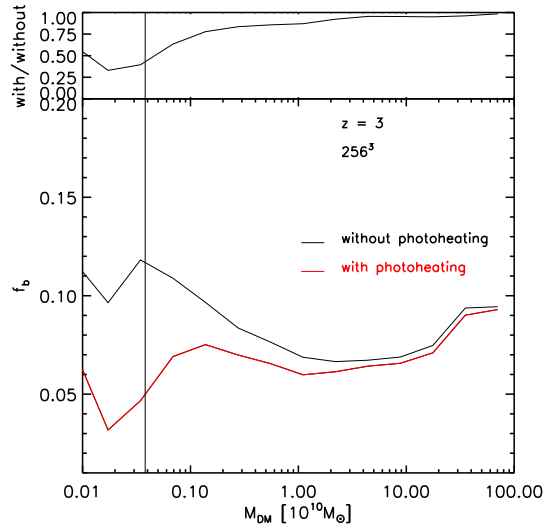
Figure 3.17: Baryon fraction as a function of the DM halo mass at $z = 3$ in the higher resolution simulation. The black vertical corresponds to a mass of 100 DM particles.

evolution of non-equilibrium in the chemistry may be inaccurate, we have parametrized the heat input per ionization event in terms of a parameter $\tilde{\epsilon}$.

We find that our simulated universes can get reionized by star formation in ordinary galaxies alone, with the epoch of reionization ending between redshifts $z = 8$ to $z = 5$, depending on the assumed escape efficiency. The final phase transition is always quite rapid in this our setup, but sizable fractions of the volume begin to be reionized much earlier. The heating efficiency has only a weak influence on the reionization history, but a stronger one on the cosmic star formation rate density. In fact, we have shown that photoheating plays an important role in the evolution of the baryonic gas. As a result of the associated heating, it changes baryonic structure formation by slowing down the collapse of gas in dark matter halos, thereby delaying star formation. This effect is strongest for the lowest mass halos, where the DM potential well is not deep enough to easily overcome the thermal pressure from the effects of photoionization.

Our simple models of a self-consistent treatment of galaxy formation and radiative transfer are not only able to produce a plausible history of reionization, but they also manage to approximately match the basic statistics of the Lyman-α forest, at least for an appropriate choice of the parameters η and $\tilde{\epsilon}$. This suggests that the low-redshift IGM data can be a powerful additional constraint on future reionization modeling in structure formation simulations.

Despite these encouraging results it is also clear that our simulation results are likely still affected by numerical resolution effects, because the resolution in the lowest mass halos is still too coarse to yield fully converged results. Ideally, we would like to resolve the full range of star-forming halos with enough particles to achieve fully converged results. While
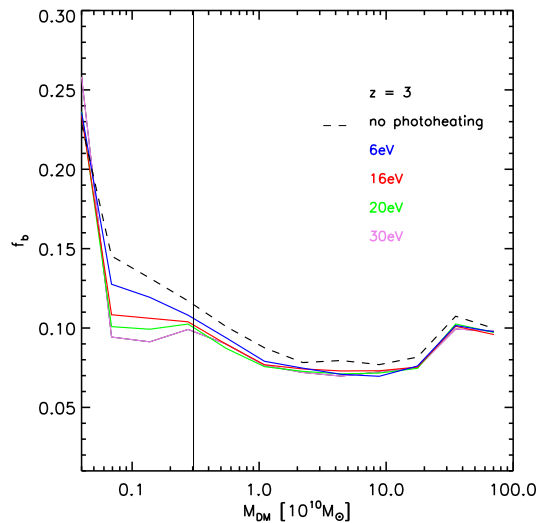
Figure 3.18: Baryon fraction as a function of DM halo mass at $z = 3$ in the lower resolution simulations with efficiency $\eta = 0.1$, and for different averaged photon excess energy. The dashed line shows the baryon fraction when no photoheating has taken place. The black vertical line corresponds to a mass of 100 DM particles. Photoheating does not affect the baryon fraction as strongly as in the high resolution simulation. We also observe that differences in the excess photon energy do not have a large effect on the baryon fraction.

this is unlikely to qualitatively change any of the results presented here, future precision work will require such calculations. Another important caveat that will require further study are uncertainties due to the radiative transfer approximation itself. This is probably best addressed by comparing the results with a completely different approach to radiative transfer.

4

Cosmological radiative transfer in the AREPO code

Based on Petkova, M., & Springel, V., 2010, astro-ph: 1012.1017

4.1. Introduction

It is the goal of this chapter to propose a new numerical scheme for RT that is competitive with the best of the known methods in terms of accuracy and general applicability, but is also fast enough to allow self-consistent radiation-hydrodynamic simulations in the context of cosmological reionization and star formation problems. We also aim to couple the method to the new moving-mesh code AREPO (Springel, 2010), which solves the equations of hydrodynamics on an unstructured Voronoi mesh that moves with the flow and automatically adapts its resolution to the gravitational clustering of matter. This mesh-based code computes hydrodynamics similar to high-accuracy Eulerian codes on Cartesian grids, but it features reduced advection errors when the flow velocity is large.

Our new method is based on a radiation advection technique where a second-order accurate, piece-wise linear reconstruction of the photon intensity field is used to estimate upwind photon fluxes for each face of the mesh. If there is only a single point source, such a scheme can exploit the fact that the local streaming direction of the photons is known everywhere – it is along the ray from the source's position to the local coordinate. If there are multiple sources, the radiation field can be treated equally accurately by decomposing it into a linear sum for each source, and treating each component independently. Alternatively, we introduce a direct discretization of angular space, allowing a description of arbitrary source fields, albeit at the cost of a finite angular resolution. We note that in all these variants the conservation of photon number is manifest in the transport step. We treat the source terms and the coupling to the hydrodynamics in an operator split approach, where the emission, advection, and absorption of radiation are calculated in separate steps. This makes our approach fully photon conserving, which is especially useful for the cosmic reionization problem, as it ensures that all photons emitted by an ionizing source are really used up in exactly one ionization event.

We note that the advection scheme discussed in this chapter normally propagates the photons at their physical speed of light, based on an explicit time integration scheme. While this has the advantage of allowing general, fully time-dependent radiative transfer simulations, it can make them computationally very expensive due to the required small Courant time steps. This can however be greatly alleviated by using a reduced speed of light approximation (Gnedin & Abel, 2001), which allows much larger timesteps while still preserving the speed of cosmological ionization fronts (I-fronts). With this approximation, it then becomes possible to calculate high-resolution cosmological radiation hydrodynamics simulations of structure formation that simultaneously account for cosmic reionization, with no restriction on the number of sources.

In Section 4.2 of this chapter, we present our methodology in detail. We first give a brief introduction to the RT equation in Section 4.2.1. Then we discuss three variants of our solution method for the radiation advection equation in Sections 4.2.2, 4.2.3, and 4.2.4. In Section 4.2.5, we briefly describe our treatment of emission and absorption processes, with an emphasis on the hydrogen chemistry relevant for the cosmic reionization problem, and in Section 4.2.6 we specify our formulation of photoheating and radiative cooling. Issues of time stepping and code implementation are discussed in Sections 4.2.7 and 4.2.8. We move on to a presentation of basic test results in Section 4.3, starting with a variety of shadowing (Section 4.3.1) and Strömgren sphere tests (Section 4.3.2). We then consider the more demanding tests of I-front trapping in Section 4.3.3, the ionization of a cosmological density field in Section 4.3.4, and an ionization problem with dynamic density field in Section 4.3.5. Finally, we present results of a fully self-consistent hydrogen reionization simulation in Section 4.4. We make conclusions in Section 4.5.

4.2. An advection solver for the radiative transfer problem

4.2.1. The radiative transfer equation

Let us briefly discuss different forms of the RT equation, which is helpful to clarify how our new method differs from other approaches, and for specifying our notation. Let $f_\gamma \equiv f_\gamma(t, \mathbf{x}, \mathbf{p})$ be the photon distribution function for comoving coordinate $\mathbf{x}$ and photon momentum

$$\mathbf{p} = a\frac{h\nu}{c}\hat{\mathbf{n}}\,, \tag{4.1}$$

where $a \equiv a(t)$ is the cosmological scale factor, h is the Planck constant, ν is the frequency of the photons, and $\hat{\mathbf{n}}$ is the unit vector in the direction of photon propagation. Then the number of photons in some part of the Universe is

$$N_\gamma = \int \mathrm{d}\mathbf{x}\, \mathrm{d}\mathbf{p}\, f_\gamma(t, \mathbf{x}, \mathbf{p})\,. \tag{4.2}$$

We can quite generally write the phase-space continuity equation for the distribution

function f_γ of photons as

$$\frac{\partial f_\gamma}{\partial t} + \frac{\partial}{\partial \mathbf{x}}(\dot{\mathbf{x}} f_\gamma) + \frac{\partial}{\partial \mathbf{p}}(\dot{\mathbf{p}} f_\gamma) = \left.\frac{\partial f_\gamma}{\partial t}\right|_{\text{sources}} - \left.\frac{\partial f_\gamma}{\partial t}\right|_{\text{sinks}}. \tag{4.3}$$

In this Boltzmann-like transport equation, the source and sink terms on the right-hand side of the equation represent photon emission and absorption processes, respectively. If we neglect gravitational lensing effects, individual photons propagate along straight lines with conserved momenta, i.e. we have $\dot{\mathbf{x}} = (c/a)\hat{\mathbf{n}}$ and $\dot{\mathbf{p}} = 0$. The transport equation hence simplifies to

$$\frac{\partial f_\gamma}{\partial t} + \frac{c}{a}\frac{\partial}{\partial \mathbf{x}}(\hat{\mathbf{n}} f_\gamma) = \left.\frac{\partial f_\gamma}{\partial t}\right|_{\text{sources}} - \left.\frac{\partial f_\gamma}{\partial t}\right|_{\text{sinks}}. \tag{4.4}$$

Normally, a direct use of equation (4.4) through a discretization of phase-space is considered prohibitively expensive due to the high-dimensionality of the problem. However, if only monochromatic radiation is considered, which is often sufficient, the momentum-space dimensions reduce to just two angular coordinates. If furthermore only a relatively coarse angular resolution for the photon transport is sufficient, then the 4π solid angle described by these angular dimensions may be discretized into a limited set of cones, say up to 10-100, at which point a brute-force solution of equation (4.4) on a 3D mesh becomes computationally feasible and attractive, as we shall argue here.

Before we discuss this in more detail, let us first briefly recall for clarity how the specific intensity I_ν that is normally used in RT studies relates to equation (4.4). We can define the specific radiation intensity I_ν in a certain direction $\hat{\mathbf{n}}$ through the energy $\Delta E_\nu = I_\nu \Delta\nu \Delta A \Delta\Omega \Delta t$ of photons that pass through a physical area ΔA normal to $\hat{\mathbf{n}}$ and within solid angle $\Delta\Omega$ around $\hat{\mathbf{n}}$, over a time interval Δt and in a frequency bin $\Delta\nu$. With this definition, the specific intensity I_ν is then related to the photon distribution function f_γ as

$$I_\nu = h\nu f_\gamma \frac{\mathrm{d}^3 x\, \mathrm{d}^3 p}{\mathrm{d}\nu\, \mathrm{d}\Omega\, \mathrm{d}A\, \mathrm{d}t} = \frac{h^4 \nu^3}{c^2} f_\gamma. \tag{4.5}$$

Substituting into equation (4.4), and writing the absorption and emission terms in their conventional form, one obtains the cosmological RT equation in the form

$$\frac{1}{c}\frac{\partial I_\nu}{\partial t} + \frac{\hat{\mathbf{n}}}{a}\frac{\partial I_\nu}{\partial \mathbf{x}} - \frac{H(a)}{c}\left(\nu\frac{\partial I_\nu}{\partial \nu} - 3I_\nu\right) = -\kappa_\nu I_\nu + j_\nu, \tag{4.6}$$

where κ_ν is the absorption coefficient, j_ν is the emission coefficient, and $H(a)$ is the Hubble rate. Defining the solid angle averaged intensity as

$$J_\nu = \frac{1}{4\pi}\int \mathrm{d}\Omega\, I_\nu, \tag{4.7}$$

we can calculate the physical photon number density from the specific intensity as

$$n_\gamma^{\text{phys}} = \frac{1}{c}\int \frac{4\pi J_\nu}{h\nu}\, \mathrm{d}\nu. \tag{4.8}$$
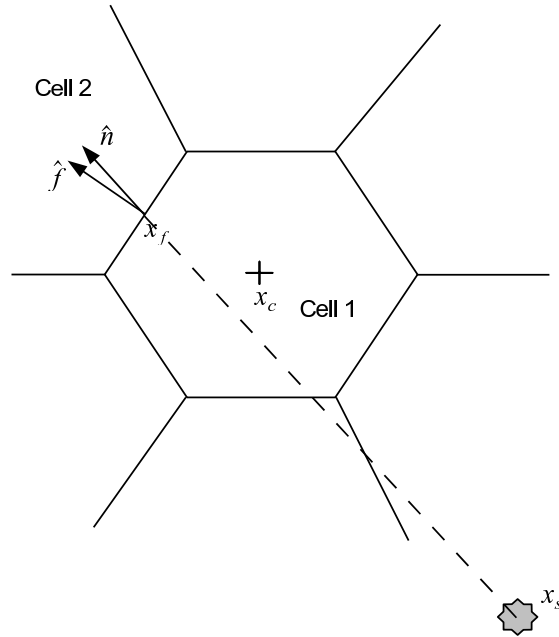
Figure 4.1: A simple sketch showing the geometry involved in our advection scheme for a single point source at coordinate $\mathbf{x}_s$. Here $\hat{\mathbf{n}}$ is the photon propagation direction, $\hat{\mathbf{f}}$ is the normal vector of a face of a cell, $\mathbf{x}_c$ is the center of mass of the corresponding cell and $\mathbf{x}_f$ is the center of mass of the face for which the photon flux is calculated.

Another equivalent way to obtain the photon number density is simply to integrate the distribution function,

$$n_\gamma = \int \mathrm{d}\mathbf{p}\, f_\gamma(t, \mathbf{x}, \mathbf{p}), \tag{4.9}$$

which yields the comoving number density of photons, $n_\gamma = a^3 n_\gamma^{\mathrm{phys}}$. This highlights again that describing the radiation field with the arguably more familiar RT equation (4.6), or with the distribution function and the Boltzmann-like equation (4.4), is fully equivalent. In this chapter, we will mostly work in the latter formulation.

In general, to solve the RT problem on some discretized mesh, we can split off the source and sink terms and treat them separately in the time integration. In such an operator splitting approach, known as Strang splitting, we are basically left with two separate problems that are interleaved in the time integration, one is to follow the conservative transport of photons on the mesh, the other is the local updating of the photon density field through the source and sink terms. In the following, we first focus on the conservative transport problem, which is where the primary computational challenge lies.

4.2.2. Transferring radiation by advection for point sources

Suppose for the moment that we know at a given point in space that all photons stream in the same direction $\hat{\mathbf{n}}$. This is for example the case if there is a single point source
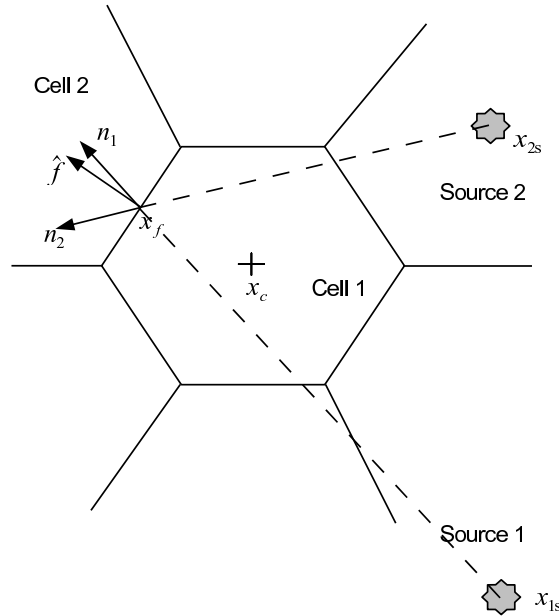
Figure 4.2: Sketch that illustrates the linear summation principle used to treat the radiative transfer for multiple sources. Here $\hat{\mathbf{n}}_1$ and $\hat{\mathbf{n}}_2$ are the photon propagation directions from the two sources, as seen from the center $\mathbf{x}_f$ of a face with normal vector $\hat{\mathbf{f}}$. The total flux passing through the face is then computed as a linear sum of the contributions from the partial fields created by each source.

at coordinate $\mathbf{x}_s$ (i.e. no other sources and no scattering are present). For simplicity, we shall also restrict ourselves to a spatially invariant photon momentum spectrum. One then obtains a simple advection equation for the comoving photon density n_γ:

$$\frac{\partial n_\gamma}{\partial t} + \frac{c\,\hat{\mathbf{n}}}{a} \cdot \nabla n_\gamma = 0, \tag{4.10}$$

where the local advection direction $\hat{\mathbf{n}}$ is known at every point $\mathbf{x}$ and is simply given by

$$\hat{\mathbf{n}}(\mathbf{x}) = \frac{\mathbf{x} - \mathbf{x}_s}{|\mathbf{x} - \mathbf{x}_s|}. \tag{4.11}$$

This advection is conservative and may be solved with the techniques commonly employed to treat the hyperbolic conservation laws of ideal fluid dynamics on spatial meshes. Indeed, this is the approach we are going to employ: we shall use a conservative transport scheme based on a second-order accurate upwind method that is inlined with the hydrodynamic calculations of our unstructured moving-mesh hydrodynamics code AREPO, which is described in some more detail below. It is important to note that knowledge of the local number density field of photons combined with the source location $\mathbf{x}_s$ is sufficient to accurately solve the radiative transport, simply because this information suffices to specify the photon streaming direction at every point in space. Apart from the spatial discretization,

no approximations need to be made for the case of a single monochromatic point source in this treatment.

In practice, we use a second-order accurate spatial reconstruction technique to convert photon numbers N_i stored for each cell i of a given mesh into a photon density field. For every cell, we first obtain an estimate $\langle \nabla n_\gamma \rangle_i$ for the gradient of n_γ, which allows a piece-wise linear conservative reconstruction of the photon density field, in the form

$$n_\gamma(\mathbf{x}) = \langle n_\gamma \rangle_i + \langle \nabla n_\gamma \rangle_i (\mathbf{x} - \mathbf{x}_i^c), \quad \text{for } \mathbf{x} \in \text{cell } i. \tag{4.12}$$

Here $\langle n_\gamma \rangle_i = N_i/V_i$ is the mean photon number density in the cell with center-of-mass $\mathbf{x}_i^c$ and volume V_i. As illustrated in the sketch of Figure 4.1, for every face centroid $\mathbf{x}_f$ of the mesh, we can then identify the upwind side of the photon flow, based on the sign of the dot product between face normal $\hat{\mathbf{f}}$ and the photon streaming direction $\hat{\mathbf{n}} = (\mathbf{x}_f - \mathbf{x}_s)/|\mathbf{x}_f - \mathbf{x}_s|$. This allows us to estimate the photon flux F_γ over the face as

$$F_\gamma = \frac{c}{a} (\mathbf{f} \cdot \hat{\mathbf{n}}) \, n_\gamma(\mathbf{x}_f), \tag{4.13}$$

where the photon density $n_\gamma(\mathbf{x}_f)$ at the face centroid is estimated based on the linear reconstruction of the cell on the upwind side. If the face has comoving area A, the number of photons exchanged during time Δt between the cells that share the face is then given by

$$\Delta N_\gamma = F_\gamma A \Delta t. \tag{4.14}$$

Due to the pairwise exchange of photons, the conservation of total photon number is manifest, which is important for guaranteeing that I-fronts propagate at their physical speeds. We note that in our code the mesh is composed of Voronoi cells (of which a Cartesian mesh is a special case), but this is not important for the general approach.

There are two important caveats with this transport scheme, which need to be pointed out. One is that this explicit transport scheme requires a time step that is given by a local Courant criterion for the photons, which can become very small due to the high speed of light. For reionization problems, this can however be circumvented with the reduced speed of light approximation, which we will discuss in more detail later on. The other caveat is that close to a point source the mesh resolution will always be coarse, so that our use of a single Gauss point per mesh face may introduce sizable errors in the discretized advection fluxes. This can happen when the opening angle under which a mesh face is seen by the point source is large, so that adopting a single propagation direction for the entire face is inaccurate. As a result, isophots of the radiation field produced by the point source may then deviate from sphericity with distortions that reflect the local geometry of the mesh around the point source. We have found however that this problem can be cured quite effectively by injecting the photons of the source in a kernel-weighted fashion over 2-3 mesh cells or so. With such slightly extended sources, the above scheme is able to quite accurately treat single point sources.

The approach can also be straightforwardly extended to multiple point sources simply by linear superposition of the radiation fields produced by each of the individual sources, as
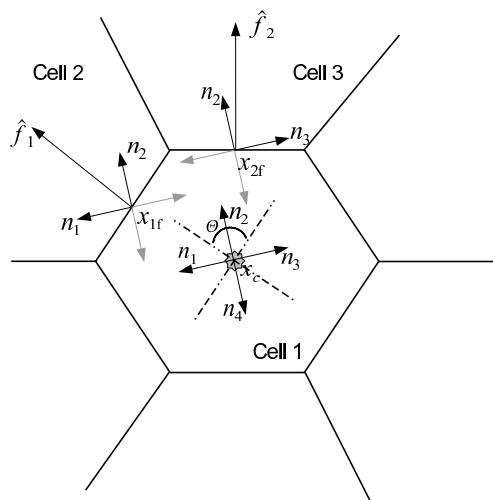
Figure 4.3: This sketch illustrates the geometry and the vectors involved in our "cone transport", where the angular space is discretized into regions of equal angle (in 2D) or solid angle (in 3D). In this example, only four cones in in 2D are used. The photon field is linearly decomposed into radiation fields corresponding to the four cones, which have symmetry axes $\hat{\mathbf{n}}_1$, $\hat{\mathbf{n}}_2$, $\hat{\mathbf{n}}_3$, ... $\hat{\mathbf{n}}_N$, where N is the number of discrete cones or angles, i.e. $N = 4$ in the sketch. At each face of the mesh (here the normal vectors $\hat{\mathbf{f}}_1$ and $\hat{\mathbf{f}}_2$ are shown), photon fluxes for each of the partial fields are estimated. The photon propagation direction is taken to be parallel to the gradient of the total radiation intensity field, constrained to lie within the opening angle of the corresponding cone.

sketched in Figure 4.2. This means that the advection equation is solved for the radiation field of each source separately. This obviously involves a computational and storage cost that scales with the number of sources, but if the number of sources is small, this is an interesting technique for certain applications due to its high accuracy. As we show in our test problems, the method in particular is able to accurately cast shadows, and unlike for example in the optically thin variable Eddington tensor approximation (OTVET), there is no accuracy-degrading mutual influence of multiple sources on each other.

However, for a large number of ionizing sources, the linear superposition approach will quickly become infeasible. For example, in large cosmological simulations, we would like to allow every star particle to act as a source of ionizing radiation. Here we obviously cannot decompose the radiation field into all its single point sources, instead, we need to employ another decomposition. We have actually developed two possible schemes for this, which we describe in the following.

4.2.3. A hybrid between point-source treatment and local diffusion

One possibility to address the multiple point sources problem is to only retain a finite number N_{br} of locally brightest sources in an explicit treatment, while all the remaining sources are lumped together into a background radiation field that is treated with radiative

diffusion. The idea here is that especially in cosmic reionization problems the local ionization "bubble" is expected to be driven primarily by one or a few sources, and only at very late stages, multiple sources may become visible at a given point, but then reionization has largely completed already anyway. By making the set of sources that are treated exactly as point sources spatially variable, we should then get a quite accurate approximation of the reionization phenomenon even for moderate values of $N_{\rm br}$. Since in the limit of large $N_{\rm br}$, the scheme will become essentially exact (apart from spatial discretization errors), the degree to which imposing a limiting value for $N_{\rm br}$ affects the results can be readily tested.

We will discuss some results obtained with this approach later on, but we note that it clearly involves several complication when applied in practice. First of all, the need to allow a local change of the list of bright sources requires that one keeps track of all locally incoming fluxes of radiation, sorting them appropriately, and matching them through the use of unique source identifiers to the already stored radiation intensities from the previous step. Also, since neighboring cells may have different source lists, a matching procedure is required for gradient estimates, with the additional complication that the accuracy of the gradients will be reduced at "domain boundaries", i.e. regions of the mesh that differ in their assessment what the locally most important $N_{\rm br}$ point sources are. Furthermore, if the number of sources is very large and spread out in space (e.g. the individual stars in galaxies), the injection of photons needs to be treated in some sort of clustered fashion, otherwise faint individual sources may not be able to compete with the $N_{\rm br}$ bright sources already stored locally, so that they are channeled into the radiatively treated flux reservoir right away without having a chance to build up to a significant source when combined with the potentially many nearby sources that are equally faint. Finally, one also needs a separate radiative diffusion solver, which requires a small timestep for stability when integrated explicitly in time, as we do here. For all these reasons, we actually favor in most applications our second approach for treating a large number of sources, which is facilitated by discretizing the solid angle explicitly, as we describe next.

4.2.4. Full angular discretization and cone transport

For general radiation fields we seek a method that can directly represent the angular distribution of the local radiation field. This can, for example, be done in terms of moments of the radiation field. However, we here want to propose a more flexible approach that is based on a direct angular discretization of the photon space. To this extent, we can decompose the full solid angle into a set of cones of equal size, for example based on the well-known HEALPIX (Górski et al., 2005) tessellation of the unit-sphere, which we shall use in the following. An example of the tessellation and the different resolutions is shown in Figure 4.5. Our strategy could however be straightforwardly generalized also for other discretization of angular space. In HEALPIX, the unit sphere is decomposed into $N_{\rm pix} = 12\,N_{\rm side}^2$ patches of equal solid angle (which we call "cones" for simplicity, even though they are not exactly axi-symmetric), each centered around a central direction $\hat{\mathbf{n}}_j$, where $j = 1 \ldots N_{\rm pix}$. We now linearly decompose the radiation field f_γ into $N_{\rm pix}$ components, each containing the photons that propagate along a direction within the

corresponding cone:

$$f_\gamma(\mathbf{x}, \hat{\mathbf{n}}) = \sum_j f_\gamma^j(\mathbf{x}, \hat{\mathbf{n}}), \tag{4.15}$$

where $f_\gamma^j(\mathbf{x}, \hat{\mathbf{n}}) = 0$ if the photon direction $\hat{\mathbf{n}}$ lies outside of $\Delta\Omega_j$ around $\hat{\mathbf{n}}_j$. The basic simplification we now make is that we assume that each of the partial radiation fields, $f_\gamma^j(\mathbf{x}, \hat{\mathbf{n}})$, can be taken to be constant as a function of direction within the corresponding cone. Or in other words, each of the partial fields $f_\gamma^j(\mathbf{x}, \hat{\mathbf{n}})$ describes the intensity of a homogeneously illuminated beam of opening angle $\Delta\Omega_j$ around direction $\hat{\mathbf{n}}_j$, emanating from the local coordinate $\mathbf{x}$. Our goal is now to generalize the radiation advection scheme for point sources outlined above such that it can accurately transport the radiation cones occurring in this discretization.

If we simply transport one of the partial radiation fields f_γ^j locally always along the primary direction of its cone, i.e.

$$\frac{\partial f_\gamma^j}{\partial t} + \frac{c\,\hat{\mathbf{n}}_j}{a} \cdot \nabla f_\gamma^j = 0, \tag{4.16}$$

we will invariably observe a central "focusing effect", i.e. the radiation emanating from a point will not illuminate the finite solid angle $\Delta\Omega_j$ homogeneously, but rather tend to concentrate along the primary axis of the cone. It is clear that this "focusing effect" arises from the parallel transport described by equation (4.16); instead of transporting the photon field over different directions that are uniformly spread over the finite solid angle, all of the photons are transported along the single direction $\hat{\mathbf{n}}_j$, with any residual angular spread around $\hat{\mathbf{n}}_j$ arising only from numerical diffusion due to the finite mesh resolution.

One may try to fix this problem by somehow randomizing the direction within the corresponding cone taken in single transport steps, or by using higher-order quadratures in integrating the fluxes arising for a given mesh geometry. However, we have found that a simple trick can be used to resolve this issue, and to obtain close to perfect results even for unfavorable mesh geometries. To this end, we replace the local advection direction $\hat{\mathbf{n}}_j$ appearing in equation (4.16) with a modified direction $\hat{\mathbf{n}}_j'$, chosen along the gradient of the *total* radiation density field, but constrained to lie within the cone j. Specifically, we first adopt

$$\hat{\mathbf{n}}_j' = -\frac{\nabla f_\gamma}{|\nabla f_\gamma|}, \tag{4.17}$$

and calculate the angle between the gradient direction and the cone direction as

$$\phi = \arccos\left(\hat{\mathbf{n}}_j' \cdot \hat{\mathbf{n}}_j\right). \tag{4.18}$$

If this angle is larger than the half opening angle of the cone,

$$\phi^{\max} = \sqrt{(4\pi/N_{\mathrm{pix}})/\pi}, \tag{4.19}$$

then we use the vector $(\hat{\mathbf{n}}_j')_{\mathrm{new}}$, which is defined by the intersection of the plane spanned by $\hat{\mathbf{n}}_j'$ and $\hat{\mathbf{n}}_j$ with the cone of half-opening angle $\phi^{\max}$ (see Figure 4.4). This vector is given by

$$(\hat{\mathbf{n}}_j')_{\mathrm{new}} = \sin\left(\phi^{\max}\right)\mathbf{m} + \cos\left(\phi^{\max}\right)\hat{\mathbf{n}}_j, \tag{4.20}$$
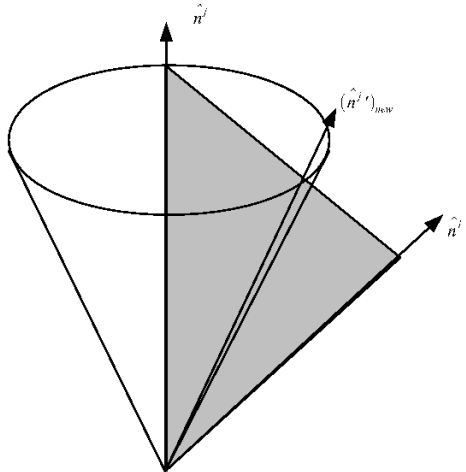
Figure 4.4: A sketch illustrating the construction of the vector given by equation (4.20). The symmetry axis of the solid-angle cone j is given by $\hat{\mathbf{n}}_j$, while the gradient direction is $\hat{\mathbf{n}}'_j$. If the latter lies outside the cone, it is projected onto the cone to yield direction $(\hat{\mathbf{n}}'_j)_{\mathrm{new}}$, which is then used in the local advection step for the cone's radiation field.

where

$$\mathbf{g} = \hat{\mathbf{n}}_j \times \hat{\mathbf{n}}'_j, \tag{4.21}$$

$$\mathbf{m} = \mathbf{g} \times \hat{\mathbf{n}}_j. \tag{4.22}$$

In other words, we transport the radiation corresponding to a certain cone always in the direction of the negative intensity gradient, constrained to lie within the solid angle defined by the cone.

It is clear that this modification has the tendency to smooth out the angular gradient of the radiation field within a cone, making it uniform in the cone. For example, imagine that the transport has led to some intensity excess along the principal direction of the cone. This will then cause some of the transport steps to propagate photons away from the symmetry axis of the cone, slightly more sideways, until the cone is illuminated homogeneously again. But importantly, the constraint we imposed on the advection direction means that all of the photons of any of the partial radiation fields are always transported along a direction "permitted" by their corresponding angular cone. While the specific choice for this direction may hence deviate slightly from the primary cone axis $\hat{\mathbf{n}}_j$, this deviation is strictly bounded, and it will automatically become smaller if a larger number of angular cones is used. One may wonder why we base the initial calculation of the transport direction in equation (4.17) on the total radiation intensity field, and not on the partial cone field f_γ^j alone. This is done to avoid possible boundary effects at the edges of cones, for example when two neighboring cones are both homogeneously illuminated. Using the gradient of the total field will in this case automatically work to eliminate any residuals from the common boundary and to produce a seamless connection of the cones, a feature
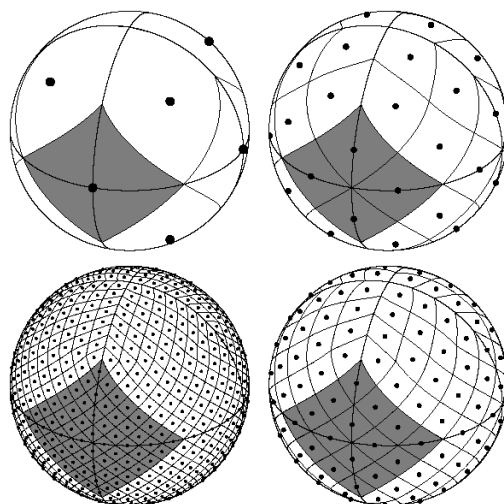
Figure 4.5: Tessellation of the unit sphere as made by the Healpix algorithm (Górski et al., 2005). The upper left image shows the minimum possible number of solid angles - 12. In each further image the resolution is increased by a factor of four.

that is not guaranteed when the gradient of the partial field is used instead. In Section 4.3, we will discuss a number of test problems that illustrate that our simple approach works rather well in practice.

We note that the angular discretization we outlined here is completely independent of the total number of sources. Also, its angular resolution is constant everywhere (at least in the present implementation), even though the spatial resolution of the mesh can vary as a function of position. Another interesting aspect of the method is that it can work accurately both in the optically thin and in the optically thick regime, as well as in the transition region. Unlike in certain approximate treatments of RT, for example in radiative diffusion, we have not made any approximation that changes the fundamental character of the equations, apart from the use of a spatial and an angular discretization. This suggests that the robustness and the convergence of results obtained with this method can reliably be tested by simply changing the grid and/or angular resolution, and if convergence is achieved, then the method should converge to the *correct* solution in the limit of high resolution. The latter property can not necessarily be expected for RT schemes that use more drastic approximations.

4.2.5. Source and sink terms

We treat source and sink terms in the radiative transfer equation through an operator splitting approach, where the evolution of the homogeneous RT equation (which conserves photon number) is alternated with an evolution of the source terms alone. This greatly simplifies the calculation of the interaction of the local radiation field with matter, and also allows accurate balance equations that for example ensure that the number of photons

absorbed matches the number of atoms that are ionized. As an illustrative example, we here detail our implementation of hydrogen chemistry, which can be used in simple model calculations of cosmic reionization.

Emission processes

Emission of ionizing radiation in a cosmological simulation can be based on a variety of source models, tied for example to star-forming gaseous cells, star particles, or sink particles that represent accreting supermassive black holes. Given the source luminosities and their coordinates, we can simply find the cells in which the sources fall, and inject the number of photons emitted by them over the timestep into each of the corresponding host cells. We normally assume isotropic sources where we distribute the total emissivity equally over all angular cones, but in principle also beamed emission characteristics can be realized.

If our single/multiple point source approach is used instead, we spread the source photons over a small region around the host cell with a Gaussian-shaped kernel with a radius equal to a few effective host-cell radii. This is done to avoid potential asymmetries in the source's radiation field that otherwise can arise from the particular geometry of the source cell.

Absorption and hydrogen chemistry

For simplicity, we here discuss a minimal chemical model that only follows hydrogen and an ionizing photon density field with a fixed spectral shape. Extensions to include helium and several ionizing frequencies to account for changes of the spectral shape can be constructed in similar ways.

The neutral hydrogen fraction $\tilde{n}_{\mathrm{HI}}$ evolves due to photoionizations, collisional ionizations and recombinations:

$$\frac{\mathrm{d}\tilde{n}_{\mathrm{HI}}}{\mathrm{d}t} = \alpha n_{\mathrm{H}}\,\tilde{n}_{\mathrm{e}}\tilde{n}_{\mathrm{HII}} - \beta n_{\mathrm{H}}\,\tilde{n}_{\mathrm{e}}\tilde{n}_{\mathrm{HI}} - c\sigma n_{\mathrm{H}}\,\tilde{n}_{\mathrm{HI}}\tilde{n}_{\gamma}, \qquad (4.23)$$

where $\alpha(T)$ is the recombination coefficient, $\beta(T)$ is the collisional ionization coefficient and σ is the effective photoionization cross-section of neutral hydrogen for our adopted spectrum, defined as

$$\sigma = \left[\int \frac{4\pi J_{\nu}(\nu)}{h\nu}\,\sigma_{\nu}(\nu)\,\mathrm{d}\nu\right] \times \left[\int \frac{4\pi J_{\nu}(\nu)}{h\nu}\,\mathrm{d}\nu\right]^{-1}. \qquad (4.24)$$

Here $\sigma_{\nu}(\nu)$ is the frequency dependent photoionization cross-section of neutral hydrogen (with $\sigma_{\nu} = 0$ for frequencies $\nu < \nu_0$ below the ionization cut-off ν_0). The photon density on the other hand evolves according to

$$\frac{\mathrm{d}\tilde{n}_{\gamma}}{\mathrm{d}t} = -c\sigma n_{\mathrm{H}}\,\tilde{n}_{\mathrm{HI}}\tilde{n}_{\gamma}. \qquad (4.25)$$

Here the variables $\tilde{n}_{\mathrm{HI}}$, $\tilde{n}_{\mathrm{HII}}$, $\tilde{n}_{\mathrm{e}}$ and $\tilde{n}_{\gamma}$ express the corresponding abundance quantities in dimensionless form, in units of the total hydrogen number density n_{H}, for example
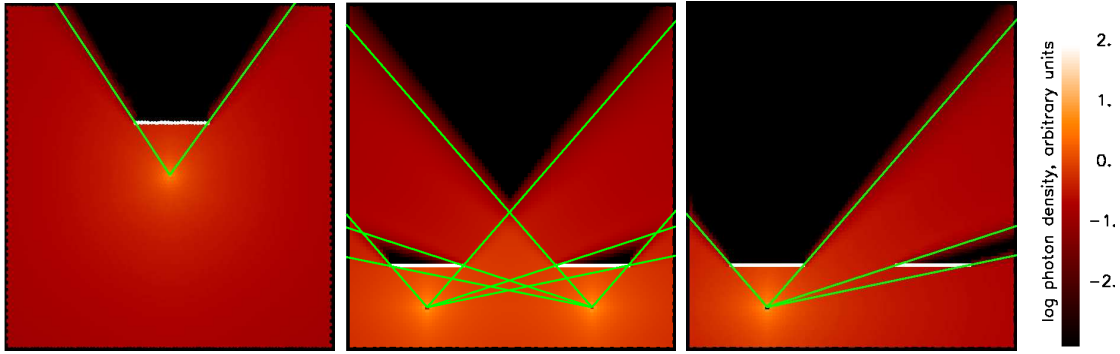
Figure 4.6: *Test (1)*. Photon density maps of 2D shadowing tests in three different cases: single point source with a single obstacle (left panel), two point sources with two obstacles (middle panel), and a single source with two obstacles (right panel). The green lines indicate the geometric boundaries of the expected shadow regions, whereas the thick white lines mark the absorbing obstacles.

$\tilde{n}_\gamma \equiv n_\gamma / n_{\mathrm{H}}$. If we consider only hydrogen, we hence have the constraints $\tilde{n}_{\mathrm{e}} = \tilde{n}_{\mathrm{HII}}$ and $\tilde{n}_{\mathrm{HI}} + \tilde{n}_{\mathrm{HII}} = 1$.

In order to robustly, efficiently and accurately integrate these stiff differential equations, special care must be taken. This is especially important if one wants to obtain the correct post-ionization temperatures, which requires an accurate treatment of the rapid non-equilibrium effects during the transition from the neutral to the ionized state (e.g. Bolton et al., 2005). Also, one would like to ensure that the number of photons consumed matches the number of hydrogen photoionizations, and that the injected photoheating energy is strictly proportional to the number of photons absorbed. We use either an explicit, semi-implicit, or exact integration of equations (4.23) and (4.25) to achieve these goals, depending on the current conditions encountered in each step.

Specifically, we start by first calculating an explicit estimate of the photon abundance change over the next timestep, as

$$\Delta \tilde{n}_\gamma = \tilde{n}_\gamma^{i+1} - \tilde{n}_\gamma^i = -c\sigma n_{\mathrm{H}}\, \tilde{n}_{\mathrm{HI}}^i \tilde{n}_\gamma^i\, \Delta t, \qquad (4.26)$$

where i enumerates the individual timesteps. If the implied relative photon density change is small, say $|\Delta \tilde{n}_\gamma| < 0.05\, \tilde{n}_\gamma^i$, we are either in approximate photoionization equilibrium or the photon density is so large that it does not change appreciably due to hydrogen ionization losses during the step. In this situation, we can calculate an estimate for the neutral hydrogen density at the end of the step based on implicitly solving

$$\tilde{n}_{\mathrm{HI}}^{i+1} = \tilde{n}_{\mathrm{HI}}^i + [\alpha(1 - \tilde{n}_{\mathrm{HI}}^{i+1})^2 - \beta\tilde{n}_{\mathrm{HI}}^{i+1}(1 - \tilde{n}_{\mathrm{HI}}^{i+1})]n_{\mathrm{H}}\Delta t + \Delta \tilde{n}_\gamma \qquad (4.27)$$

for $\tilde{n}_{\mathrm{HI}}^{i+1}$. If the implied relative change in $\tilde{n}_{\mathrm{HI}}^i$ is again small, we keep the solution.

Otherwise, we first check whether the photon number is very much smaller than the neutral hydrogen number, i.e. whether we have $\tilde{n}_\gamma < 0.01\, \tilde{n}_{\mathrm{HI}}$. If this holds, the photons
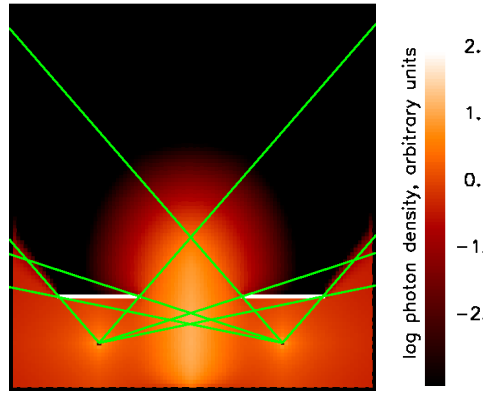
Figure 4.7: *Test (1)*. Radiation field around two point sources and two absorbing obstacles, for our hybrid treatment of point-sources and radiative diffusion. In this example, only the brightest source seen from a given cell was treated explicitly as a point source, while the other radiation was dumped into a background field transported with radiative diffusion.

in the cell cannot possibly ionize a significant fraction of the neutral hydrogen atoms, but the photon abundance itself may still change strongly over the step (for example because almost all of the photons are absorbed). We in this case first compute an estimate of the new photon number at the end of the step, based on the implicit step

$$\tilde{n}_\gamma^{i+1} = \tilde{n}_\gamma^i - c\sigma n_H \tilde{n}_{\mathrm{HI}}^i \tilde{n}_\gamma^{i+1} \, \Delta t. \tag{4.28}$$

With the solution for $\tilde{n}_\gamma^{i+1}$ in hand, we calculate again an implicit solution for the new neutral hydrogen fraction at the end of the step, using equation (4.27). If the predicted relative change in the hydrogen ionization state is small, we keep the solution, otherwise we discard it.

Finally, if both of the two approaches to calculate new values for $\tilde{n}_\gamma^{i+1}$ and $\tilde{n}_{\mathrm{H}}^{i+1}$ at the end of the step have failed, we integrate the rate equations (4.23) and (4.25) essentially exactly over the timestep Δt, using a 4-th order Runge-Kutta-Fehlberg integrator with adaptive step-size control as implemented in the GSL library[1]. We note that this subcycled integration is hence only done in timesteps where the ionization state changes rapidly in time and non-equilibrium effects can become important, which is a very small fraction of all cells, such that our updating scheme remains computationally very efficient.

4.2.6. Photoheating and radiative cooling

To calculate the evolution of the thermal energy, we can now inject the photoheating energy

$$\Delta E_\gamma = (\tilde{n}_\gamma^i - \tilde{n}_\gamma^{i+1}) n_{\mathrm{H}} V \, \epsilon_\gamma \tag{4.29}$$

into the corresponding cell, where V is the volume of the cell under consideration, $(\tilde{n}_\gamma^i - \tilde{n}_\gamma^{i+1}) n_{\mathrm{H}}$ is the number density of photons consumed by ionizing events over the timestep,

---

[1]http://www.gnu.org/software/gsl
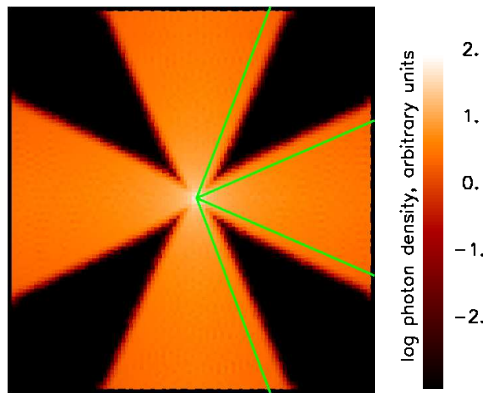
Figure 4.8: *Test (1)*. Illustration of our cone transport scheme, and the accuracy with which it can represent homogeneously illuminated radiation cones. The panel shows a map of the 2D photon density around a single source positioned at the center of the field. Radiation transport was calculated by partitioning the full 2π angle into eight regions of size $\pi/4$ each, with each of the fields transported individually. To show that the cones produce a homogeneous field, the source luminosity was only injected into every second cone and some of the cone boundaries were marked with green lines.

and ϵ_γ gives the average energy absorbed per photoionization event. For our prescribed spectral shape, this injection energy per ionization event is given by the frequency-averaged photon excess energy (Spitzer, 1998)

$$\epsilon_\gamma = \left[\int_{\nu_0}^{\infty} \mathrm{d}\nu \frac{4\pi J_\nu}{h\nu} \sigma_\nu (h\nu - h\nu_0) \right] \times \left[\int_{\nu_0}^{\infty} \mathrm{d}\nu \frac{4\pi J_\nu}{h\nu} \sigma_\nu \right]^{-1} \tag{4.30}$$

above the ionization cut-off ν_0. For many of our test calculations, we assume a black body spectrum with $T_{\mathrm{eff}} = 10^5\,\mathrm{K}$, which leads to $\epsilon_\gamma = 6.4\,\mathrm{eV}$.

The evolution of the thermal energy is then completed by a separate cooling step that accounts for recombination cooling, collisional ionization, excitation cooling, and bremsstrahlung cooling (e.g. Katz et al., 1996). We implement these cooling rates with a combination of an explicit and implicit timestep integrator, where an explicit integration scheme is used as default, but if the temperature change over the step becomes large, the cooling is instead calculated with an unconditionally stable implicit solver.

4.2.7. Time stepping and the reduced speed-of-light approximation

As discussed above, we include the source terms into the time integration of our RT solver by an operator splitting technique, where the source and advection parts are treated separately. This technique can be generalized also to the coupling of hydrodynamics and radiative transfer, by alternatingly evolving the hydrodynamical density field and the radiation field with its associated radiation chemistry. In fact, this is the approach we follow in our radiative transfer implementation in the hydrodynamical AREPO code. As the latter
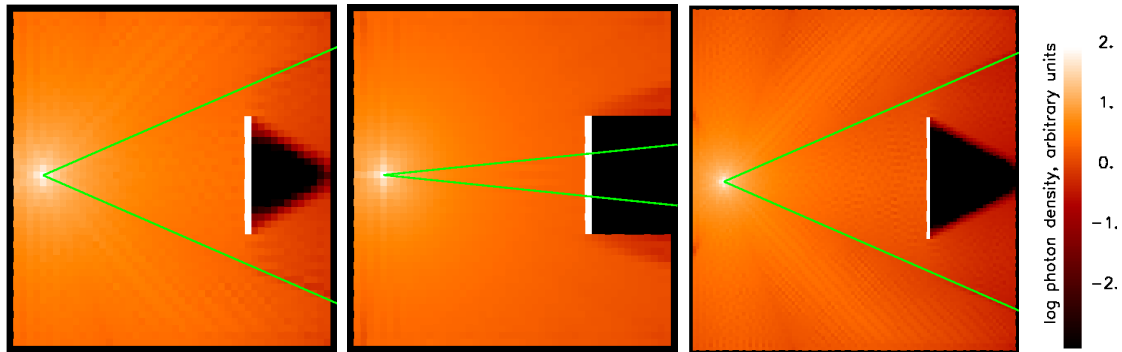
Figure 4.9: *Test (1)*. Maps of the photon density field obtained with our "cone transport" scheme for a point source at coordinates $(0.1, 0.5)$ and an obstacle (shown in white) centered at coordinates $(0.72, 0.5)$. The three panels differ in the mesh resolution used and the angular resolution employed for the radiation transfer. In all panels, the angular size of the cones employed in the angular discretization are shown with green lines. In the left panel, where eight cones are used, the obstacle's opening angle as seen from the source is smaller than the fundamental cone, and therefore no complete shadow is formed. In the middle panel, 32 cones are used instead, such that the obstacle's opening angle is now larger than the angular resolution, allowing a full shadow to be formed. Finally, in the right hand panel, the spatial mesh resolution has been doubled in each dimension compared to the panel on the left, while the number of angular resolution elements has been kept at eight. Again there is no complete shadow formed, as expected, but the boundary of the shadow region behind the obstacle is now more sharply defined.

is a moving-mesh code, we however need to ensure that during the hydrodynamical step the radiation field is left invariant. This can be achieved by appropriate advection terms that compensate for the mesh-motion during the hydrodynamical step.

For the time integration of the radiative source terms, we employ implicit or semi-implicit methods, as described in Section 4.2.5, that are stable even for very large time steps, and in selected situations, adaptive numerical integration of the stiff ordinary differential equations that describe the chemical networks. The latter is essential to accurately account for non-equilibrium effects. As these processes are completely local, this does usually not incur a very significant computational cost, provided the exact integration is only done where really needed. In contrast, the timestepping of the radiation advection step poses more severe computational requirements. This is because this step is based on an explicit time integration scheme, whose timestep needs to obey a Courant criterion of the form

$$\Delta t_{\text{advect}} < C_k \frac{\Delta x\, a}{c}, \tag{4.31}$$

where $0 < C_k < 1$ is the Courant factor, and Δx is taken to the smallest comoving size of a cell in the simulated volume.

In ordinary hydrodynamics, a similar time step constraint is encountered, except that the speed of light is replaced with the speed of sound. Since we are primarily interested in non-relativistic gas dynamics in cosmological structure formation, the speed of light
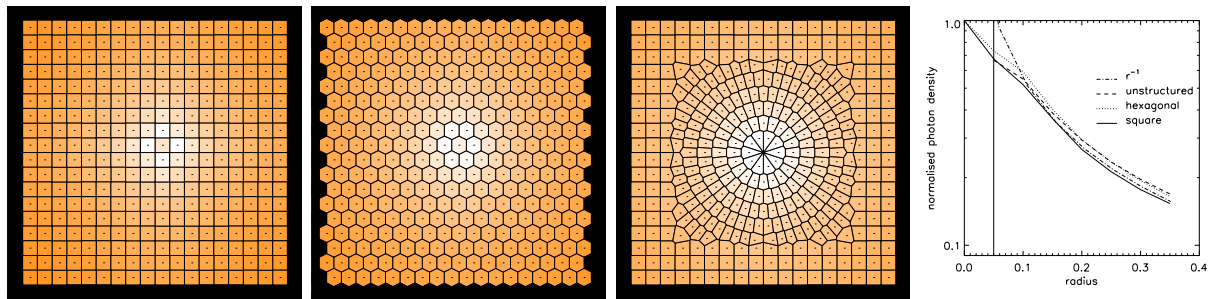
Figure 4.10: *Test (1).* Maps of the photon distribution for 2D simulations with three different cell shapes: Cartesian square, hexagonal and azimuthal/unstructured. The line plot on the right shows the photon intensity profile, overplotted with the expected r^{-1} law. The vertical line indicates the average cell size. Results from all mesh shapes agree well with the analytical prediction (dot-dashed line).

will typically be a factor $\sim 10^2$ to 10^4 larger than the hydrodynamical sound speed. The resulting reduction in the allowed time step size can hence make a simulation prohibitively expensive when the RT is coupled to the hydrodynamics over significant fractions of the Hubble time. However, in many applications of interest this problem can be greatly alleviated by resorting to an artificially reduced speed of light c', which is introduced instead of the physical speed of light both in the transport equation and the ionization equation. As Gnedin & Abel (2001) and Aubert & Teyssier (2008) discuss in detail, this reduced speed-of-light approximation is especially attractive for cosmic reionization problems because it here does not modify the propagation speed of I-fronts, except perhaps in the very near field region around a source directly after it turns on, but this introduces a negligible timing error. In general, the reduced speed-of-light approximation can be expected to yield reasonable accuracy in many radiation hydrodynamic problems as long as c' remains significant larger than the maximum sound speed occurring in the simulation.

4.2.8. Implementation aspects in the moving-mesh code AREPO

We have implemented the different variants of our radiation advection solver in the moving-mesh code AREPO (Springel, 2010). This code treats hydrodynamics with an ordinary finite-volume approach and a second order accurate Godunov scheme, similar to many Eulerian grid codes. However, AREPO works on an unstructured mesh created with a tessellation technique. The particular mesh used is the Voronoi tessellation created by a set of mesh-generating points. Using such a mesh offers a number of advantages compared to traditional grid codes in that its mesh can flow along with the gas. As a result of the induced dynamic mesh motion, AREPO exhibits considerably lower advection errors than ordinary mesh codes, and also avoids the introduction of preferred spatial directions. Also, the cell size automatically and continuously adjusts to the density in a Lagrangian sense, and is hence decreased in regions where typically more resolution is required even without
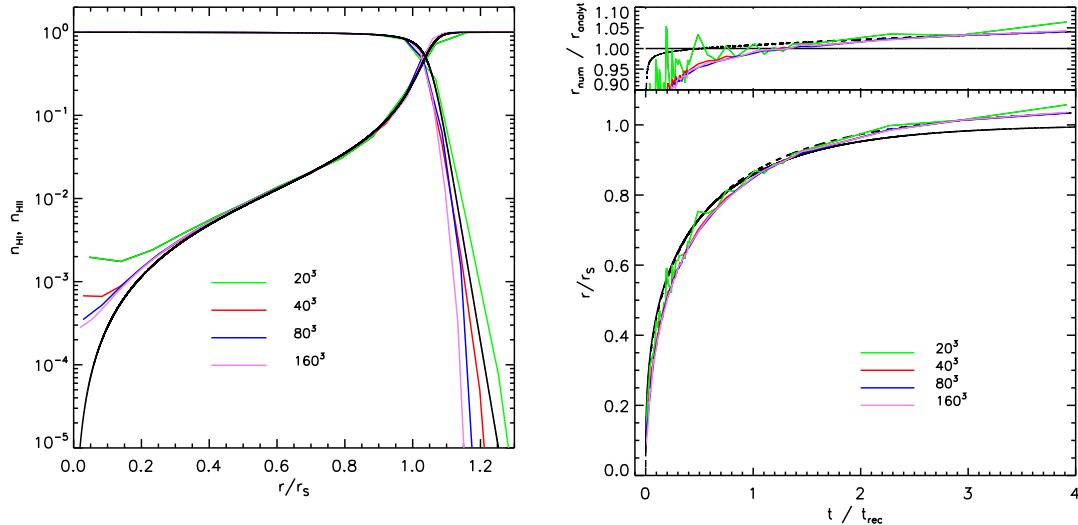
Figure 4.11: *Test (2)*. *Left panel*: Profiles of the neutral and ionized fraction at the end of the ionized bubble expansion test, when the Strömgren radius $r_{S,0}$ has been reached. The black line is the analytic solution based on equation (4.35), while the colored lines are the numerical results for mesh resolutions of 20^3, 40^3, 80^3, and 160^3 cells, as labeled. *Right panel*: Radius of the ionized region as a function of time, in units of the recombination time t_{rec}. The solid black line is the analytic solution from equation (4.35), while the dashed black line gives the simple approximation of equation (4.33). The colored lines give our numerical results for different mesh resolutions. We see that the ionizing front is slower than the theoretical prediction in the beginning of the expansion, as a result of the artificially reduced speed of light adopted here. At late times, the numerical result agrees however very well with the analytical solution.

doing adaptive mesh refinement.

For implementing our RT transfer scheme as described above, we can readily employ the infrastructure and communication algorithms provided by the fully parallelized AREPO code, making it an ideal base for a first demonstration of the method. This in particular applies to the gradient estimation, the spatial reconstruction of the photon intensity fields, and the parallelization for distributed memory computers. A full description of these aspects of our code can hence be found in Springel (2010). We carry out a RT step on every top-level synchronization point of the AREPO code, which means on the longest time step Δt_{max} allowed by the gravitational and hydrodynamical interactions followed by the code. If Δt_{advect} is smaller than the top-level simulation timestep Δt_{max}, the radiation transfer step is calculated in several subcycling steps equal to or smaller than Δt_{advect}, as needed.

Note that these subcycling steps do not require a new construction of the Voronoi mesh, or a new gravity calculation, hence they are in principle quite fast compared to a full step of the hydrodynamic code. However, this advantage can be quickly (over)compensated by the need to carry out multiple flux calculations for each of the angular components of the
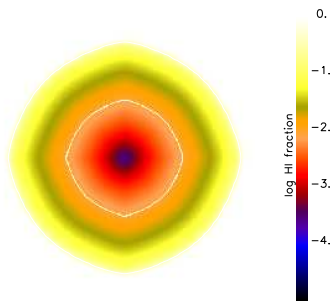
Figure 4.12: *Test (2)*. Map of the neutral fraction in a slice through the center of our Strömgren sphere test (based on our point-source advection scheme), for our highest resolution simulation with 160^3 mesh cells. The white line shows the contour at a neutral fraction of 0.5.

radiation field, and the additional need to do subcycling in time to ensure stability of the explicit time integration used in the advection steps. Furthermore, if a multi-frequency treatment is desired, the cost of the radiative transfer calculations will scale linearly with the number of frequency bins employed, simply because the dominating advection part of the radiative transfer problem needs to be carried out for each frequency independently. The additional storage requirements for a multiple frequency treatment should also not be overlooked, which again scale linearly with the number of frequency bins, likewise with the number of solid-angle bins used in the angular discretization. It is hence clear that multi-frequency radiative transfer at high angular resolution clearly remains expensive with the discretization scheme proposed here. However, the relative cost increase compared to hydrodynamics alone is a constant (and at least for sufficiently interesting problems still affordable) factor that is nearly independent of spatial resolution. This, together with the ability of our scheme to cope with essentially arbitrary source functions, makes it an interesting new technique for cosmological hydrodynamics.

4.3. Basic test problems

4.3.1. Test (1) - Shadows around isolated and multiple point sources

We begin our investigation of the accuracy of our proposed radiative transfer algorithms with isolated point sources in an optically thin medium that includes some regions with absorbing obstacles. This serves both as a verification that an isolated point source produces a radiation field $n_\gamma \propto 1/r^2$ (in 3D, and $n_\gamma \propto 1/r$ in 2D), with sufficiently spherical isophots, and as a test whether the method can cast sharp shadows behind obstacles. The latter is often difficult for RT transfer schemes, especially the ones that are diffusive in character such as the OTVET scheme (e.g. Gnedin & Abel, 2001; Petkova & Springel, 2009).

In Figure 4.6, we show such shadowing tests for three different cases, which for visualization purposes have been done in 2D space. In the left hand panel, we consider the shadow
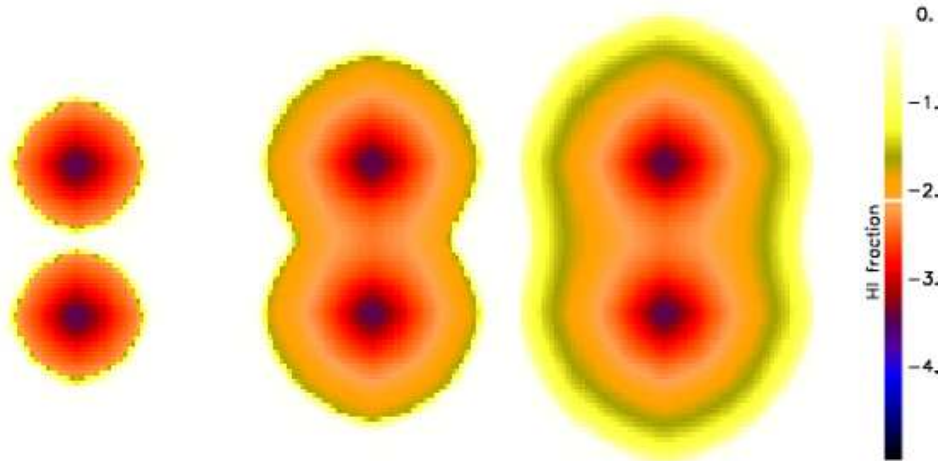
Figure 4.13: *Test (2)*. Neutral fraction in a slice through the center of two nearby sources of equal luminosity that ionize neutral gas. The three panels from left to right show different evolutionary stages. The left panel shows a stage before the ionized spheres overlap ($t = 25\,\mathrm{Myr}$). Here they have exactly the same shape and do not influence each other yet. In the middle panel, the two have begun to overlap ($t = 100\,\mathrm{Myr}$), while in the right panel the final state is shown, where the ionized region becomes time invariant ($t = 500\,\mathrm{Myr}$).

that is produced by an obstacle when it is illuminated by a single source in the middle of the panel. The green lines show the geometric boundaries of the theoretically expected position of the shadow. We see that the obstacle produces a rather sharply defined shadow with only a small radiation leak into the shadowed region due to numerical advection and discretization errors along the shadow boundaries. In the unshadowed regions, the radiation intensity falls of as $\propto 1/r$, as expected.

Equally good results are also obtained when multiple sources are considered in our "linear sum" approach to the total radiation field, where the total photon density is computed as a linear sum of the photon fields from each source, and the transport of each partial field is treated independently. Examples for this are shown in the middle and right panels of Figure 4.6, where two obstacles and one or two sources are used in different configurations. Again, the shadows agree very well with the expected boundaries shown with green lines, with only a small amount of residual diffusion into the shadowed regions. If the spatial mesh resolution is improved, the shadows become progressively sharper still.

We note that the above success essentially holds in this approach for an arbitrary set of absorbing regions, and an arbitrary combination of point sources. It hence provides a general and highly accurate solution to the radiative transfer problem, even though it can certainly get expensive to obtain it, especially for a large number of source. It is important to note however that the radiation fields produced by our scheme are essentially noise-free, which is a drastic improvement compared to results obtained from schemes that rely on Monte-Carlo methods (e.g. Maselli et al., 2003), or on randomized cone transport
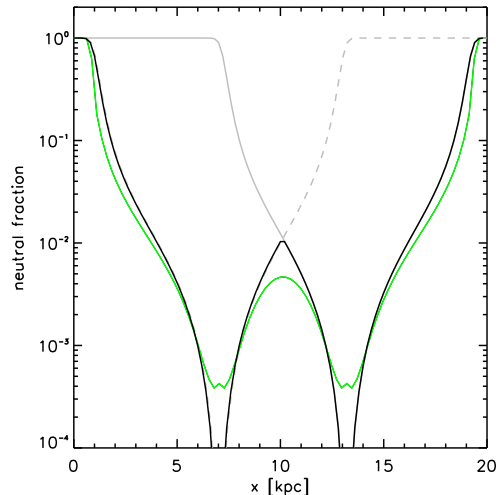
Figure 4.14: *Test (2)*. Neutral fraction along a line passing through the centers of two nearby sources that ionize the background gas. The green line shows the numerical result, whereas the black lines are a simple composite model for the expected structure of the solution based on superposing the analytic solution for each of the sources (gray dashed line for the left source and gray solid line for the right source). This superposition of the individual sources describes the numerical solution reasonably accurately, but we note that it is not the correct solution; the latter can only be obtained numerically for this problem.

(Pawlik & Schaye, 2008).

As we discussed earlier, for many problems in astrophysics the number of sources is too large to make the linear sum approach a viable solution technique. In our first approach to work around this limitation, we only treat the photons from the brightest sources at a given cells as independent point sources in the transport scheme, while all other incoming photons form fainter sources are added to a background radiation field, which is then diffused from cell to cell. In Figure 4.7, we show a (somewhat extreme) example for how this can change the results. We repeat the test shown in the middle panel of Fig. 4.6, which has two sources and two obstacles, but this time we only allow the code to treat the locally brightest $N_{\mathrm{br}} = 1$ sources as explicit point sources, while the rest of the radiation needs to treated with radiative diffusion. As we can see from Figure 4.7, the radiation field near to the two sources is unchanged, as expected, but at the mid-plane, where the sources have equal intensity, half of the flux is dumped into a diffusive reservoir. The diffusion approximation then lets the radiation spread from the mid-plane more slowly, causing an incorrect increase of the radiation intensity there. A second effect is that the shadows behind the obstacles are not sustained as nicely any more, instead they are partially illuminated by the radiative diffusion. It is important to be aware that unlike in the pure transport scheme considered earlier, these errors will not become smaller for an improved mesh resolution, rather, one would simply converge to a wrong solution in this
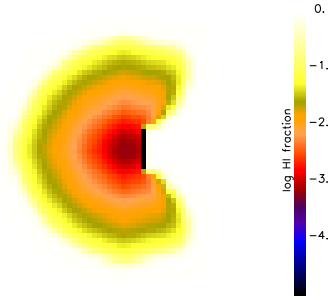
Figure 4.15: *Test (2)*. Map of the neutral fraction in a slice through the center of a Strömgren sphere. Unlike in our previous tests, an absorbing obstacle in the form of an optically thick disk was included as well (shown as a black line). We find that a nice shadow is produced behind the disk, with the inobscured directions developing as in the Strömgren sphere without an obstacle.

case.

The example studied in Fig. 4.7 is deliberately extreme in the sense that $N_{\rm br}$ was kept very low. Much better results can be expected for a sizable value of $N_{\rm br}$, say $5 - 10$, because then the flux that needs to be treated with the diffusion approximation should become locally sub-dominant everywhere. Nevertheless, for general radiation fields and smoothly distributed source functions, we prefer our "cone transport" scheme, which we now begin to evaluate in the context of shadowing.

In Figure 4.8, we illustrate the ability of this transport scheme to produce homogeneously illuminated radiation cones with an opening angle equal to the angular resolution adopted for the scheme. In this example, a single source was placed in the center of a 2D unit square, and angular space has been divided into eight equal sized regions, with the source radiation only injected into four of them, alternating between an "empty" and a "full" cone. The green lines in the plot show some of the geometric boundaries of the angular discretization as seen from the source. We see that the cone transport succeeds in producing a flat intensity profile as a function of angle within every illuminated cone, while at the same time the leaking of radiation into cones that should remain dark as seen from the source is very small. We note that if we let the source inject radiation into two adjacent cones with equal luminosity, the radiation field shows no trace of the angular boundary between the cones, thanks to our use of the total intensity field in calculating the local advection direction for the radiation of each partial field.

An interesting question now arises how this transport scheme deals with obstacles and the problem of shadowing. We illustrate the salient points with a few tests in Figure 4.9. Here, we illuminate an obstacle (shown in white) by a single source in the left part of the simulated 2D space. We vary both the angular and the spatial mesh resolution in order to study how the shadowing performs in the cone transport scheme. In the left panel, we have used 50^2 cell and eight angular regions. The fundamental cone size is shown by the green lines. In this setup, the opening angle of the obstacle as seen from the source is hence smaller than the angular resolution of the RT, making the obstacle "unresolved". In this
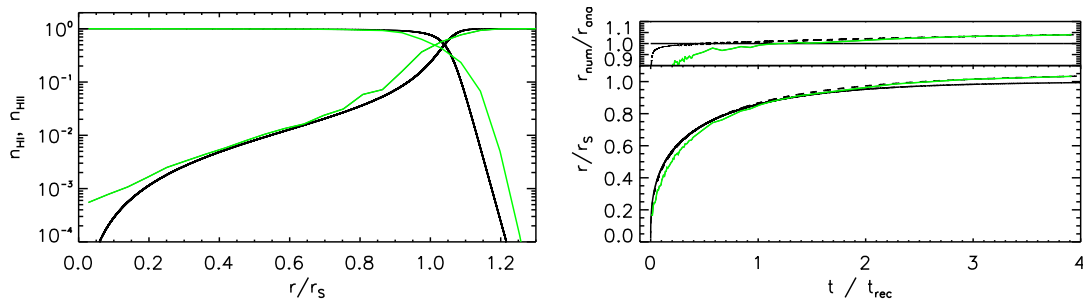
Figure 4.16: *Test (2)*. Strömgren sphere test for our 'cone transport' scheme where the angular space is decomposed into cones of equal solid angle. The panel on top shows the profiles of ionized and neutral fractions (green lines) versus distance from the source, in units of the Strömgren radius $r_{S,0}$ at the end of the expansion at $t = 500\,\mathrm{Myr}$. The analytical solution is given by the solid black line. The bottom panel shows the ionization front radius as a function of time, relative to the Strömgren radius $r_{S,0}$ as a function of time in units of the recombination time t_{rec}. The numerical solution is shown in green and the analytical one in black.

case, the obstacle absorbs the correct amount of radiation expected for its size, but it will not form a correct shadow behind it. Instead, the "downstream region" behind the obstacle will get refilled with photons. As this can happen only by photons transported within the same geometric cone, a partial shadow is formed behind the object, with boundaries that are in principle parallel to the cone boundaries. In the middle panel, we repeat the test with the same spatial mesh resolution, but we have increased the number of cones to 32. In this way the angular size of the obstacle as seen from the source becomes larger than the angular resolution, allowing it to be resolved. As a result, a complete shadow is being formed, but this shadow is in general a bit smaller than the correct geometric shadow, with the difference being filled by a partial shadow, created in the cones that are only partially obscured by the obstacle. Finally, in the right hand panel, we have repeated the test on the left a second time, but now doubling the spatial resolution to 100^2 cells while the angular resolution was kept unchanged. The primary difference this makes is that the borders of the partial shadow that is formed are now more sharply defined compared to the case with lower spatial resolution, as expected.

Finally, we examine how well our transport scheme can cope with different mesh geometries, which naturally arise in simulations with the AREPO code. In Figure 4.10 we show the radiation fields developing around a point source embedded in different mesh geometries: a Cartesian mesh, a hexagonal mesh (which is akin to the mesh geometry developing in AREPO in regions of constant resolution), and an azimuthal/unstructured mesh. For all four cases, we compare the created radiation fields to the expected profile in 2D, obtaining good agreement. This confirms the ability of our approach to work well with the unstructured Voronoi meshes produced by the AREPO code.
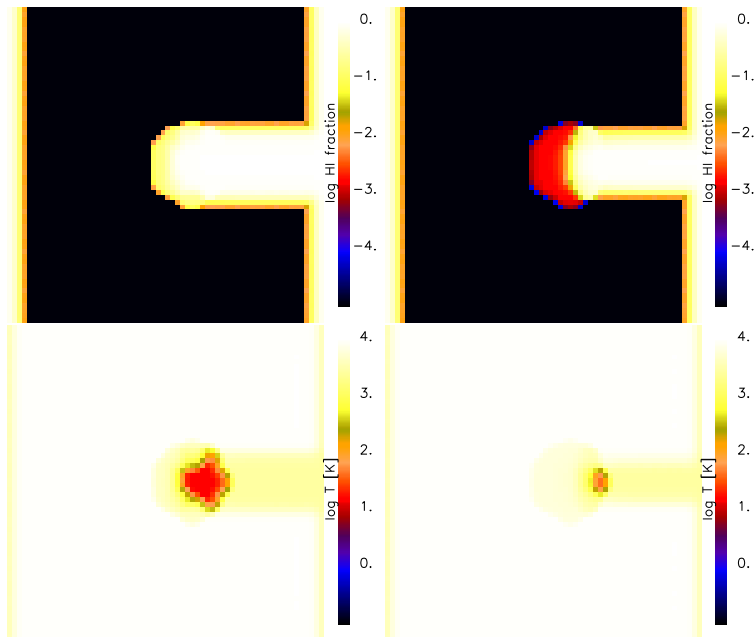
Figure 4.17: *Test (3)*. Maps of neutral fraction (top row) and temperature (bottom row), in a simulation of the interaction of a plane-parallel ionization front with a dense clump. The two columns show our simulation results at two different times, $t = 1\,\mathrm{Myr}$ (left) and $t = 15\,\mathrm{Myr}$ (right). We note that already at the earlier time the background gas has been fully ionized. The I-front gets however stuck in the clump, producing a shadow behind it.

4.3.2. Test (2) - Isothermal ionized sphere expansion

We now turn to a test of our basic radiation advection scheme that involves both sources and sinks. To this end, we perform an ionized sphere expansion test in three dimensions, which is arguably the most fundamental and important test relevant for cosmic reionization codes.

The expansion of an ionization front in a static, homogeneous and isothermal gas is the only problem in radiation hydrodynamics that has a known analytical solution and is therefore indeed the most widely used test for RT codes. We adopt a monochromatic source that steadily emits $\dot{N}_\gamma$ photons with energy $h\nu = 13.6\,\mathrm{eV}$ per second into an initially neutral medium with constant gas density n_H. Then the Strömgren radius at which the ionized sphere around the source reaches its maximum radius is defined as

$$r_{\mathrm{S},0} = \left(\frac{3\dot{N}_\gamma}{4\pi\alpha_\mathrm{B}n_\mathrm{H}^2} \right)^{1/3}, \tag{4.32}$$

where α_B is the recombination coefficient. If we approximate the I-front is infinitely thin, i.e. features a discontinuity in the ionization fraction, then the temporal expansion of the Strömgren radius can be solved analytically in closed form, with the I-front radius $r_{\mathrm{I},0}$
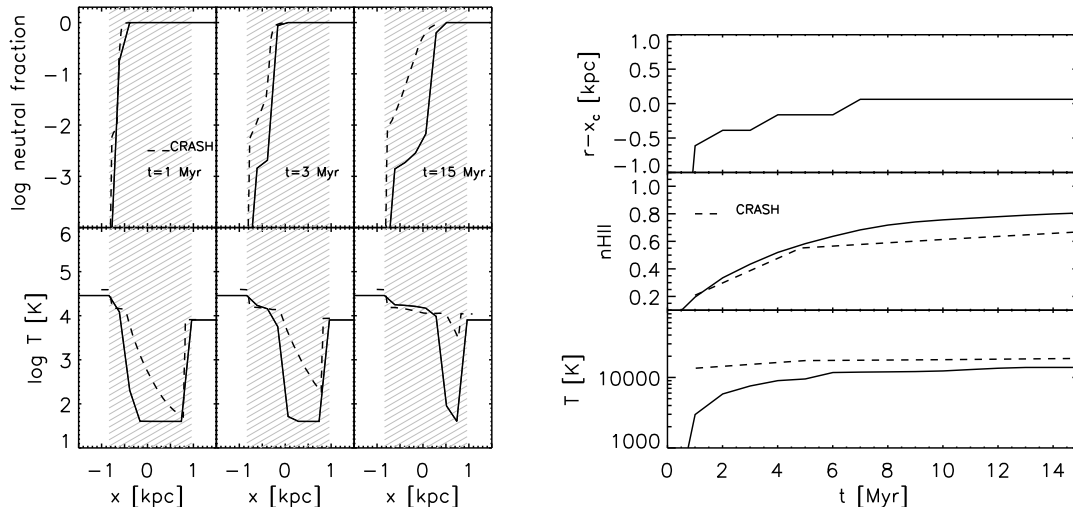
Figure 4.18: *Test (3)*. *Left panel*: Neutral fraction and temperature as a function of distance from the center of the dense clump, at three different times: $t = 1\,\mathrm{Myr}$ (left column), $3\,\mathrm{Myr}$ (middle) and $15\,\mathrm{Myr}$ (right). The shaded area shows the geometric extension of the clump. Results obtained with the code CRASH in the RT code comparison project are also included and shown as dashed lines. *Right panel*: Time evolution of the temperature, neutral fraction, and ionized front (solid lines) in the dense clump that is ionized by an impinging I-front.

given by

$$r_{\mathrm{I},0} = r_{\mathrm{S},0}[1 - \exp(-t/t_{\mathrm{rec}})]^{1/3}, \tag{4.33}$$

where

$$t_{\mathrm{rec}} = \frac{1}{n_{\mathrm{H}}\alpha_{\mathrm{B}}} \tag{4.34}$$

is the recombination time and α_{B} is the recombination coefficient.

More accurately, the neutral and ionized fraction as a function of radius of the Strömgren sphere can be calculated analytically (e.g. Osterbrock & Ferland, 2006) from the equation

$$\frac{\tilde{n}_{\mathrm{HI}}(r)}{4\pi r^2} \int \mathrm{d}\nu\, \dot{N}_\gamma(\nu)\, e^{-\tau_\nu(r)}\, \sigma_\nu \;=\; \tilde{n}_{\mathrm{HII}}^2(r)\, n_{\mathrm{H}}\, \alpha_{\mathrm{B}}, \tag{4.35}$$

where $\tilde{n}_{\mathrm{HI}}$ is the neutral fraction, $\tilde{n}_{\mathrm{HII}}$ is the ionized fraction and

$$\tau_\nu(r) \;=\; n_{\mathrm{H}}\, \sigma_\nu \int_0^r \mathrm{d}r'\, \tilde{n}_{\mathrm{HI}}(r'). \tag{4.36}$$

Moreover, we can analytically solve for the radial profile of the photon density $n_\gamma(r)$, yielding

$$n_\gamma(r) = \frac{1}{c}\frac{\dot{N}_\gamma}{4\pi r^2} \exp\left\{-\int_0^r \kappa(r')\,\mathrm{d}r'\right\}. \tag{4.37}$$
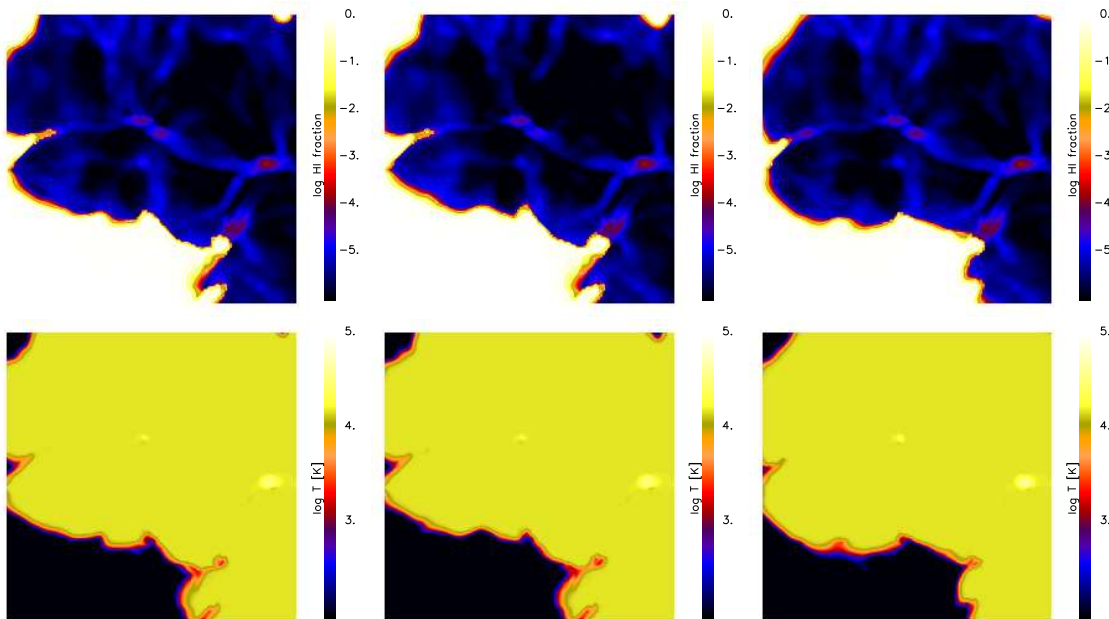
Figure 4.19: *Test (4)*. Maps of the ionized fraction (top row) and temperature (bottom row) in a slice through the middle of the simulation volume at time $t = 0.4$ Myr of our cosmological density field ionization test. In the results shown in the left column, all sources have been treated independently as point sources. In the middle column, only the locally four brightest sources have been considered independently, while the remaining luminosity has been treated with radiation diffusion. Finally, the results in the right column are based on our cone transport algorithm with a division of the full solid angle into 12 cones of equal size, corresponding to the coarsest HEALPIX resolution.

From this we can also obtain the profile of the ionized fraction $\tilde{n}_{\mathrm{HII}}(r)$ as a function of time. We note that the Strömgren radius obtained by direct integration of equation (4.35) differs from the approximate expression (4.32) because it does not approximate the ionized region as a top-hat sphere with constant ionized fraction.

For definiteness, we follow in our tests the expansion of the ionized region around a source that emits $\dot{N}_\gamma = 5 \times 10^{48}\,\mathrm{s}^{-1}$ photons. The surrounding hydrogen number density is set to $n_{\mathrm{H}} = 10^{-3}\,\mathrm{cm}^{-3}$ at a temperature of $T = 10^4\,\mathrm{K}$. At this adopted temperature, the case B recombination coefficient is $\alpha_{\mathrm{B}} = 2.59 \times 10^{-13}\,\mathrm{cm}^3\,\mathrm{s}^{-1}$. Given these parameters, the recombination time is $t_{\mathrm{rec}} = 125.127$ Myr and the expected Strömgren radius is $r_{\mathrm{S},0} = 5.38$ kpc.

In Figure 4.11, we show the profiles of ionized and neutral fraction at the end of the ionized sphere expansion, when the Strömgren radius has been reached. We present results for simulations with four different spatial resolutions, using grids with 20^3, 40^3, 80^3 and 160^3 cells, respectively, using our point-source advection scheme. The results for all resolutions agree well with the analytical solution. The largest errors occur close to the central point source, but with better spatial resolution they become progressively smaller. We also
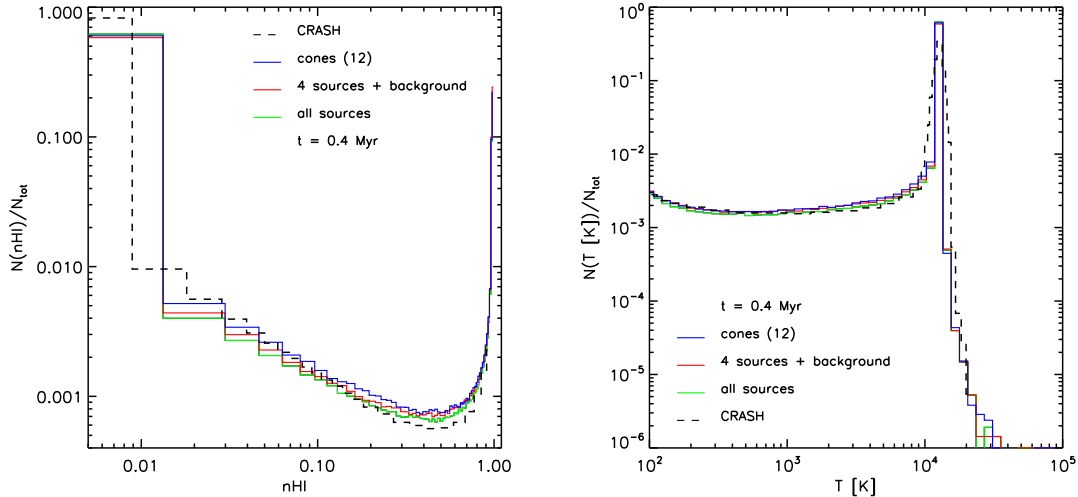
Figure 4.20: *Test (4)*. Distribution functions of the neutral fraction (left panel) and the temperature (right panel) in the simulated cosmological volume at time $t = 0.4\,\mathrm{Myr}$, for three different variants of our radiation transfer scheme, as labeled: (1) all sources are followed in a linearly independent fashion, (2) only the four locally brightest sources are followed as point sources with the rest treated through radiative diffusion, and (3) a cone transport approach based on a division of the unit sphere into 12 cones. For comparison, we also include results obtained with the code CRASH in the RT code comparison project of Iliev et al. (2006a).

show the time evolution of the ionizing front, for the same simulations. The position of the front is determined as the distance from the source at which the ionized fraction equals 0.5. The agreement with the analytical solution is generally good and improves with better resolution. However, in the beginning, the ionization front moves noticeably slower than expected, which is due to our use of the reduced speed of light approximation with $c' = c/1000$. At later times, this initial error becomes unimportant, however, and the numerical solution matches the analytic expectation well. Making the start-up error vanishingly small would be possible, if desired, but requires using $c' = c$.

In Figure 4.12, we show a map of the neutral fraction in a slice through the source plane for the resolution 160^3. We notice that the isophotal shapes exhibit small departures from a perfectly spherical shape, which originate in spatial discretization errors close to the source. In fact, these deviations depend on the geometry of the source cell itself. For a hexagonal mesh structure as it occurs for a regularized Voronoi mesh in 2D dimensions, the errors are noticeably smaller than for the Cartesian mesh employed here. Higher spatial resolution alone will normally not be able to decrease the deviations to arbitrarily small levels, but spreading the point source over multiple cells (effectively resolving the source geometry) can make the isophots perfectly round if desired. We note that our cone transport scheme also does a good job in producing round isophots, even when a single cell is used as source.

As a simple variant of the isolated source case, we have also considered the evolution of
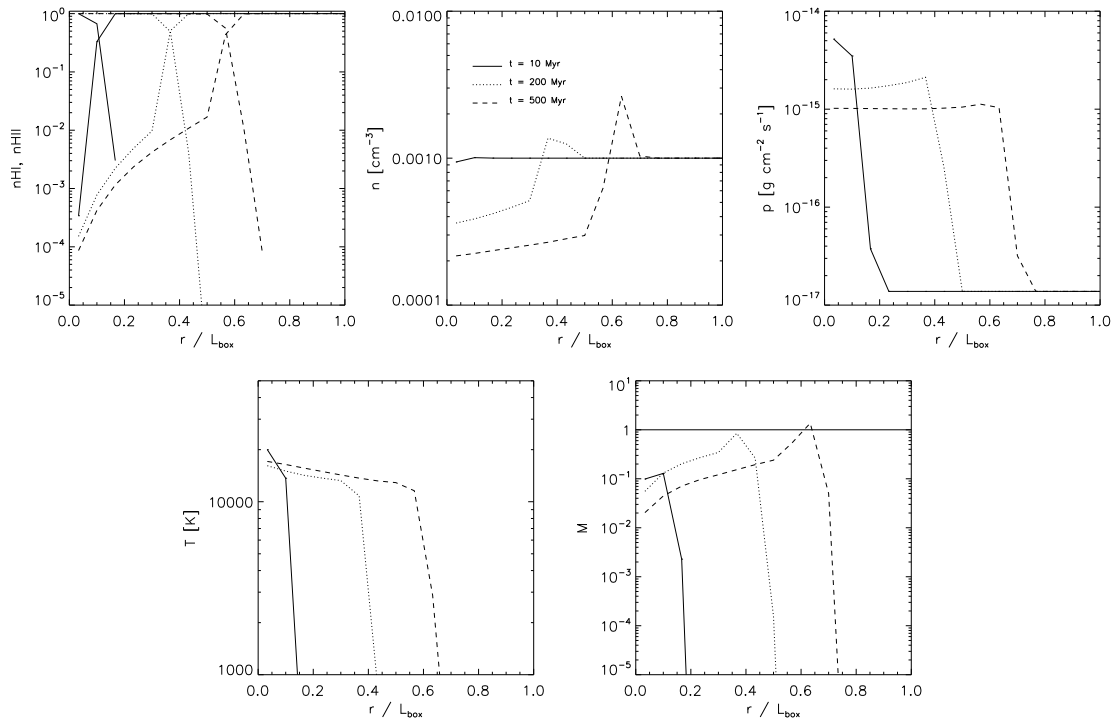
Figure 4.21: *Test (5).* Profiles of ionized fraction, hydrogen number density, pressure, temperature, and mach number at different times for a hydrodynamically coupled Strömgren sphere test. The distance from the source is normalized by the box size $L_{\mathrm{box}} = 15 \, \mathrm{kpc}$. The three lines in each plot correspond to the times $t = 10 \, \mathrm{Myr}$ (solid), $t = 200 \, \mathrm{Myr}$ (dashed), and $t = 500 \, \mathrm{Myr}$ (dotted).

the ionized regions around two sources that are $4 \, \mathrm{kpc}$ apart, using our multiple point-source scheme. The density of the gas and the luminosity of each source are the same as in the previous test. In Figure 4.13, we show maps of the neutral fraction in a slice through the source at three different times: $t = 25 \, \mathrm{Myr}$ (left), $t = 100 \, \mathrm{Myr}$ (middle), and $t = 500 \, \mathrm{Myr}$ (right). An important point of this test is that the proximity of the sources does not affect the shape of the ionized regions at all until they begin to overlap. This is very different in the OTVET scheme, for example, where the early expansion is distorted because the Eddington tensor estimates already "feel" nearby sources even though they may still be completely hidden in their own ionization bubbles. In Figure 4.14, we show the neutral fraction along a line passing through both sources at the final time. A simple model for the expected neutral fraction based on the superposition of the analytic single source solution is shown in black, while the numerical solution is shown in green. While the superposition model does a reasonably good job in describing the numerical solution, we note that the latter is showing important differences, for example for the radiation intensity between the sources. Our method allows an accurate calculation of this quantity, and similarly for more complicated setups.
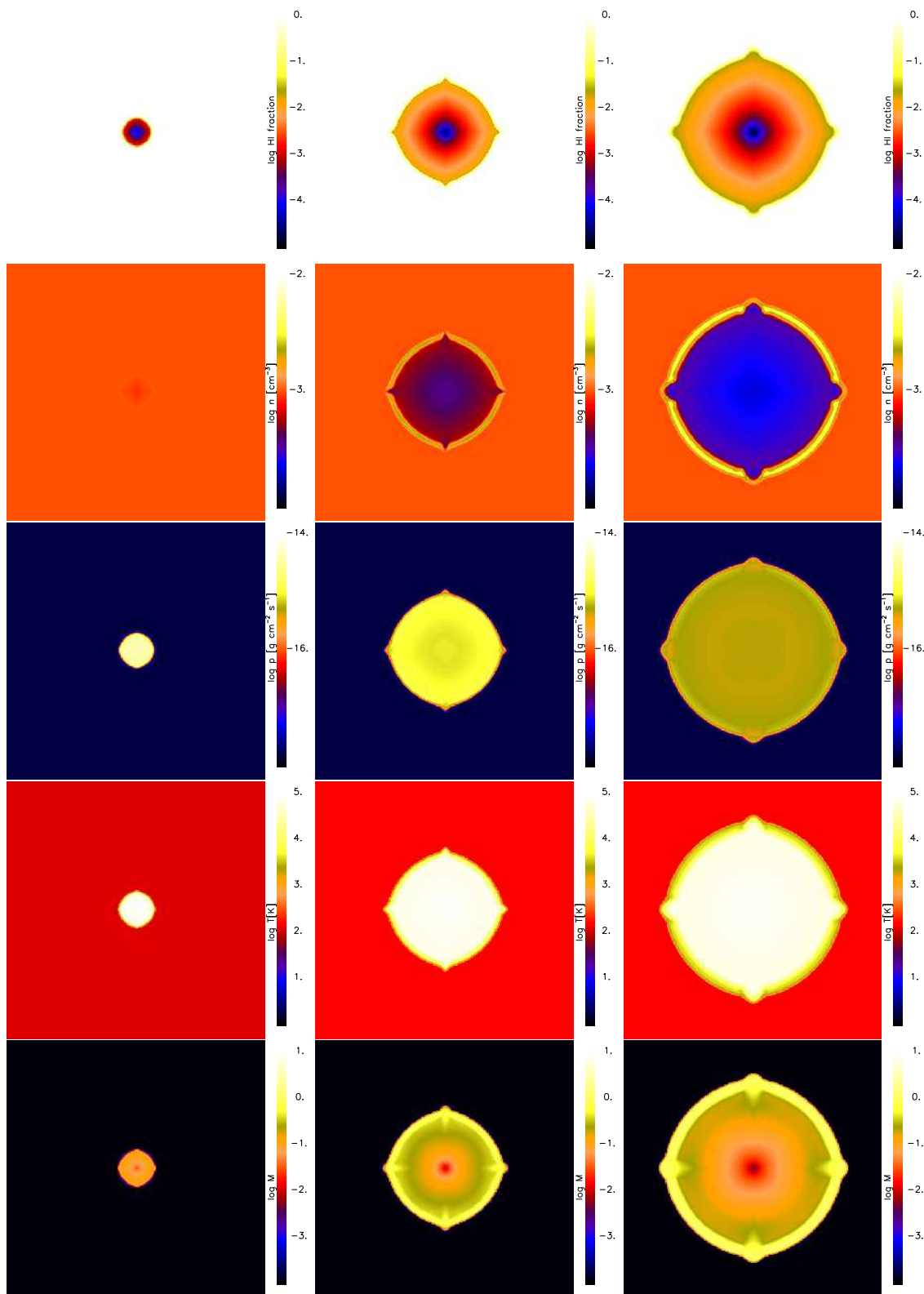
Figure 4.22: *Test (5)*. Slices through the middle of the simulated volume, showing the neutral fraction, hydrogen number density, pressure, temperature and mach number of the gas at three different times: $t = 10\,\mathrm{Myr}$ (left column), $t = 200\,\mathrm{Myr}$ (middle column), $t = 10\,\mathrm{Myr}$ (right column).
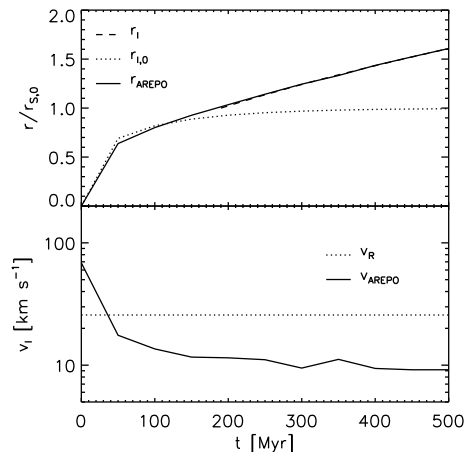
Figure 4.23: *Test (5).* Evolution of the position of the ionizing front in a hydrodynamically coupled Strömgren sphere test. The distance is expressed in terms of the Strömgren radius $r_{S,0}$ for the case of a static density field. The dotted line shows the analytic solution for the time evolution in the static density case, while the dashed line gives the solution for the dynamic density case. The latter is well reproduced by our numerical AREPO calculation. In the bottom panel, we show the speed of the ionization front. In the first 40 Myr of the expansion, the front moves with a speed higher than the R-critical velocity (indicated by a dotted line).

In Figure 4.15 we show a further map of the neutral fraction in a slice through the source plane in a simple single-source Strömgren test. However, in this test we included an obstacle in the form of an optically-thick three dimensional plate, located 2 kpc from the source (shown in black in the figure). The setup is meant to test shadowing in 3D for a problem with non-trivial source function, and is designed to match the parameters of an equivalent test in Pawlik & Schaye (2008). We can see that our obstacle produces a clear shadow that remains fully neutral, as expected. Comparing our result to those of Pawlik & Schaye (2008, see their Fig. 10), we find good qualitative agreement but much reduced numerical noise.

Finally, we check whether using the cone transport scheme described in Section 4.2.4 is equally well capable of accurately solving the Strömgren sphere problem. To this end we have repeated our standard setup for the ionized sphere expansion of a single source, but this time employing direct discretization of angular space using 12 cones for the full 4π solid angle, and a spatial mesh resolution of 40^3. In the top and bottom panels of Figure 4.16 we show the profiles of ionized and neutral fraction at the end of the ionized sphere expansion, and the temporal evolution of the ionizing front, respectively. The numerical results agree well with the analytical solutions, with an overall accuracy that is comparable to that of our point source treatment.

4.3.3. Test (3) - Ionizing front trapping in a dense clump

In our next test, we study the behavior of the code in a more challenging setting taken from the RT code comparison study of Iliev et al. (2006a). A plane-parallel front of ionizing radiation is incident on a dense, cold clump. The I-front penetrates the clump, ionizes it and heats it up. Eventually, the I-front gets trapped half-way through the clump, and as the it is stopped inside the obstacle, a shadow is produced behind the clump.

Our set-up of this test problem is as follows. We simulate a plane-parallel I-front with flux $F_\gamma = 10^6\,\mathrm{photons\,s^{-1}\,cm^{-2}}$ that is incident on a dense clump, located $5\,\mathrm{kpc}$ away from the edge of the simulation domain. The ambient background gas has density $n_\mathrm{H} = 2 \times 10^{-4}\,\mathrm{cm^{-3}}$ and temperature $T = 8000\,\mathrm{K}$. The radius of the clump is $r_\mathrm{clump} = 0.8\,\mathrm{kpc}$, with a density of $n_\mathrm{H}^\mathrm{clump} = 200\,n_\mathrm{H}$, and a temperature $T_\mathrm{clump} = 40\,\mathrm{K}$. We note that in this test, following Iliev et al. (2006a), the gas is not allowed to move due to pressure or gravitational forces, hence only radiative transfer is tested. The system is evolved for a period of $15\,\mathrm{Myr}$ with a resolution of 40^3 cells. In Figure 4.17, we show the neutral fraction and the temperature of the system in slices through the center of the clump at times $t = 1\,\mathrm{Myr}$, and $15\,\mathrm{Myr}$. The I-front approaches from the left, moving to the right. At time $t = 1\,\mathrm{Myr}$, already the whole box has been swept up by the ionizing photons, with the clump producing a clear shadow in the downstream direction on the right hand side of the clump. As time advances further, the clump becomes more ionized and continues to heat up, but the shadow is preserved throughout the simulated time span without being filled in by diffusion.

In the left panel of Figure 4.18, we show the temperature and neutral fraction as a function of distance from the geometric clump center. The results are compared to those obtained in the comparison study of Iliev et al. (2006a) for the Monte-Carlos transfer code CRASH. The position and shape of the ionizing front agree well with the results from the CRASH code, both at times $t = 1\,\mathrm{Myr}$ and $15\,\mathrm{Myr}$. The temperature profile shows, however, some differences. This discrepancy can be traced back to inaccuracies in CRASH, where lower energy photons penetrate into the gas ahead of the ionizing front and heat it there.

Finally, in the right panel of Figure 4.18 we show the time evolution of the temperature, ionized fraction and position of the I-front in the clump, compared to the results obtained with CRASH. The clump is 60% ionized at the end, its average temperature increases to several $10^4\mathrm{K}$ and the I-front becomes trapped around the geometric center of the clump, which is all in good agreement with the CRASH results. We hence conclude that our RT scheme yields results of good accuracy for this test, which are comparable in accuracy to those obtained with expensive yet accurate Monte-Carlo treatments.

4.3.4. Test (4) - Ionization of a static cosmological density field

In our most demanding test of pure RT we follow hydrogen ionization in a realistic cosmo-logical density field, which is taken to be static for simplicity. Again, in order to be able to compare our results with those of the cosmological RT comparison project (Iliev et al.,

2006a) we use the same density field, the same cosmological box parameters, and assign sources in the same way. The test is based on a cosmological density field in a periodic box with size $0.5 \, h^{-1}$comoving Mpc that resulted from the evolution of a standard ΛCDM model with the cosmological parameters $\Omega_0 = 0.27$, $\Omega_b = 0.043$, and $h = 0.7$. The gas density field at redshift $z = 9$, represented by 128^3 cells is considered for further analysis.

The source distribution is determined by finding halos within the simulation box with a Friend-Of-Friends (FOF) algorithm and then assigning sources to the 16 most massive groups. The photon luminosity of these sources is taken to be

$$\dot{N}_\gamma = f_\gamma \frac{M\Omega_b}{\Omega_0 m_p t_s}, \tag{4.38}$$

where M is the total halo mass, $t_s = 3\,\mathrm{Myr}$ is the assumed lifetime of each source, m_p is the proton mass, and $f_\gamma = 250$ is the number of emitted photons per atom during the lifetime of the source. For simplicity we also set the initial temperature of the gas to $100\,\mathrm{K}$ throughout the whole box.

In Figure 4.19, we show the neutral fraction and the temperature in slices through the center of the simulated volume, at the final evolution time of $t = 0.4\,\mathrm{Myr}$. We have calculated the radiation transfer in three different ways, corresponding to the three variants of the radiation advection approach proposed in this chapter. In the left panel, we show the results if all sources are treated as linearly independent point sources. The middle panel shows the result when only the $N_{br} = 4$ brightest sources seen from a given point are treated as point sources, while the remaining luminosity is fed to a background radiation field which is treated with radiative diffusion. Finally, the right hand panel gives the result when angular discretization with 12 HEALPIX cones for the full solid angle is applied.

Visually, based on Fig. 4.19, all three results agree very well with each other. However, there are some small differences in the structure of the ionized regions and in the shape of the I-fronts. For a better quantitative comparison we show in the top panel of Figure 4.20 the volume filling function of the neutral fractions for all three simulation methods, where a comparison with CRASH results from the RT code comparison study (Iliev et al., 2006a) is also included. Our results agree very well with the CRASH data, and we note that there are also no substantial differences between the three different approaches for dealing with multiple sources in our radiation advection scheme. The same conclusion is also reached from a comparison of the volume distribution function of the temperature, which is shown in the bottom panel of Figure 4.20. We note that these results are considerably better than those we obtained for the OTVET scheme implemented in the SPH code GADGET (Petkova & Springel, 2009).

4.3.5. Test (5) - Ionized sphere expansion in a dynamic density field

As our final test, we again follow the expansion of an ionized sphere in an initially homogeneous and isothermal medium, similar to Section 4.3.2, but this time we allow the gas to be heated up by the photons and to expand due to the raised pressure. This is hence a radiation hydrodynamics test where both RT and hydrodynamics are followed. We design
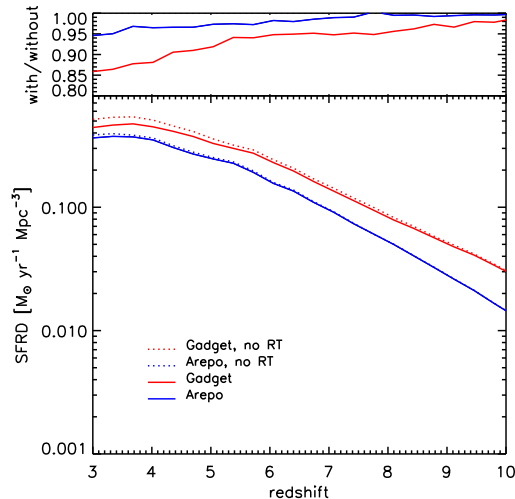
Figure 4.24: Star formation density as a function of redshift. GADGET produces more stars than AREPO during the whole time evolution. In both codes the SFR density is lower when reionization is included. The change for GADGET is greater - approximately 15% and for AREPO - around 5%.

our test similar to the set-up studied in Iliev et al. (2009). The source is at the center of the simulation domain and emits at a luminosity of $\dot{N}_\gamma = 5 \times 10^{48} \, \mathrm{s}^{-1}$. The surrounding hydrogen number density is $n_\mathrm{H} = 10^{-3} \, \mathrm{cm}^{-3}$ at an initial temperature of $T = 10^2 \, \mathrm{K}$. The simulated box is $30 \, \mathrm{kpc}$ on a side, and is resolved with 160^3 cells. We evolve the system for $500 \, \mathrm{Myr}$.

There are two critical gas velocities defined for such a set up (Spitzer, 1978): the R-critical velocity $v_\mathrm{R} = 2c_\mathrm{s}^b$ and the D-critical velocity $v_\mathrm{D} = c_\mathrm{s}^b - \sqrt{(c_\mathrm{s}^b)^2 - (c_\mathrm{s}^a)^2}$, where c_s^a and c_s^b are the isothermal sound speeds ahead and behind the I-front, respectively. If we assume the ionized gas has temperature $10^4 \, \mathrm{K}$ and the neutral gas $10^2 \, \mathrm{K}$, than we obtain $v_\mathrm{R} \approx 25.70 \, \mathrm{km \, s}^{-1}$ and $v_\mathrm{D} \approx 0.03 \, \mathrm{km \, s}^{-1}$. The I-front is called D-type when its speed is smaller than the D-critical speed $v_\mathrm{I} \leq v_\mathrm{D}$. In this case it is subsonic with respect to the neutral gas, which expands as the I-front passes through it. When $v_\mathrm{I} \geq v_\mathrm{R}$, the I-front is called R-type. It is supersonic with respect to the neutral gas ahead, and the gas does not expand as the I-front passes trough it. When $v_\mathrm{D} < v_\mathrm{I} < v_\mathrm{R}$, there is a hydrodynamic shock wave in front of the I-front. The position of the I-front in this stage is given by (Spitzer, 1978)

$$r_\mathrm{I} = r_{\mathrm{S},0} \left(1 + \frac{7c_\mathrm{s}t}{4r_{\mathrm{S},0}}\right), \tag{4.39}$$

where c_s is the sound speed of the ionized gas and $r_{\mathrm{S},0}$ is the Strömgren radius given by equation (4.32).

We evolve our test setup for $500 \, \mathrm{Myr}$ and analyze the results at three different times
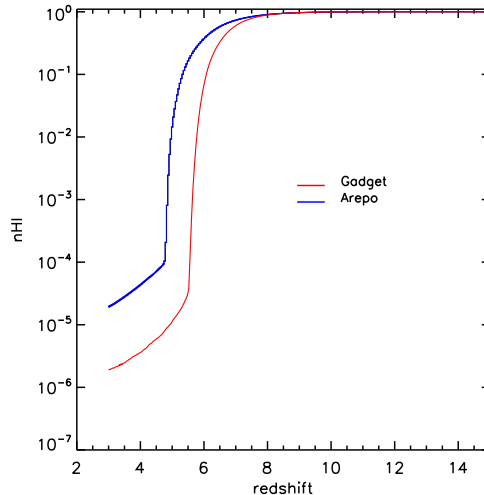
Figure 4.25: Neutral hydrogen fraction evolution as a function of redshift. Reionization in the AREPO simulation occurs later than in the GADGET one. The volume averaged neutral fraction is also several orders of magnitude higher.

equal to $t = 10$, 200 and 500 Myr. Figure 4.21 shows the time evolution of the profiles of the ionized fraction, hydrogen number density, pressure, temperature, and mach number profiles. At time $t = 10$ Myr, the gas expands at subsonic speed. The pressure inside the ionized bubble is very high as the density is still relatively close to 10^{-3} cm^{-3} and the temperature is several 10^4 K. At later times, $t = 200$ Myr, there is a shock developing ahead of the ionizing front. The gas in this pseudo shock region is compressed, leading to densities higher than 10^{-3} cm^{-3} and an increased pressure. At time $t = 500$ Myr, the dynamic situation of the gas is similar, as there is still a shock ahead of the ionizing front, but the pressure in the ionized bubble has dropped significantly due to the lowered density of the gas. For better spatial interpretation of the quantities, refer to Figure 4.22.

In Figure 4.23, we show the evolution of the radius of the I-front. In the first 40 Myr, the ionizing front moves with a speed larger than the R-critical velocity: $v_I > v_R$. Its evolution corresponds to that of an I-front in a static density field, and the position of the front follows the analytical prediction from equation (4.33). The gas does not expand significantly in this stage. As the speed of the I-front drops below the R-critical velocity, a shock develops ahead of it and the gas gets compressed in these regions. Here the position of the front evolves according to equation (4.39).

In general, our results for this test agree well with the other codes that have been tested by Iliev et al. (2009). We find the best agreement with the ENZO-RT results from the RT comparison study, which is probably due to the specific monochromatic nature of our code.
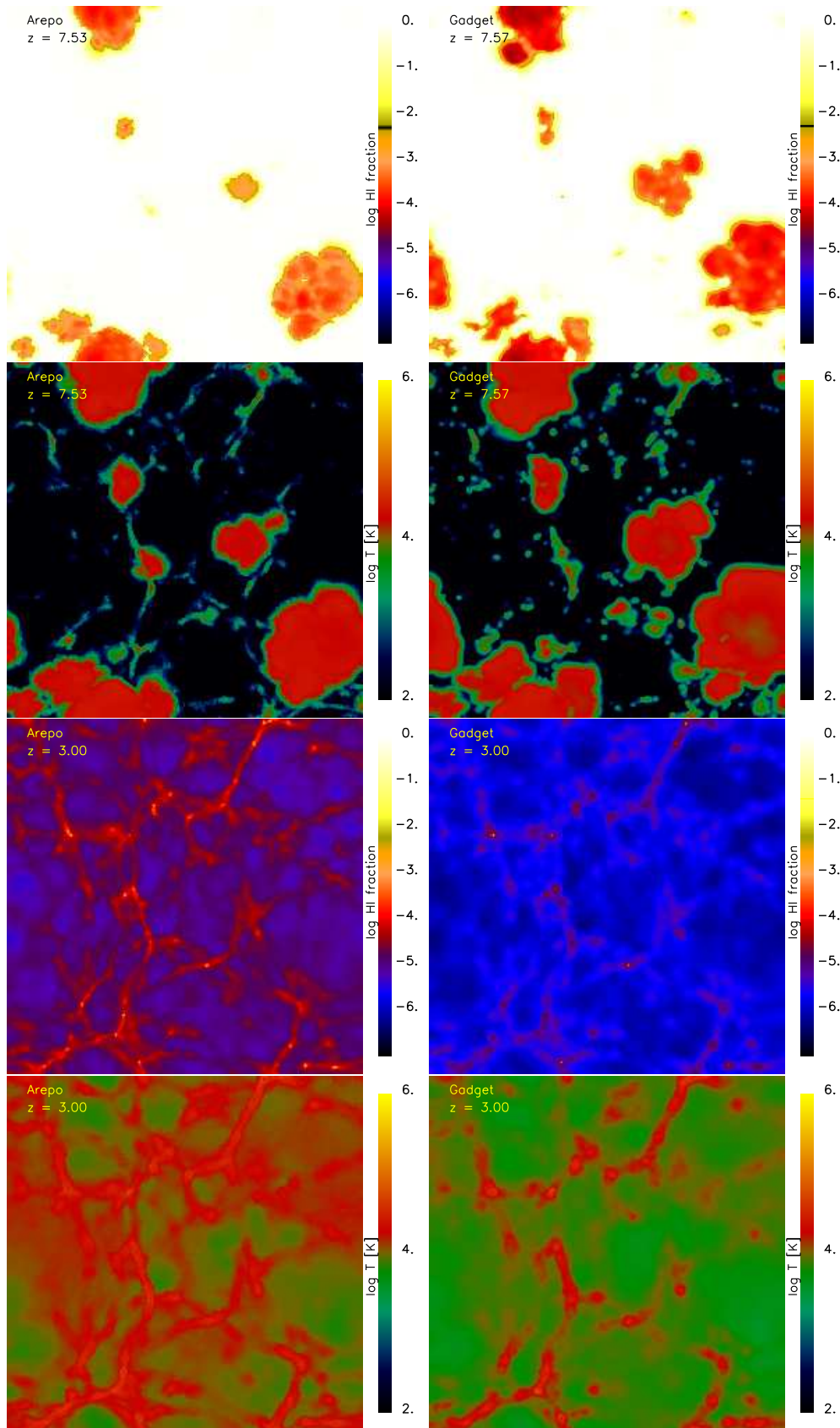
Figure 4.26: Slices of the neutral hydrogen fraction and temperature through the middle of the simulated volume at redshift $z = 7.6$ (top two rows) and $z = 3$ (bottom two rows).
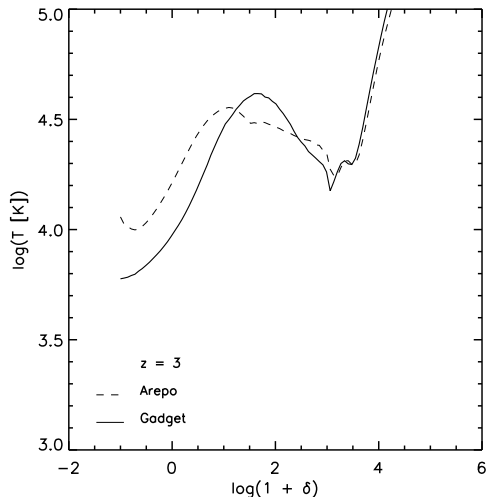
Figure 4.27: Median gas temperature as a function of overdensity in AREPO (dashed) and GADGET (solid) at redshift $z = 3$. AREPO produces higher temperatures at low redshift.

4.4. Hydrogen reionization

In this section we present the results of a self-consistent hydrogen reionization simulation with our novel implementation of radiative transfer in AREPO. We compare our results to a simulation with the same initial conditions and properties, carried out by the code GADGET with a treatment of RT that we have discussed in the first two chapters of this thesis.

4.4.1. Simulation initial conditions

Our simulations assume a ΛCDM universe with cosmological parameters $\Omega_0 = 0.27$, $\Omega_\Lambda = 0.73$, $\Omega_b = 0.044$, $h = 0.7$ and $\sigma_8 = 0.9$ and the same initial conditions as in Chapter 3. The RT is treated using the cone transport scheme, where 12 cones were chosen. In order to have sufficiently high mass resolution, we follow a comparatively small region in a periodic box of comoving size $L_{\text{box}} = 10h^{-1}\,$Mpc on a side. There are 2×128^3 dark matter and gas particles, giving a mass resolution of $3.04 \times 10^7\,h^{-1}$M$_\odot$ and $5.29 \times 10^6\,h^{-1}$M$_\odot$ in dark matter and gas, respectively. The gravitational softening in GADGET was chosen as $1/35$ of the mean particle spacing, corresponding to $\epsilon = 2.23\,h^{-1}$kpc. In order to save computational time, the runs were restarted from $z = 20$, such that the higher redshift evolution did not have to be repeated. We chose a parameter set of 'escape fraction' $\eta = 0.1$ and heating efficiency $\tilde{\epsilon} = 30\,$eV. Star formation in the dense, cold gas is modeled in a sub-resolution fashion (Springel & Hernquist, 2003a). We adopt an ionizing source luminosity of $\dot{N}_{\text{SFR}} = 10^{53}\,$photons M$_\odot^{-1}$ yr (Madau et al., 1999), which relates the number of emitted photons to the star formation rate in units of M$_\odot$yr^{-1}. Stellar winds are *not* part of the
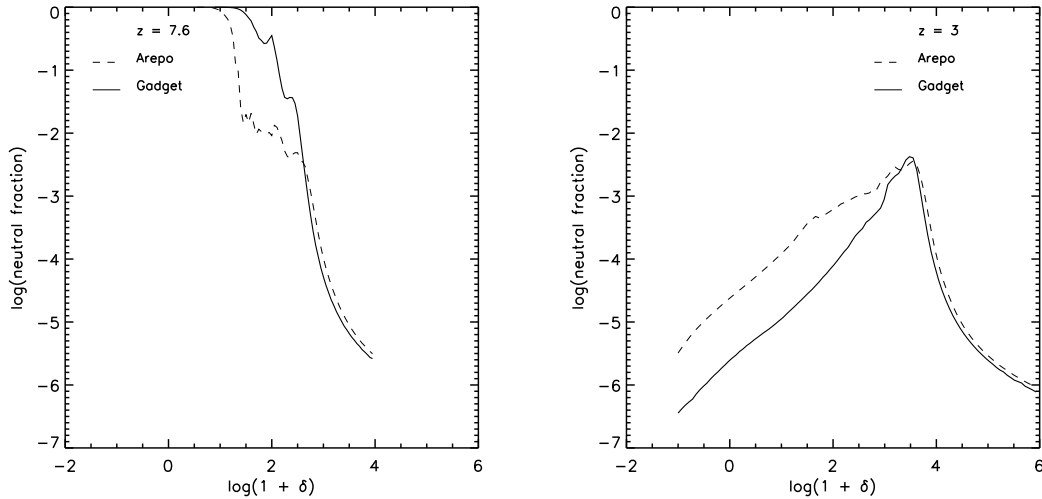
Figure 4.28: Median neutral fraction as a function of overdensity in AREPO (dashed) and GAD-GET (solid) at redshift $z = 7.6$ (left) and $z = 3$ (right). In the beginning of reionization, both codes show similar neutral fraction distribution, where high density regions get ionized first. At redshift $z = 3$, the neutral fraction is directly proportional to the overdensity, except at star forming densities. The low density gas in AREPO is less ionized.

calculations since the AREPO code is still in a development stage, where such treatment is not yet implemented. Even though the treatment of stellar winds is already included in GADGET and we have used is before, we do not adopt it here in order to ensure consistent comparison between the two codes.

4.4.2. Star formation rate density and neutral fraction evolution

Since both codes use the same sub-resolution model for star formation, we expect that the redshift evolution of the SFR density is similar in the simulations. However, in Figure 4.24 we show that there is a difference between the two codes for all redshift and GADGET produces systematically more stars than AREPO in this scenario. We expect that already this difference in the simulation properties will result in some differences in the reionization histories.

In both simulations the global SFR density decreases when photoheating during reionization is included in the simulations. As the gas gets heated up it can escape the deep potential wells of the high density regions, leaving them with less gas to convert to stars. The effect is larger for GADGET, where the decrease reaches $\sim 20\%$ at redshift $z = 3$, versus $\sim 5\%$ for AREPO.

The extent to which the SFR density is inhibited is different from our previous findings in Chapter 3, where a more significant decrease is reported. This suggests that stellar winds are very important in effectively distributing hot gas and therefore modulating star
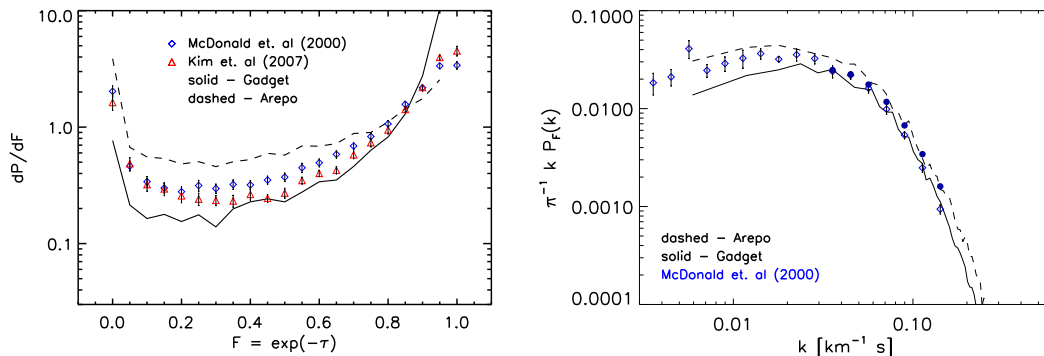
Figure 4.29: Lyman-α flux probability (left) and power spectrum (right) in both simulations, compared with observations from McDonald et al. (2000) and Kim et al. (2007). Both AREPO and GADGET results fall outside of the errors of the observations. However, both simulations recover the given trend, indicating that they both represent reionization to some extent.

formation, an effect already found by Pawlik & Schaye (2009). Without winds photoheated gas tends to linger in dense regions and cool down more efficiently, thus being subject to star formation. When winds are present, the photoheated gas is expelled from high density regions more efficiently and has more time to cool down, resulting in a reduction of the global star formation rate.

The volume-averaged neutral hydrogen fraction evolution differs substantially between the two codes. In AREPO, the universe is reionized at lower redshift $z \sim 5$, in comparison to $z \sim 6$ in GADGET. This difference is most likely primarily due to the SFR densities, mentioned in the previous section. The lower SFR in AREPO results in a lower total number of photons available for ionizing the hydrogen atoms and leads to a delay in the reionization. In Figure 4.25, we show the time evolution of the neutral fraction. In both cases, the epoch of reionization has a similar redshift duration, $\Delta z \sim 1.1$, where we have computed Δz as

$$\Delta z = z(n_{\mathrm{HI}} = 0.5) - z(n_{\mathrm{HI}} = 10^{-3}). \tag{4.40}$$

However, in physical units, reionization in AREPO takes more time. One reason for this extended process might be that at lower redshifts structures are further apart and therefore it takes more time for photons to travel to the ionization sites and the overlap phase, at the end stages of reionization, is prolonged. Another reason might be the ability of the scheme to produce accurate shadows, which is absent in GADGET. In this case, some regions are more effectively shielded from the photons and are ionized at later times.

4.4.3. Temperature and ionization states

We also compare visually the ionization and temperature states of the gas in both simulations at two different redshift $z = 7.6$ – before reionization, and $z = 3$ – after reionization is completed. The maps are shown in Figure 4.26. The morphology and structure of the
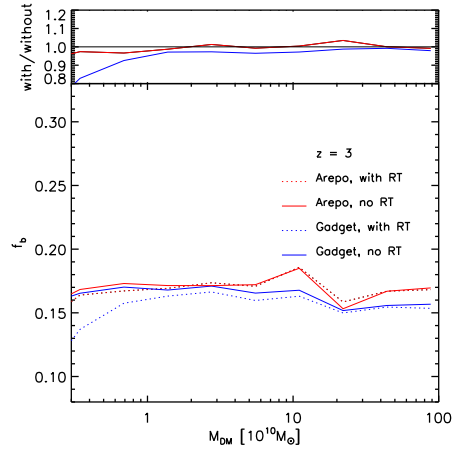
Figure 4.30: Baryon fraction as a function of DM halo mass. Results are compared for AREPO and GADGET for simulations both with and without radiative transfer. Since both simulations are without stellar winds, the baryon fraction is around the cosmological value $f_b = 0.18$. When reionization is included gas and stellar content in low mass DM halos is decreased. The change in AREPO is insignificant - around 1%, compared to the change in GADGET - around 20%.

ionized regions agree well in the simulations – they are in the same places and have similar shapes. There are some differences in the level of ionization of the regions and at later times, at redshift $z = 3$, it is clear that in GADGET the gas is on average more highly ionized, as we have discussed in the previous section. In both simulations filaments are less ionized than the lower density gas.

The temperature maps also show differences in the internal structure of the ionized regions. Although in both simulations ionized gas is heated above 10^4 K, the cooling efficiency in GADGET appears to be higher and the gas cools below 10^4 K in some regions. This is also evident in comparing the median temperature of the gas at different overdensities for the two simulations (Figure 4.27). AREPO produces higher temperature gas at low overdensities and lower temperature gas at high overdensities, compared to GADGET. This distribution of temperatures suggests that GADGET is more efficient in cooling the ionized gas at low overdensities or, alternatively, that AREPO is more efficient in photoheating the it. It is interesting to note that despite the lower temperature, low density gas is more ionized in GADGET than in AREPO, as shown in Figure 4.28.

At higher redshift, as reionization begins, the dense gas gets ionized first. This is the material closest to he sources of ionizing photons. After reionization is completed, the neutral fraction becomes becomes directly proportional to the overdensity of the gas, with under-dense region being more ionized than overdense regions, except the star forming gas.

4.4.4. Lyman-α forest

We construct Lyman-α absorption spectra along different lines of sight in both simulations and construct probability distribution functions and power spectra at redshift $z = 3$. As in Chapter 3, we compare our results to observations by McDonald et al. (2000) and Kim et al. (2007), plotted in Figure 4.29. Both functions agree marginally well with the observations. Since our models do not include stellar winds, we can not expect a very good agreement with the data. However, the results suggest that with the proper treatment of winds, we will be able to reproduce a sensible thermal state of the gas at redshift $z = 3$, as shown in Chapter 3.

4.4.5. Baryon fraction

Finally, we want to study how the gas and stellar content of DM halos changes when photoheating from reionization takes place. In Figure 4.30 we show the baryon fraction of DM halos at redshift $z = 3$. Since there are no winds in our simulations, the baryon fractions is approximately 0.18. It decreases for low mas halos when photoheating is included. We have already observed this effect in Chapter 3. The decrease in the gas and stellar component of halos is larger for GADGET – $\sim 20\%$ than for AREPO – $\sim 1\%$. This difference suggest that GADGET is more efficient in expelling hot gas from low mass halos and thus decreasing the baryon fraction.

4.5. Discussion and Conclusions

In this study, we have proposed a novel implementation of radiative transfer and implemented it in the moving-mesh code AREPO. The method differs substantially from commonly employed ray-tracing or moment-based schemes in that it directly evolves a discretised version of the Boltzmann equation describing the photon distribution function. This is done in terms of an advection treatment, where the photon transport is carried out with a second-order accurate upwind scheme, based on methods that are commonly employed in hydrodynamic mesh codes. We have introduced three different approaches to deal with multiple sources, either by splitting up the radiation field into a linear sum of the partial fields created by all sources, by using a hybrid approach consisting of an exact treatment of the locally brightest sources combined with radiative diffusion, or by employing a direct discretisation of angular space into a finite set of cones. The latter approach is the most general. At a given angular resolution, it can easily deal with an arbitrary number of sources as well as with radiation scattering. Also, if the number of angular cones is enlarged, its angular accuracy becomes progressively better, allowing a simple way to test for convergence with angular resolution.

The radiation transport in our method is manifestly photon conserving. Combined with a photon-conserving treatment of the source terms, this yields a very robust description of the reionization problem, ensuring that ionization fronts propagate at the correct speed.

If needed, our code can employ a reduced speed-of-light approximation that avoids overly small timesteps while not altering the growth of ionized regions in any significant way.

We have presented tests of our new scheme in a variety of cases. Using different photon transport tests in 2D, we have shown that our method manages to accurately capture shadows, and to produce the correct radiation fields independent of the mesh geometry. To test the coupling of gas physics with the photon transport we have carried out isothermal ionized sphere expansion tests and compared to the analytical solutions. The results agree reassuringly well with theoretical expectations, both for our linear summation method and the cone transport approach. Furthermore, we have shown that our method can treat multiple point sources in a highly accurate way, without the problem of a detrimental mutual influence of the sources onto each other, which is encountered in certain moment-based schemes (Gnedin & Abel, 2001; Petkova & Springel, 2009). We have also shown that our code performs well on the problem of the ionization of a static cosmological density field, where we benchmarked our results against those obtained for the same setup in the radiative transfer comparison study of Iliev et al. (2006a). Similarly, our results for I-front trapping in a dense clump, and for a hydrodynamically coupled Strömgren sphere agree well with those of other radiative transfer codes included in Iliev et al. (2006a).

Our final and most demanding test is the hydrogen reionization of the universe, where we have adopted a cone transport approach. The results are compared to a simulation with the cosmological code GADGET using a moment-based approach for treating the RT problem. The underlying cosmological simulation codes produce different star formation rate histories, which results in a different total photon budget. As a consequence reionization in GADGET happens at a higher redshift, i.e. sooner, than in AREPO. The lower number of ionizing photons in the latter code results in a higher volume-averaged neutral fraction at redshift $z = 3$ and a different temperature state of the baryonic gas. We find that in both reionization scenarios the baryon fraction of low mass dark matter halos is reduced due to photoheating processes and observe that the change is bigger in the GADGET simulation than in the one with AREPO, which is due to the higher ionized fractions we find in the former. Finally, we can conclude that despite the differences between the two realizations, both codes perform well at the given problem and are suitable for robustly studying the process of reionization because they produce similar results close to observational constraints, despite the use of very different techniques. We emphasize, however, that the reionization history depends strongly on the star formation rate density in the simulations and which should therefore be accurately reproduced.

Compared to other radiative transfer schemes, our new method based on the cone transport features several interesting advantages. Unlike long-characteristics or Monte Carlo schemes, it avoids any strong sensitivity of the computational cost on the number of sources, and it does not concentrate the computational effort in regions close to the sources, which greatly helps in parallelising the calculations. Also, the ability to easily treat time-dependent effects that are consistently coupled to the hydrodynamic evolution is a substantial asset. Compared to moment-based solvers, our method can cast sharp shadows, and it performs accurately both in the optically thin and the optically thick regimes.

Our cone-transport scheme bears some superficial resembles to the TRAPHIC scheme of Pawlik & Schaye (2008). However, unlike their approach, we do not rely on stochastic Monte Carlo techniques. Instead, we work with an explicit spatial reconstruction of the radiation field and a fixed set of angular cones. As a result, our radiation field is essentially free of stochastic noise, which is a significant advantage compared to Monte Carlo approaches and offers much better convergence rate.

5

Conclusions and Outlook

As we enter the new decade, astrophysical experiments are starting to generate data that will be of critical importance for understanding the process of reionization. LO-FAR (Falcke et al., 2007) is already collecting the first signals and SKA (square kilometer array) (Garrett et al., 2010) will be operational in the foreseeable future. With this first availability of direct observations of reionization it is critical that accurate computer simulations are produced in order to interpret the data correctly. The astrophysical community has developed many numerical solvers for the radiative transfer equation in order to follow the propagation of the photons in space and the subsequent hydrogen photoionizations. As abundant as these codes are, few of them are self-consistent, i.e. treating radiation hydrodynamics and not simply radiation transport alone. Radiation hydrodynamics is shown to have important effects on galaxy formation and therefore it is necessary that self-consistent simulations of reionization treat this problem.

It was the goal of this thesis to develop such a numerical solver for the radiative transfer equation and implement it into an accurate and robust cosmological simulation code. To achieve this task we have developed two methods, in search for an even better solution to the radiative transfer problem.

In Chapter 2 we have introduced the first method and implemented it into the cosmological simulation code GADGET-3. It is based on a moment method with a variable Eddington tensor. We have developed a new discretization scheme for anisotropic diffusion in SPH, which for the first time allows a calculation of such anisotropic diffusion in SPH. We have tested the code and concluded that out results agree very well with analytical predictions and numerical calculation, performed by other codes. However, the long-term evolution of geometric shadows is reproduced inaccurately with this method. We have concluded that, despite this drawback, our code can produce accurate results in the problem of reionization. Furthermore, we have observed that our method has several important strengths - it is independent of the number of sources and it is a radiation hydrodynamics method, computed on-the-fly.

In Chapter 3 we have used our method to simulate cosmological reionization. Our main goal was to determine whether the star formation model together with our RT scheme were able to reproduce a sensible reionization history of the Universe and thermal evolution of

the baryonic gas. For simplicity, we have assumed star forming galaxies as sources for ionizing photons. Since it is unclear to what extent the resolution of our simulations affects the internal processes in the interstellar medium, we have varied the heating efficiency of the streaming photons as well as the luminosity of the star forming galaxies.

We find that all universes that we simulate get reionized between redshifts $z = 8$ and $z = 6$. The span in the reionization time is largely determined by the variance in the luminosity of the sources and to a lesser extent by the heating efficiency. In all cases, the transition from a neutral to an ionized state is rapid. Furthermore, we find that the heating efficiency of the photons has a substantial influence of the thermal state of the gas. In comparing our results to Lyman-α forest observations at redshift $z = 3$, we find that a heating efficiency of $\sim 30\,\mathrm{eV}$ per ionization even is needed in order to reproduce a plausible thermal state of the gas. This heating efficiency corresponds to an average energy of a photon, emitted by a $10^5\,\mathrm{K}$ star, that is absorbed in an optically thick regime.

We study the properties of the baryonic content of DM halos in our "best-fit" simulation. As shown in Figure 5.1, photoheating during reionization affects the gas and stellar mass in low mass DM halos. The effect becomes substantial below masses of $10^9\,\mathrm{M_\odot}$, when the stellar mass is depleted by 50%, relative to the case without photoheating. This corresponds to a decrease in the baryon fraction of more than 40%. This result might shed some more light on the missing satellite problem and explain why we do not see as many luminous DM halo counterparts as we expect from the simulation. On the other hand, other processes such as active galactic nuclei feedback might be more effective in providing an explanation for the phenomenon. In any case, it is clear that the effect of the photoheating during reionization may play an important role in shaping the satellite luminosity function of galaxies (Muñoz et al., 2009; Busha et al., 2010; Iliev et al., 2010).

Despite these encouraging results it is also clear that our simulation results are likely still affected by numerical resolution because the particle number in the lowest mass halos is still too small to yield fully converged results. Ideally, we would like to resolve the full range of star-forming halos with enough particles. While this is unlikely to qualitatively change any of the results presented here, future precision work will require such calculations. Another important caveat that will require further study are uncertainties due to the radiative transfer approximation itself. This is probably best addressed by comparing the results with a completely different approach to radiative transfer.

In Chapter 4 we have presented a scheme in the moving-mesh code AREPO. It avoids the use of the diffusion approximation and can cast sharp shadows, hence a direct one-to-one comparison with the optically-thin variable Eddington tensor approach is particularly interesting. The method is rather different from other schemes as it involves directly solving a version of the Boltzmann equation. The photons are transported via an advection equation, that is solved with an accurate and standard upwind scheme. As the speed of light may cause the time step of such an explicit time integration to become prohibitively small, we adopt a reduced speed of light formalism that has been shown to give accurate results of cosmic reionization. We have furthermore adopted three different methods to deal with multiple sources, all of which make the scheme relatively independent of the number of sources. We found that the best approach is to use a direct discretization of
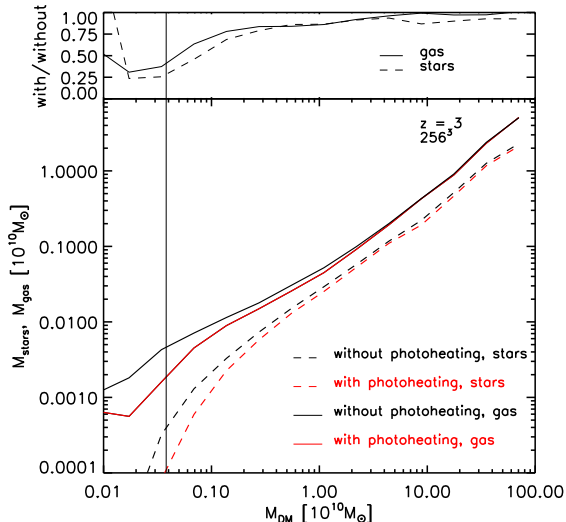
Figure 5.1: Mean stellar and gas masses as a function of the DM halo mass at $z = 3$ in the high resolution simulation. The black vertical corresponds to a mass of 100 DM particles, which can be taken as an (optimistic) resolution limit of the simulation. Photoheating slows down the collapse of gas in halos, which in turn also decreases their stellar and gas masses. The effect becomes stronger for low mass DM halos.

angular space into a finite set of cones.

We have presented numerous tests of our scheme, both in 2D and 3D, with various configurations of shadow-casting objects and source positions. We found that the method is able to cast sharp shadows, whose accuracy depends on the angular resolution of the cones in the discretization approach. Our results agree very well with analytical predictions and other simulation codes. In particular, the scheme provides an accurate treatment of multiple sources, a problematic task in moment-based methods. It also agrees well with other codes in radiation hydrodynamic tests.

Compared to other radiative transfer schemes, our new method based on the cone transport features several interesting advantages. Unlike long-characteristics or Monte Carlo schemes, it avoids any strong sensitivity of the computational cost on the number of sources, and it does not concentrate the computational effort in regions close to the sources, which greatly helps in parallelizing the calculations. Also, the ability to easily treat time-dependent effects that are consistently coupled to the hydrodynamic evolution is a substantial asset. Compared to moment-based solvers, our method can cast sharp shadows, and it performs accurately both in the optically thin and the optically thick regimes.

In our final and most demanding test we demonstrated that our new method is able to produce realistic reionization history of the universe. We have also shown that the differences between our methods (the moment-based and the advection-based) are very

difficult to evaluate in such a complicated simulation, which involves star formation and gas cooling. The interplay between these processes alone may produce deviations in the ionization and thermal state of the gas, which are non-distinguishable from the effect of the RT method. In fact, the GADGET code produces higher star formation rates than the AREPO one, resulting in a larger photon budget, available for reionization in the former, and lead to different reionization histories. However, we note that both schemes are able to reproduce hydrogen reionization and are close to observational constraints, even without the inclusion of stellar winds. Therefore we conclude that both our codes are suitable for further study of reionization and we note that other astrophysical processes, such as star formation and gas cooling, play an important role in that stage of that development of the Universe and a realistic representation can be achieved only if they all reproduce sensible results, comparable to observations. As we still have no sufficient data about the star formation rate at high redshift, we need to explore many models and eventually compare to observational results, as they become available in the future.

A natural further course of this research is to create high resolution hydrogen reionization simulations, using both stars and quasars as sources of ionizing photons. They can be used to extract a mock 21cm signal and be compared to LOFAR data in order to study different reionization models. Including a multi-frequency treatment will also allow us to follow ionization and photoheating processes more accurately, and to study the helium reionization in the Universe.

Helium reionization is an important benchmark in the thermal evolution of the intergalactic gas. The topology and dynamics of helium II reionization are different than those of hydrogen due to the nature of the sources of ionizing photons. Hydrogen is ionized primarily by stellar sources, but double-ionized helium requires higher energy photons and is therefore most likely ionized by quasar radiation. Ionized helium bubbles are therefore distributed on larger scales and trace the quasar density distribution. Large volume numerical simulations are therefore needed to study this process and an efficient and fast RT solver, which our methods present.

Helium reionization is somewhat easier to study observationally than hydrogen reionization, since it happens around redshift $z \sim 3$. It can be inferred from spectra of SDSS quasars (e.g. Bolton et al., 2009; McQuinn et al., 2009). Numerical simulations of helium reionization can therefore provide a better understanding of the process and better means for interpreting the Lyman-α forest.

Radiative transfer has application to many other astrophysical problems as well. It can be used to study star formation in molecular clouds, where ionizing radiation creates pillars of neutral dense gas (e.g. Gritschneder et al., 2009). Radiation hydrodynamics is also relevant in optically thick accretion disks around black holes (e.g. Dotti et al., 2011) and in galaxy formation. In the following years, we plan to explore those frontiers and develop even better methods for simulating radiative processes.

A
Cooling rates

Here we present all cooling rates that we have used in our simulations with temperature evolution. The rates have been obtained from Cen (1992) and are given in $\mathrm{erg\,cm^{-3}\,s^{-1}}$.

1. Recombination cooling rate

$$\Lambda_r = 8.7 \times 10^{-27} \sqrt{T} \left(\frac{T}{10^3} \right)^{-0.2} \bigg/ \left[1 + \left(\frac{T}{10^6} \right)^{0.7} \right] n_e n_{\mathrm{HI}} \; , \tag{A.1}$$

2. Collisional ionisation cooling rate

$$\Lambda_{ci} = 1.27 \times 10^{-21} \sqrt{T} \left(1 + \sqrt{\frac{T}{10^5}} \right) \exp \left(\frac{-157809.1}{T} \right) n_e n_{\mathrm{HI}}, \tag{A.2}$$

3. Collisional excitation cooling rate

$$\Lambda_{ce} = 7.5 \times 10^{-19} \left(1 + \sqrt{\frac{T}{10^5}} \right)^{-1} \exp \left(\frac{-118348}{T} \right) n_e n_{\mathrm{HI}}, \tag{A.3}$$

4. Bremsstrahlung cooling rate

$$\Lambda_{\mathrm{B}} = 1.42 \times 10^{-27} g_{\mathrm{ff}} \sqrt{T} n_e n_{\mathrm{HI}}, \tag{A.4}$$

where $g_{\mathrm{ff}} = 1.3$ is the Gaunt factor.

Conjugate gradient method

B.1. Method of Steepest Descent

In this Appendix, we give a derivation of the CG technique for solving linear problems, which we employ in our implicit time integration scheme of the anisotropic diffusion problem. As the CG scheme is closely related to the method of steepest decent, we start with an explanation of this more general technique, and then specialize to the CG method.

The method of steepest descent is a scheme to solve a linear system of equations given by $A\mathbf{x} = \mathbf{b}$. The idea is to obtain the solution as the minimum of the quadratic form

$$f(\mathbf{x}) = \frac{1}{2}\mathbf{x}^T A \mathbf{x} - \mathbf{b}^T \mathbf{x}, \tag{B.1}$$

such that

$$f'(\mathbf{x}) = \frac{1}{2}A^T \mathbf{x} + \frac{1}{2}A\mathbf{x} - \mathbf{b}. \tag{B.2}$$

This equation reduces to

$$f'(\mathbf{x}) = A\mathbf{x} - \mathbf{b} \tag{B.3}$$

if $\mathbf{A}$ is symmetric and positive definite, i.e. if $\mathbf{x}^T A \mathbf{x} > 0$ for all $\mathbf{x} \neq 0$.

We now consider an iteration scheme that tries to find the solution $\mathbf{x}$. As we take steps, we choose the direction of the next step in the direction in which the quadratic form f decreases most rapidly, which is in the direction opposite to the gradient $f'(\mathbf{x})$. Therefore, the next step should be proportional to $-f'(\mathbf{x}_{(i)}) = \mathbf{b} - A\mathbf{x}_{(i)}$. Here the index i denotes the number of the step we take towards the correct value of $\mathbf{x}$. Let us denote the difference between the numerical and the exact solution as $\mathbf{e}_{(i)} = \mathbf{x}_{(i)} - \mathbf{x}$, and the residual as $\mathbf{r}_{(i)} = \mathbf{b} - A\mathbf{x}_{(i)} = -f'(\mathbf{x}_{(i)})$. Therefore, the next step taken is given by $\mathbf{x}_{(1)} = \mathbf{x}_{(0)} + \alpha \mathbf{r}_{(0)}$. The optimum value of α is chosen such that the directional derivative $\frac{d}{d\alpha}f(\mathbf{x}_{(1)})$ equals 0, i.e. the vectors $f'(\mathbf{x}_{(1)})$ and $\mathbf{r}_{(0)}$ should be chosen orthogonal:

$$\frac{\mathrm{d}}{\mathrm{d}\alpha}f(\mathbf{x}_{(1)}) = f'(\mathbf{x}_{(1)})^T \frac{\mathrm{d}}{\mathrm{d}\alpha}\mathbf{x}_{(1)} = f'(\mathbf{x}_{(1)})^T \mathbf{r}_{(0)} = 0 \tag{B.4}$$

We further notice that $f'(\mathbf{x}_{(1)}) = -\mathbf{r}_{(1)}$ and therefore

$$
\begin{aligned}
\mathbf{r}_{(1)}^T \mathbf{r}_{(0)} &= 0 \\
(\mathbf{b} - \mathbf{A}\mathbf{x}_{(1)})^T \mathbf{r}_{(0)} &= 0 \\
(\mathbf{b} - \mathbf{A}(\mathbf{x}_{(0)} + \alpha \mathbf{r}_{(0)}))^T \mathbf{r}_{(0)} &= 0 \\
(\mathbf{b} - \mathbf{A}\mathbf{x}_{(0)})^T \mathbf{r}_{(0)} - \alpha(\mathbf{A}\mathbf{r}_{(0)})^T \mathbf{r}_{(0)} &= 0 \\
(\mathbf{b} - \mathbf{A}\mathbf{x}_{(0)})^T \mathbf{r}_{(0)} &= \alpha(\mathbf{A}\mathbf{r}_{(0)})^T \mathbf{r}_{(0)} \\
\mathbf{r}_{(0)}^T \mathbf{r}_{(0)} &= \alpha \mathbf{r}_{(0)}^T (\mathbf{A}\mathbf{r}_{(0)}) \\
\alpha &= \frac{\mathbf{r}_{(0)}^T \mathbf{r}_{(0)}}{\mathbf{r}_{(0)}^T \mathbf{A}\mathbf{r}_{(0)}}
\end{aligned}
$$

Finally, putting it all together, the method of steepest descent is as follows

$$\mathbf{r}_{(i)} = \mathbf{b} - \mathbf{A}\mathbf{x}_{(i)} \tag{B.5}$$

$$\alpha_{(i)} = \frac{\mathbf{r}_{(i)}^T \mathbf{r}_{(i)}}{\mathbf{r}_{(i)}^T \mathbf{A}\mathbf{r}_{(i)}} \tag{B.6}$$

$$\mathbf{x}_{(i+1)} = \mathbf{x}_{(i)} + \alpha_{(i)} \mathbf{r}_{(i)} \tag{B.7}$$

$$\mathbf{r}_{(i+1)} = \mathbf{r}_{(i)} - \alpha_{(i)} \mathbf{A}\mathbf{r}_{(i)} \tag{B.8}$$

B.2. Conjugate Gradient Method

In the method of steepest descent the value of $\mathbf{x}$ is determined via successively adding the search directions $\mathbf{r}_{(i)}$. Let us define the set of directions $\{\mathbf{d}_{(i)}\}$ as the search directions for the CG method, such that $\mathbf{x}_{(i+1)} = \mathbf{x}_{(i)} + \alpha_{(i)}\mathbf{d}_{(i)}$ and $\mathbf{r}_{(i+1)} = \mathbf{r}_{(i)} - \alpha_{(i)}A\mathbf{d}_{(i)}$. We further require that the vectors $\{\mathbf{d}_{(i)}\}$ are $\mathbf{A}$-conjugate, i.e. $\mathbf{d}_{(i)}\mathbf{A}\mathbf{d}_{(j)} = 0$, which means

$$\mathbf{d}_{(i+1)} = \mathbf{r}_{(i+1)} + \sum_{k=0}^{i} \beta_{ik} \mathbf{d}_{(k)}. \tag{B.9}$$

Using Gram-Schmidt orthogonalization, the coefficients β_{ik} are found to be

$$
\beta_{ik} = \begin{cases} \dfrac{1}{\alpha_{(i-1)}} \dfrac{\mathbf{r}_{(i)}^T \mathbf{r}_{(i)}}{\mathbf{d}_{(i-1)}^T \mathbf{A}\mathbf{d}_{(i-1)}} & \text{for } i = k+1 \\[2em] 0 & \text{for } i > k+1 \end{cases} \tag{B.10}
$$

Thus

$$\beta_{(i)} \equiv \beta_{i,i-i} = \frac{\mathbf{r}_{(i)}^T \mathbf{r}_{(i)}}{\mathbf{r}_{(i-1)}^T \mathbf{r}_{(i-1)}}. \tag{B.11}$$

Therefore, the CG method can be summarized as follows:

$$\mathbf{r}_{(0)} = \mathbf{b} - \mathbf{A}\mathbf{x}_{(0)} \tag{B.12}$$

$$\mathbf{d}_{(0)} = \mathbf{b} - \mathbf{A}\mathbf{x}_{(0)} \tag{B.13}$$

$$\alpha_{(i)} = \frac{\mathbf{r}_{(i)}^T \mathbf{r}_{(i)}}{\mathbf{d}_{(i)}^T \mathbf{A}\mathbf{d}_{(i)}} \tag{B.14}$$

$$\mathbf{x}_{(i+1)} = \mathbf{x}_{(i)} + \alpha_{(i)}\mathbf{d}_{(i)} \tag{B.15}$$

$$\mathbf{r}_{(i+1)} = \mathbf{r}_{(i)} - \alpha_{(i)}\mathbf{A}\mathbf{d}_{(i)} \tag{B.16}$$

$$\beta_{(i+1)} = \frac{\mathbf{r}_{(i+1)}^T \mathbf{r}_{(i+1)}}{\mathbf{r}_{(i)}^T \mathbf{r}_{(i)}} \tag{B.17}$$

$$\mathbf{d}_{(i+1)} = \mathbf{r}_{(i+1)} - \beta_{(i+1)}\mathbf{A}\mathbf{d}_{(i)} \tag{B.18}$$

The interesting feature of the CG method is that each subsequent correction to the solution vector is orthogonal to all previous ones, while at the same time it points into the direction where the error in the solution decreases most quickly. This normally produces a comparatively rapid convergence of the scheme.

Acknowledgements

Publications

1. **Petkova, M.**, & Springel, V., *An implementation of radiative transfer in the cosmological simulation code Gadget,* 2009, MNRAS, 396, 1383

2. **Petkova, M.**, & Springel, V., *Simulations of galaxy formation with radiative transfer: Hydrogen reionization and radiative feedback*, 2010, MNRAS, p. 1851

3. **Petkova, M.**, & Springel, V., *A novel approach for accurate radiative transfer in cosmological hydrodynamic simulations*, 2010, astro-ph: 1012.1017, submitted to MNRAS on the 7th of December

4. Dotti, M., Maio, U., **Petkova, M.**, Springel, V., *Massive black hole feeding in circumnuclear discs: coherent or chaotic?*, 2011, in preparation

Bibliography

Abel T., Bryan G. L., Norman M. L., The Formation of the First Star in the Universe, 2002, Science, 295, 93

Abel T., Norman M. L., Madau P., Photon-conserving Radiative Transfer around Point Sources in Multidimensional Numerical Cosmology, 1999, ApJ, 523, 66

Abel T., Wandelt B. D., Adaptive ray tracing for radiative transfer around point sources, 2002, MNRAS, 330, L53

Adshead P. J., Furlanetto S. R., Reionization and the large-scale 21-cm cosmic microwave background cross-correlation, 2008, MNRAS, 384, 291

Ahn K., Shapiro P. R., Does radiative feedback by the first stars promote or prevent second generation star formation?, 2007, MNRAS, 375, 881

Altay G., Croft R. A. C., Pelupessy I., SPHRAY: a smoothed particle hydrodynamics ray tracer for radiative transfer, 2008, MNRAS, 386, 1931

Alvarez M. A., Bromm V., Shapiro P. R., The H II Region of the First Star, 2006, ApJ, 639, 621

Alvarez M. A., Busha M., Abel T., Wechsler R. H., Connecting Reionization to the Local Universe, 2009, ApJL, 703, L167

Alvarez M. A., Komatsu E., Doré O., Shapiro P. R., The Cosmic Reionization History as Revealed by the Cosmic Microwave Background Doppler-21 cm Correlation, 2006, ApJ, 647, 840

Alvarez M. A., Shapiro P. R., Ahn K., Iliev I. T., Implications of WMAP 3 Year Data for the Sources of Reionization, 2006, ApJL, 644, L101

Aubert D., Teyssier R., A radiative transfer scheme for cosmological reionization based on a local Eddington tensor, 2008, MNRAS, 387, 295

Baek S., Di Matteo P., Semelin B., Combes F., Revaz Y., The simulated 21 cm signal during the epoch of reionization: full modeling of the Ly-α pumping, 2009, A&A, 495, 389

Becker R. H., et al., Evidence for Reionization at z~6: Detection of a Gunn-Peterson Trough in a z=6.28 Quasar, 2001, AJ, 122, 2850

Blanc G. A., et al., The HETDEX Pilot Survey for Emission Line Galaxies - II: The Evolution of the Ly-alpha Escape Fraction from the UV Slope and Luminosity Function of 1.9 ¡ z ¡ 3.8 LAEs, 2010, ArXiv e-prints

Bolton J. S., Becker G. D., Resolving the high redshift Lyα forest in smoothed particle hydrodynamics simulations, 2009, MNRAS, 398, L26

Bolton J. S., Haehnelt M. G., Viel M., Springel V., The Lyman α forest opacity and the metagalactic hydrogen ionization rate at z~ 2-4, 2005, MNRAS, 357, 1178

Bolton J. S., Oh S. P., Furlanetto S. R., Photoheating and the fate of hard photons during the reionization of HeII by quasars, 2009, MNRAS, 395, 736

Bolton J. S., Viel M., Kim T., Haehnelt M. G., Carswell R. F., Possible evidence for an inverted temperature-density relation in the intergalactic medium from the flux distribution of the Lyα forest, 2008a, MNRAS, 386, 1131

Bolton J. S., Viel M., Kim T.-S., Haehnelt M. G., Carswell R. F., Possible evidence for an inverted temperature-density relation in the intergalactic medium from the flux distribution of the Lyα forest, 2008b, MNRAS, 386, 1131

Bowman J., Rogers A., A lower limit of dz¿0.06 for the duration of the reionization epoch, 2010, Nature, 468, 796

Busha M. T., et al., The Impact of Inhomogeneous Reionization on the Satellite Galaxy Population of the Milky Way, 2010, ApJ, 710, 408

Cantalupo S., Porciani C., RADAMESH: Cosmological Radiative Transfer for Adaptive Mesh Refinement Simulations, 2010, ArXiv e-prints

Cen R., A hydrodynamic approach to cosmology - Methodology, 1992, ApJS, 78, 341

Cen R., A Fast, Accurate, and Robust Algorithm for Transferring Radiation in Three-dimensional Space, 2002, ApJS, 141, 211

Choudhury T. R., Ferrara A., Searching for the reionization sources, 2007, MNRAS, 380, L6

Ciardi B., Bianchi S., Ferrara A., Lyman continuum escape from an inhomogeneous interstellar medium, 2002, MNRAS, 331, 463

Ciardi B., Ferrara A., Governato F., Jenkins A., Inhomogeneous reionization of the intergalactic medium regulated by radiative and stellar feedbacks, 2000, MNRAS, 314, 611

Ciardi B., Ferrara A., Marri S., Raimondo G., Cosmological reionization around the first stars: Monte Carlo radiative transfer, 2001, MNRAS, 324, 381

Ciardi B., Madau P., Probing beyond the Epoch of Hydrogen Reionization with 21 Centimeter Radiation, 2003, ApJ, 596, 1

Ciardi B., Stoehr F., White S. D. M., Simulating intergalactic medium reionization, 2003, MNRAS, 343, 1101

Croft R. A. C., Altay G., Radiation-induced large-scale structure during the reionization epoch: the autocorrelation function, 2008, MNRAS, 388, 1501

Davé R., Hernquist L., Katz N., Weinberg D. H., The Low-Redshift LYalpha Forest in Cold Dark Matter Cosmologies, 1999, ApJ, 511, 521

Doré O., Holder G., Alvarez M., Iliev I. T., Mellema G., Pen U.-L., Shapiro P. R., Signature of patchy reionization in the polarization anisotropy of the CMB, 2007, PRd, 76, 043002

Dotti M., Maio U., Petkova M., Springel V., Massive black hole feeding in circumnuclear discs: coherent or chaotic?, 2011, in preparation

Falcke H. D., et al., A very brief description of LOFAR the Low Frequency Array, 2007, Highlights of Astronomy, 14, 386

Fan X., 2007, in Metcalfe N., Shanks T., eds, Cosmic Frontiers Vol. 379 of Astronomical Society of the Pacific Conference Series, The Highest Redshift Quasars: Early Black Hole Growth and the End of Reionization Epoch. p. 35

Fan X., Carilli C. L., Keating B., Observational Constraints on Cosmic Reionization, 2006, ARA&A, 44, 415

Fan X., et al., Evolution of the Ionizing Background and the Epoch of Reionization from the Spectra of z~6 Quasars, 2002, AJ, 123, 1247

Fan X., et al., A Survey of z ¿ 5.7 Quasars in the Sloan Digital Sky Survey. II. Discovery of Three Additional Quasars at z ¿ 6, 2003, AJ, 125, 1649

Fan X., et al., A Survey of z>5.7 Quasars in the Sloan Digital Sky Survey. IV. Discovery of Seven Additional Quasars, 2006a, AJ, 131, 1203

Fan X., et al., Constraining the Evolution of the Ionizing Background and the Epoch of Reionization with z~6 Quasars. II. A Sample of 19 Quasars, 2006b, AJ, 132, 117

Fan X. o., A Survey of z ¿ 5.7 Quasars in the Sloan Digital Sky Survey. III. Discovery of Five Additional Quasars, 2004, AJ, 128, 515

Field G. B., The Spin Temperature of Intergalactic Neutral Hydrogen., 1959, ApJ, 129, 536

Finlator K., Özel F., Davé R., A new moment method for continuum radiative transfer in cosmological re-ionization, 2009, MNRAS, 393, 1090

Furlanetto S. R., Briggs F. H., 21 cm tomography of the high-redshift universe with the Square Kilometer Array, 2004, New Astronomy Reviews, 48, 1039

Furlanetto S. R., McQuinn M., Hernquist L., Characteristic scales during reionization, 2006, MNRAS, 365, 115

Furlanetto S. R., Mesinger A., The ionizing background at the end of reionization, 2009, MNRAS, 394, 1667

Furlanetto S. R., Oh S. P., Taxing the rich: recombinations and bubble growth during reionization, 2005, MNRAS, 363, 1031

Furlanetto S. R., Oh S. P., Redshifted 21 cm Emission from Minihalos before Reionization, 2006, ApJ, 652, 849

Furlanetto S. R., Oh S. P., The Temperature-Density Relation of the Intergalactic Medium after Hydrogen Reionization, 2009, ApJ, 701, 94

Gallerani S., Salvaterra R., Ferrara A., Choudhury T. R., Testing reionization with gamma-ray burst absorption spectra, 2008, MNRAS, 388, L84

Garrett M. A., Cordes J. M., Deboer D. R., Jonas J. L., Rawlings S., Schilizzi R. T., 2010, in ISKAF2010 Science Meeting The Square Kilometre Array (SKA) - Phase 1 Design Concept

Geil P. M., Wyithe J. S. B., The impact of a percolating IGM on redshifted 21-cm observations of quasar HII regions, 2008, MNRAS, 386, 1683

Gnedin N. Y., Cosmological Reionization by Stellar Sources, 2000, ApJ, 535, 530

Gnedin N. Y., Abel T., Multi-dimensional cosmological radiative transfer with a Variable Eddington Tensor formalism, 2001, New Astronomy, 6, 437

Gnedin N. Y., Fan X., Cosmic Reionization Redux, 2006, ApJ, 648, 1

Gnedin N. Y., Kravtsov A. V., Chen H., Escape of Ionizing Radiation from High-Redshift Galaxies, 2008, ApJ, 672, 765

Gnedin N. Y., Ostriker J. P., Reionization of the Universe and the Early Production of Metals, 1997, ApJ, 486, 581

Gnedin N. Y., Shaver P. A., Redshifted 21 Centimeter Emission from the Pre-Reionization Era. I. Mean Signal and Linear Fluctuations, 2004, ApJ, 608, 611

González V., et al., The Stellar Mass Density and Specific Star Formation Rate of the Universe at z ˜ 7, 2010, ApJ, 713, 115

Górski K. M., Hivon E., Banday A. J., Wandelt B. D., Hansen F. K., Reinecke M., Bartelmann M., HEALPix: A Framework for High-Resolution Discretization and Fast Analysis of Data Distributed on the Sphere, 2005, ApJ, 622, 759

Gritschneder M., Naab T., Burkert A., Walch S., Heitsch F., Wetzstein M., iVINE - Ionization in the parallel TREE/SPH code VINE: first results on the observed age-spread around O-stars, 2009, MNRAS, 393, 21

Gritschneder M., Naab T., Walch S., Burkert A., Heitsch F., Driving Turbulence and Triggering Star Formation by Ionizing Radiation, 2009, ApJL, 694, L26

Gunn J. E., Peterson B. A., On the Density of Neutral Hydrogen in Intergalactic Space., 1965, ApJ, 142, 1633

Haardt F., Madau P., Radiative Transfer in a Clumpy Universe. II. The Ultraviolet Extragalactic Background, 1996, ApJ, 461, 20

Haehnelt M. G., Madau P., Kudritzki R., Haardt F., An Ionizing Ultraviolet Background Dominated by Massive Stars, 2001, ApJL, 549, L151

Hasegawa K., Umemura M., START: smoothed particle hydrodynamics with tree-based accelerated radiative transfer, 2010, MNRAS, 407, 2632

Hayes M., Schaerer D., Ostlin G., Mas-Hesse J. M., Atek H., Kunth D., On the redshift-evolution of the Lyman-alpha escape fraction and the dust content of galaxies, 2010, ArXiv e-prints

Hoeft M., Yepes G., Gottlöber S., Springel V., Dwarf galaxies in voids: suppressing star formation with photoheating, 2006, MNRAS, 371, 401

Iliev I. T., et al., Cosmological radiative transfer codes comparison project - I. The static density field tests, 2006a, MNRAS, 371, 1057

Iliev I. T., et al., Cosmological radiative transfer codes comparison project - I. The static density field tests, 2006b, MNRAS, 371, 1057

Iliev I. T., et al., Cosmological radiative transfer comparison project - II. The radiation-hydrodynamic tests, 2009, MNRAS, 400, 1283

Iliev I. T., Mellema G., Pen U.-L., Merz H., Shapiro P. R., Alvarez M. A., Simulating cosmic reionization at large scales - I. The geometry of reionization, 2006, MNRAS, 369, 1625

Iliev I. T., Moore B., Gottloeber S., Yepes G., Hoffman Y., Mellema G., Reionization of the Local Group of Galaxies, 2010, ArXiv e-prints: 1005.3139

Iliev I. T., Shapiro P. R., Ferrara A., Martel H., On the Direct Detectability of the Cosmic Dark Ages: 21 Centimeter Emission from Minihalos, 2002, ApJL, 572, L123

Iliev I. T., Shapiro P. R., Mellema G., Pen U.-L., McDonald P., Bond J. R., Simulating Reionization: Character and Observability, 2007, ArXiv e-prints, 708

Iliev I. T., Shapiro P. R., Raga A. C., Minihalo photoevaporation during cosmic reionization: evaporation times and photon consumption rates, 2005, MNRAS, 361, 405

Jelić V., et al., Foreground simulations for the LOFAR-epoch of reionization experiment, 2008, MNRAS, 389, 1319

Jubelgas M., Springel V., Dolag K., Thermal conduction in cosmological SPH simulations, 2004, MNRAS, 351, 423

Katz N., Weinberg D. H., Hernquist L., Cosmological Simulations with TreeSPH, 1996, ApJS, 105, 19

Kennicutt Jr. R. C., The Global Schmidt Law in Star-forming Galaxies, 1998, ApJ, 498, 541

Kim T., Bolton J. S., Viel M., Haehnelt M. G., Carswell R. F., An improved measurement of the flux distribution of the Lyα forest in QSO absorption spectra: the effect of continuum fitting, metal contamination and noise properties, 2007, MNRAS, 382, 1657

Kohler K., Gnedin N. Y., Hamilton A. J. S., Large-Scale Simulations of Reionization, 2007, ApJ, 657, 15

Komatsu E., et al., Seven-Year Wilkinson Microwave Anisotropy Probe (WMAP) Observations: Cosmological Interpretation, 2010, ArXiv e-prints

Kunasz P., Auer L. H., Short characteristic integration of radiative transfer problems: formal solution in two-dimensional slabs., 1988, Journal of Quantitative Spectroscopy and Radiative Transfer, 39, 67

Larson D., et al., Seven-Year Wilkinson Microwave Anisotropy Probe (WMAP) Observations: Power Spectra and WMAP-Derived Parameters, 2010, ArXiv e-prints

Lee K., Cen R., Gott III J. R., Trac H., The Topology of Cosmological Reionization, 2008, ApJ, 675, 8

Lidz A., McQuinn M., Zaldarriaga M., Hernquist L., Dutta S., Quasar Proximity Zones and Patchy Reionization, 2007, ApJ, 670, 39

Loeb A., The Frontier of Reionization: Theory and Forthcoming Observations, 2007, ArXiv e-prints, 711

Madau P., Haardt F., Rees M. J., Radiative Transfer in a Clumpy Universe. III. The Nature of Cosmological Ionizing Sources, 1999, ApJ, 514, 648

Maselli A., Ferrara A., Ciardi B., CRASH: a radiative transfer scheme, 2003, MNRAS, 345, 379

McDonald P., et al., The Observed Probability Distribution Function, Power Spectrum, and Correlation Function of the Transmitted Flux in the Lyα Forest, 2000, ApJ, 543, 1

McQuinn M., et al., Probing the neutral fraction of the IGM with GRBs during the epoch of reionization, 2008, MNRAS, 388, 1101

McQuinn M., Lidz A., Zaldarriaga M., Hernquist L., Hopkins P. F., Dutta S., Faucher-Giguère C., He II Reionization and its Effect on the Intergalactic Medium, 2009, ApJ, 694, 842

Mellema G., Iliev I. T., Alvarez M. A., Shapiro P. R., C^2-ray: A new method for photon-conserving transport of ionizing radiation, 2006, New Astronomy, 11, 374

Mellema G., Iliev I. T., Pen U., Shapiro P. R., Simulating cosmic reionization at large scales - II. The 21-cm emission features and statistical signals, 2006, MNRAS, 372, 679

Mellema G., Raga A. C., Canto J., Lundqvist P., Balick B., Steffen W., Noriega-Crespo A., Photo-evaporation of clumps in planetary nebulae, 1998, A&A, 331, 335

Mesinger A., Was reionization complete by z ~ 5-6?, 2010, MNRAS, 407, 1328

Mihalas D., Weibel Mihalas B., 1984, Foundations of radiation hydrodynamics. New York: Oxford University Press, 1984

Miralda-Escudé J., Haehnelt M., Rees M. J., Reionization of the Inhomogeneous Universe, 2000, ApJ, 530, 1

Monaghan J. J., Smoothed particle hydrodynamics, 1992, ARA&A, 30, 543

Morales M. F., Wyithe J. S. B., Reionization and Cosmology with 21-cm Fluctuations, 2010, ARA&A, 48, 127

Muñoz J. A., Madau P., Loeb A., Diemand J., Probing the epoch of reionization with Milky Way satellites, 2009, MNRAS, 400, 1593

Nakamoto T., Umemura M., Susa H., The effects of radiative transfer on the reionization of an inhomogeneous universe, 2001, MNRAS, 321, 593

Nayakshin S., Cha S., Hobbs A., Dynamic Monte Carlo radiation transfer in SPH: radiation pressure force implementation, 2009, MNRAS, 397, 1314

Norman M. L., Paschos P., Abel T., Simulating inhomogeneous reionization, 1998, Memorie della Societa Astronomica Italiana, 69, 455

Okamoto T., Gao L., Theuns T., Mass loss of galaxies due to an ultraviolet background, 2008, MNRAS, 390, 920

Osterbrock D. E., Ferland G. J., 2006, Astrophysics of gaseous nebulae and active galactic nuclei. Astrophysics of gaseous nebulae and active galactic nuclei, 2nd. ed. by D.E. Osterbrock and G.J. Ferland. Sausalito, CA: University Science Books, 2006

Paardekooper J., Kruip C. J. H., Icke V., SimpleX2: radiative transfer on an unstructured, dynamic grid, 2010, A&A, 515, A79

Patel M., Warren S. J., Mortlock D. J., Fynbo J. P. U., The reanalysis of spectra of GRB 080913 to estimate the neutral fraction of the IGM at a redshift of 6.7, 2010, A&A, 512, L3

Pawlik A. H., Schaye J., TRAPHIC - radiative transfer for smoothed particle hydrodynamics simulations, 2008, MNRAS, 389, 651

Pawlik A. H., Schaye J., Photoheating and supernova feedback amplify each other's effect on the cosmic star formation rate, 2009, MNRAS, 396, L46

Petkova M., Springel V., An implementation of radiative transfer in the cosmological simulation code GADGET, 2009, MNRAS, 396, 1383

Petkova M., Springel V., Simulations of galaxy formation with radiative transfer: hydrogen reionization and radiative feedback, 2010, MNRAS, p. 1851

Pritchard J., Loeb A., Hydrogen was not ionized abruptly, 2010, Nature, 468, 772

Pritchard J. R., Loeb A., Wyithe J. S. B., Constraining reionization using 21-cm observations in combination with CMB and Lyα forest data, 2010, MNRAS, 408, 57

Razoumov A. O., Cardall C. Y., Fully threaded transport engine: new method for multiscale radiative transfer, 2005, MNRAS, 362, 1413

Razoumov A. O., Sommer-Larsen J., Ionizing Radiation from z = 4-10 Galaxies, 2010, ApJ, 710, 1239

Reynolds D. R., Hayes J. C., Paschos P., Norman M. L., Self-consistent solution of cosmological radiation-hydrodynamics and chemical ionization, 2009, Journal of Computational Physics, 228, 6833

Richards G. T., et al., The Sloan Digital Sky Survey Quasar Survey: Quasar Luminosity Function from Data Release 3, 2006, AJ, 131, 2766

Ricotti M., Shull J. M., Feedback from Galaxy Formation: Escaping Ionizing Radiation from Galaxies at High Redshift, 2000, ApJ, 542, 548

Rijkhorst E.-J., Plewa T., Dubey A., Mellema G., Hybrid characteristics: 3D radiative transfer for parallel adaptive mesh refinement hydrodynamics, 2006, A&A, 452, 907

Ritzerveld J., Icke V., Transport on adaptive random lattices, 2006, Phys Rev E, 74, 026704

Rudnick L., et al., 2009, in astro2010: The Astronomy and Astrophysics Decadal Survey Vol. 2010 of Astronomy, Clusters and Large-Scale Structure: the Synchrotron Keys. p. 253

Salvaterra R., et al., GRB090423 at a redshift of z~8.1, 2009, Nature, 461, 1258

Santos M. G., Amblard A., Pritchard J., Trac H., Cen R., Cooray A., Cosmic Reionization and the 21 cm Signal: Comparison between an Analytical Model and a Simulation, 2008, ApJ, 689, 1

Santos M. G., Cooray A., Haiman Z., Knox L., Ma C., Small-Scale Cosmic Microwave Background Temperature and Polarization Anisotropies Due to Patchy Reionization, 2003, ApJ, 598, 756

Shapiro P. R., Iliev I. T., Raga A. C., Photoevaporation of cosmological minihaloes during reionization, 2004, MNRAS, 348, 753

Shin M.-S., Trac H., Cen R., Cosmological H II Bubble Growth during Reionization, 2008, ApJ, 681, 756

Sokasian A., Abel T., Hernquist L., Springel V., Cosmic reionization by stellar sources: Population II stars, 2003, MNRAS, 344, 607

Sokasian A., Abel T., Hernquist L. E., Simulating reionization in numerical cosmology, 2001, New Astronomy, 6, 359

Sokasian A., Yoshida N., Abel T., Hernquist L., Springel V., Cosmic reionization by stellar sources: population III stars, 2004, MNRAS, 350, 47

Songaila A., The Evolution of the Intergalactic Medium Transmission to Redshift 6, 2004, AJ, 127, 2598

Spitzer L., 1978, Physical processes in the interstellar medium. New York Wiley-Interscience

Spitzer L., 1998, Physical Processes in the Interstellar Medium. Physical Processes in the Interstellar Medium, by Lyman Spitzer, pp. 335. ISBN 0-471-29335-0. Wiley-VCH , May 1998.

Springel V., The cosmological simulation code GADGET-2, 2005, MNRAS, 364, 1105

Springel V., E pur si muove: Galilean-invariant cosmological hydrodynamical simulations on a moving mesh, 2010, MNRAS, 401, 791

Springel V., Hernquist L., Cosmological smoothed particle hydrodynamics simulations: the entropy equation, 2002, MNRAS, 333, 649

Springel V., Hernquist L., Cosmological smoothed particle hydrodynamics simulations: a hybrid multiphase model for star formation, 2003a, MNRAS, 339, 289

Springel V., Hernquist L., The history of star formation in a Λ cold dark matter universe, 2003b, MNRAS, 339, 312

Springel V., Yoshida N., White S. D. M., GADGET: a code for collisionless and gasdynamical cosmological simulations, 2001, New Astronomy, 6, 79

Susa H., Smoothed Particle Hydrodynamics Coupled with Radiation Transfer, 2006, PASJ, 58, 445

Tauber J. A., Mandolesi N., Puget J., Banos T., Bersanelli M., Bouchet F. R., Butler R. C., Charra J., Crone G., Dodsworth J., et al. Planck pre-launch status: The Planck mission, 2010, A&A, 520, A1

Thomas R. M., Zaroubi S., Ciardi B., Pawlik A. H., Labropoulos P., Jelić V., Bernardi G., Brentjens M. A., de Bruyn A. G., Harker G. J. A., Koopmans L. V. E., Mellema G., Pandey V. N., Schaye J., Yatawatta S., Fast large-scale reionization simulations, 2009, MNRAS, 393, 32

Tornatore L., Borgani S., Springel V., Matteucci F., Menci N., Murante G., Cooling and heating the intracluster medium in hydrodynamical simulations, 2003, MNRAS, 342, 1025

Totani T., et al., 2006, in IAU Joint Discussion Vol. 7 of IAU Joint Discussion, Implications for the Cosmic Reionization from the Optical Afterglow Spectrum of the Gamma-Ray Burst 050904 at z = 6.3

Trac H., Cen R., Radiative Transfer Simulations of Cosmic Reionization. I. Methodology and Initial Results, 2007, ApJ, 671, 1

Trac H., Cen R., Loeb A., Imprint of Inhomogeneous Hydrogen Reionization on the Temperature Distribution of the Intergalactic Medium, 2008, ApJL, 689, L81

Wadepuhl M., Springel V., Satellite galaxies in hydrodynamical simulations of Milky Way sized galaxies, 2010, ArXiv e-prints: 1004.3217

Whalen D., Norman M. L., A Multistep Algorithm for the Radiation Hydrodynamical Transport of Cosmological Ionization Fronts and Ionized Flows, 2006, ApJS, 162, 281

White R. L., Becker R. H., Fan X., Strauss M. A., Probing the Ionization State of the Universe at z>6, 2003, AJ, 126, 1

Whitehouse S. C., Bate M. R., Smoothed particle hydrodynamics with radiative transfer in the flux-limited diffusion approximation, 2004, MNRAS, 353, 1078

Whitehouse S. C., Bate M. R., Monaghan J. J., A faster algorithm for smoothed particle hydrodynamics with radiative transfer in the flux-limited diffusion approximation, 2005, MNRAS, 364, 1367

Willott C. J., et al., Four Quasars above Redshift 6 Discovered by the Canada-France High-z Quasar Survey, 2007, AJ, 134, 2435

Wise J. H., Abel T., How Very Massive Metal-Free Stars Start Cosmological Reionization, 2008, ApJ, 684, 1

Wise J. H., Cen R., Ionizing Photon Escape Fractions From High-Redshift Dwarf Galaxies, 2009, ApJ, 693, 984

York D. G., et al., The Sloan Digital Sky Survey: Technical Summary, 2000, AJ, 120, 1579

Yoshida N., Oh S. P., Kitayama T., Hernquist L., Early Cosmological H II/He III Regions and Their Impact on Second-Generation Star Formation, 2007, ApJ, 663, 687

Zahn O., Lidz A., McQuinn M., Dutta S., Hernquist L., Zaldarriaga M., Furlanetto S. R., Simulations and Analytic Calculations of Bubble Growth during Hydrogen Reionization, 2007, ApJ, 654, 12

Zaldarriaga M., Polarization of the microwave background in reionized models, 1997, Phys. Rev. D, 55, 1822

Zaldarriaga M., Furlanetto S. R., Hernquist L., 21 Centimeter Fluctuations from Cosmic Gas at High Redshifts, 2004, ApJ, 608, 622